



Virginia Commonwealth University
VCU Scholars Compass

Theses and Dissertations


Graduate School

2016

Sol-Gel Assembly of Metal Nanostructures into Metallic Gel Frameworks and Their Applications

Xiaonan Gao
Xiaonan Gao

Follow this and additional works at: <https://scholarscompass.vcu.edu/etd>

 Part of the [Inorganic Chemistry Commons](#), and the [Materials Chemistry Commons](#)

© The Author

Downloaded from

<https://scholarscompass.vcu.edu/etd/4319>

This Dissertation is brought to you for free and open access by the Graduate School at VCU Scholars Compass. It has been accepted for inclusion in Theses and Dissertations by an authorized administrator of VCU Scholars Compass. For more information, please contact libcompass@vcu.edu.

Xiaonan Gao 2016

All Rights Reserved

Sol-Gel Assembly of Metal Nanostructures into Metallic Gel Frameworks and Their Applications

A dissertation submitted in partial fulfillment of the requirements for the
degree of Doctor of Philosophy at Virginia Commonwealth University

by

Xiaonan Gao

B. S. at East Tennessee State University, 2009

B. S. at Shandong Normal University, 2009

Director: Dr. Indika U. Arachchige

Assistant Professor, Department of Chemistry

Virginia Commonwealth University

Richmond, Virginia

April. 2016

Acknowledgment

First of all, I would express my appreciation for all the help from my advisor, Dr. Indika U. Arachchige, for all his support and guidance in my five years study at Department of Chemistry, Virginia Commonwealth University. Dr. Arachchige is not only an excellent advisor giving suggestions and discussion about my research and encouraging me to improve my work, but also a fantastic friend with patiently helping me for each detailed problem I faced in both research and work.

I would like to thank my committee members, Dr. Julio C. Alvarez, Dr. Hani El-Kaderi, and Dr. Arunkumar Subramanian for their support and willingness to offer any help when needed. Special thanks to all the current and past members in Dr. Arachchige's lab, including Lamia Nahar, Richard J Alan Esteves, Dr. Kulugammana Ranmohotti, Venkatesham Tallapally, Minh Ho, Jing Zhang, Ebetsam Eladgham and Dr. Gotluru Kedarnath, for all their support, advice and help.

I have been fortunate to work with my excellent collaborators and feel so grateful to them of for their help: Dr. Massimo F. Bertino and Lauren White at Department of Physics of Virginia Commonwealth University; Dr. Aiyun Fu at college of life science, Dezhou University, China; Ahmed Abozeed Farghaly at Department of Chemistry, VCU for his help on the methanol oxidation catalysis study; and Dr. Yang Liu at North Carolina State University for his help on STEM images. In addition, we thank the US National Science Foundation for an instrumentation award (CHE-1337700) which was used to purchase the Raman spectrometer used for characterization.

Finally, I appreciate all the support from my wife, Xueyao Wang, as well as my parents and all my friends, who have been continually encouraging and helping me throughout all my academic endeavors.

Table of Contents

List of Tables	vi
List of Figures	vii
Abstract	xii
1. Introduction	1
1.1 Classes of Nanomaterials and Properties.....	1
1.2 Nanoparticles Synthesis and Properties.....	3
1.3 Nanoparticles Assembly Methods.....	7
1.4 Sol-Gel Method.....	10
1.5 Aerogels.....	11
1.6 New Classes of Aerogel.....	12
1.7 Noble Metal Hollow Nanoparticle and Their Properties.....	15
1.8 Galvanic Replacement Reactions.....	16
1.9 Surface Plasmon Resonance.....	17
1.10 Surface Enhanced Raman Scattering.....	19
1.11 Methanol Oxidation Catalysis for Direct Methanol Fuel Cells.....	21
1.12 Thesis Statement.....	23
2. Experimental and Characterization Methods	27
2.1 Supercritical Drying.....	27
2.2 Powder X-ray Diffraction.....	29
2.3 UV-Vis Spectroscopy.....	33
2.4 Transmission Electron Microscopy.....	35

2.5 Scanning Electron Microscopy/ Energy Dispersive Spectroscopy.....	37
2.6 X-ray Photoelectron Spectroscopy.....	39
2.7 Inductively Coupled Plasma Mass Spectrometry.....	41
2.8 Surface Area and Porosimetry Analysis.....	42
2.9 Surface Enhanced Raman Scattering.....	46
2.11 Cyclic Voltammetry.....	48
3. Oxidation-Induced Self-Assembly of Ag Nanoshells into Transparent and	
Opaque Ag Hydrogels and Aerogels.....	52
3.1 Introduction.....	52
3.2 Experimental Section.....	53
3.3 Results and Discussion.....	55
3.4 Conclusion.....	78
4. Direct Cross-Linking of Au/Ag Alloy Nanoparticles into Monolithic Aerogels	
for Application in Surface Enhanced Raman Scattering.....	79
4.1 Introduction.....	79
4.2 Experimental Section.....	80
4.3 Results and Discussion.....	82
4.4 Conclusion.....	112
5. Sol-Gel Assembly of Ag-Pt-Au Alloy Ternary Nanoparticles into Metallic	
Aerogels with the Application on Methanol Oxidation Catalysis.....	113
5.1 Introduction.....	113
5.2 Experimental Section.....	114
5.3 Results and Discussion.....	116

5.4 Conclusion.....	124
6. Conclusion.....	127
References.....	131
Vita.....	154

List of Tables

Table 3.1 The volumes of AgNO ₃ , glutathione, NaOH, and NaBH ₄ used in the synthesis.....	54
Table 3.2 Physical properties of Ag NSs and corresponding aerogels.....	60
Table 4.1 Physical properties of Au/Ag alloy NPs and corresponding aerogels.....	95

List of Figures

Figure 1.1 Size range of the nanomaterials and comparative sizes of bulk materials.....	1
Figure 1.2 Schematic illustration of nanomaterials in different dimensions.....	2
Figure 1.3 Schematic view of laser ablation for synthesizing NPs.....	4
Figure 1.4 Chemical vapor deposition of synthesizing NPs.....	5
Figure 1.5 Colloidal synthesis of Ag nanoparticles.....	6
Figure 1.6 Layer-by-layer assembly of gold nanoparticles and polyimide.....	8
Figure 1.7 Schematic view of superlattices structure.....	9
Figure 1.8 An illustration depicting the porous architecture of silica aerogel.....	12
Figure 1.9 Schematic view of sol-gel condensation process of semiconductor nanoparticles into aerogel and xerogel.....	15
Figure 1.10 Schematic view of GRR between Ag hollow NPs and HAuCl_4	17
Figure 1.11 Schematic of localized surface Plasmon resonance of metal NPs.....	18
Figure 1.12 Schematic view of an incoming light got inelastically scattered when hitting on a substrate.....	19
Figure 1.13 Vibrational transition of a solid.....	20
Figure 1.14 A Schematic graph of the direct methanol fuel cell with Pt film as catalyst.....	22
Figure 2.1 Phase diagrams show temperature and pressure effect on material state.....	28
Figure 2.2 Schematic view of an atom excited by an external simulation.....	30

Figure 2.3 Reflection of X-rays from two planes of atoms in a crystal	31
Figure 2.4 Schematic illustration of X-ray diffraction instrument	32
Figure 2.5 Schematic view of electron excited by UV-Vis light.....	33
Figure 2.6 Schematic view of UV- visible spectrophotometer.....	34
Figure 2.7 Schematic view of the inside of TEM.....	36
Figure 2.8 Schematic view excitation of photoelectrons.....	39
Figure 2.9 The photoemission process of an excited electron escape from the orbitals.....	40
Figure 2.10 A representative N ₂ adsorption/desorption isotherm	44
Figure 2.11 Six types of basic adsorption/desorption isotherms.....	44
Figure 2.12 Categories of gas adsorption/desorption hysteresis loops	45
Figure 2.13 Schematic view of a sample on SERS substrate scattered incident laser beam.....	47
Figure 2.14 Schematic illustration of a reversible scan of CV.....	49
Figure 2.15 Schematic view of three electrode system of the CV for methanol oxidation catalysis experiment.....	50
Figure 3.1 UV-visible absorption spectra and a representative TEM of the solid Ag NPs.....	57
Figure 3.2 Normalize UV-visible absorption spectra of the as-prepared Ag hollow NSs.....	58
Figure 3.3 Transmission electron micrographs of the Ag hollow NSs.....	59
Figure 3.4 Photographs illustrating the transformation of Ag NS sol into an opaque gel.....	63

Figure 3.5 Photographs showing the condensation of opaque Ag sol into transparent Ag hydrogel.....	65
Figure 3.6 Powder X-ray diffraction patterns of the cubic Ag ₂ O NPs, Ag NSs, corresponding aerogel and xerogels.....	66
Figure 3.7 SEM images and EDS spectra of the as-prepared Ag aerogels and xerogels.....	67
Figure 3.8 The Ag (3d _{5/2}) and O (1s) XPS spectra of the precursor NSs and aerogels.....	69
Figure 3.9 The S (2p) XPS spectra of the precursor Ag NSs and the aerogels.....	70
Figure 3.10 Representative SEM images of opaque Ag aerogels and xerogels.....	71
Figure 3.11 TEM images of different aerogels.....	72
Figure 3.12 Representative TEM images of the opaque Ag aerogels.....	73
Figure 3.13 TEM images of the Ag aerogel prepared from transparent hydrogels.....	74
Figure 3.14 Nitrogen adsorption/desorption isotherms of precursor Ag NSs and corresponding aerogels.....	75
Figure 3.15 Nitrogen adsorption/desorption isotherm of the Ag aerogels.....	77
Figure 4.1 Representative TEM images of the Ag hollow NPs and SPR spectra.....	84
Figure 4.2 Low resolution TEM images of Au/Ag alloy NPs produced via GRR.....	85
Figure 4.3 Low resolution TEM images of Au/Ag alloy NPs produced with <i>m</i> value.....	87
Figure 4.4 TEM images of the precursor Ag hollow NPs and Au/Ag alloy NPs.....	88

Figure 4.5 TEM image of Au/Ag alloy I along with STEM-EDS elemental maps.....	89
Figure 4.6 STEM image of Au/Ag alloy II along with elemental maps.....	90
Figure 4.7 STEM-EDS elemental maps of Ag/Au alloy NP III.....	91
Figure 4.8 Normalized UV-Visible absorption spectra of Au/Ag alloy NPs.....	91
Scheme 4.1 A Schematic illustration of the oxidation-induced self-assembly of Au/Ag alloy NPs into monolithic aerogels for surface enhanced Raman scattering.....	92
Figure 4.9 Photographs illustrating the transformation of Au/Ag NP sol into a hydrogel.....	94
Figure 4.10 Solid state absorption spectra of Au/Ag aerogels.....	96
Figure 4.11 TEM images of Au/Ag alloy aerogel with magnified electron micrographs.....	98
Figure 4.12 STEM-EDS elemental maps of Ag/Au alloy aerogel I.....	99
Figure 4.13 STEM-EDS elemental maps of Ag/Au alloy aerogel II.....	100
Figure 4.14 STEM-EDS elemental maps of Ag/Au alloy aerogel III.....	101
Figure 4.15 Dark field STEM images of Au/Ag aerogels.....	102
Figure 4.16 PXRD patterns of Au/Ag alloy NPs with corresponding aerogel.....	103
Figure 4.17 Nitrogen adsorption/desorption isotherms of Au/Ag alloy aerogels.....	106
Figure 4.18 Nitrogen absorption/desorption isotherm of Au/Ag alloy NP.....	107
Figure 4.19 SERS spectra of Au/Ag alloy NPs and corresponding aerogels.....	109
Figure 4.20 Raman spectra of Rd 101 with no SERS substrate and Au/Ag aerogel III	

with different concentrations of Rd 101.....	110
Figure 4.21 Intensity histograms of SERS spectra of Rhodamine 101 in Au/Ag aerogels.....	111
Figure 5.1 Schematic view of GRR of Pt and Au on the Ag hollow NPs.....	116
Figure 5.2 UV-Vis absorption of Ag hollow NPs, Pt/Ag alloy hollow NPs1 and Au/Pt/Ag hollow NPs.....	117
Figure 5.3 TEM images of ternary Au/Pt/Ag hollow NPs.....	118
Figure 5.4 STEM image of Au/Ag alloy hollow NP along with elemental maps.....	119
Figure 5.5 Photographs showing the condensation of the formation of the hydrogel.....	120
Figure 5.6 TEM images of ternary hollow NPs formed aerogel.....	121
Figure 5.7 STEM image of Au/Ag alloy aerogel along with elemental maps.....	122
Figure 5.8 PXRD patterns of ternary hollow NPs and resultant aerogel.....	123
Figure 5.9 Nitrogen adsorption/desorption isotherms and pore width distribution of ternary aerogel.....	124
Figure 5.10 CVs for the electro-oxidation of methanol with different concentrations.....	126

ABSTRACT

SOL-GEL ASSEMBLY OF METAL NANOSTRUCTURES INTO METALLIC GEL FRAMEWORKS AND THEIR APPLICATIONS

Xiaonan Gao, Ph. D.

A dissertation submitted in partial fulfillment of the requirements for the degree of Doctor of
Philosophy at Virginia Commonwealth University

Virginia Commonwealth University, 2016

Advisor: Dr. Indika U. Arachchige

Assistant Professor, Department of Chemistry

The advent of nanoscience and nanotechnology has sparked many research forefronts in the creation of materials with control over size, shape, composition, and surface properties.^{1,2} However, for most of the applications, nanoscale materials need to be assembled into functional nanostructures that exhibit useful and controllable physical properties. Therefore, numerous efforts on the assembly of nanoparticles (NPs) using organic ligands, polymers and polyelectrolytes have been reported.^{3,4} However, the interactions between NPs are mediated by intervening ligands, which are detrimental to charge transport and limit the thermal stability. Hence, developing a new method to produce solid state nanostructures with direct NP linkage has become a significant challenge. To avoid the bridging ligands and improve the conductivity of NP based solid state structures, a novel strategy has been developed in which colloidal NPs undergo condensation to wet “jello-like” hydrogel with direct interfacial linkage. Then hydrogels

can be dried supercritically to produce aerogels.⁵ Resultant nanostructures exhibit low densities, large open interconnected pores, and high internal surface areas and are containing entirely of colloidal metal NPs.⁶ Since noble metal NPs have been widely used in applications such as catalysts, sensors, and novel electrochemical device components, we herein expanded the sol-gel method to noble metal NPs to produce a new class of metal aerogels.

In the dissertation, the synthesis of hollow Ag hollow NPs, Au/Ag alloy NPs, and Au/Pt/Ag alloy hollow NPs with tunable sizes and physical properties, and their oxidative-assembly into high-surface-area, mesoporous, self-supported gel framework has been achieved. The gelation kinetics have been controlled by tuning the oxidant/thiolate molar ratio that governs the rate of NP condensation, which in turn determines the morphology, optical transparency, surface area, and porosity of the gel frameworks. These low-density mesoporous nano-architectures displaying optical transparency or opacity, enormously surface area, and interconnected meso-to-macro pore structure are promising candidates for catalytic, electrocatalytic, and SERS-based sensing applications. The SERS activity of Au/Ag alloy aerogels has been studied and significant signal enhancement was achieved. The performance of the Au/Pt/Ag aerogel towards methanol oxidation reaction has been studied via cyclic voltammetry and significant electro-catalytic activity was observed.

Chapter 1: Introduction

1.1 Classes of Nanomaterials and Properties

In the past few decades, nanotechnology and nanoscience have gained significant interest that covers a wide range of fields, including chemistry,⁷⁻⁹ physics,¹⁰⁻¹² electronics,^{13,14} information storage,¹⁵ energy,¹⁶⁻¹⁸ and medicine¹⁹. This is not only because nanotechnology can fulfil currently challenging demands in these areas, but also offers new perspectives for investigating the nanoscale world.^{20,21} Basically, the definition of nanomaterials qualifies two criteria: the size at least in one-dimension is between the range of 1 – 100 nm (Figure 1.1),²² and displaying unique properties other than the bulk materials. Nanomaterials have become the foundation of nanotechnology and opens a novel field for a large number of emerging applications.¹ Typically there are four different classes of nanomaterials: 0-dimensional materials, such as nanoclusters and nanoparticles (NPs); 1-dimensional materials, including nanotubes, nanorods and nanofibers; 2-dimensional materials, like nanofilms and nanoclays; 3-dimensional materials, such as polycrystal (Figure 1.2).^{20,23-26}

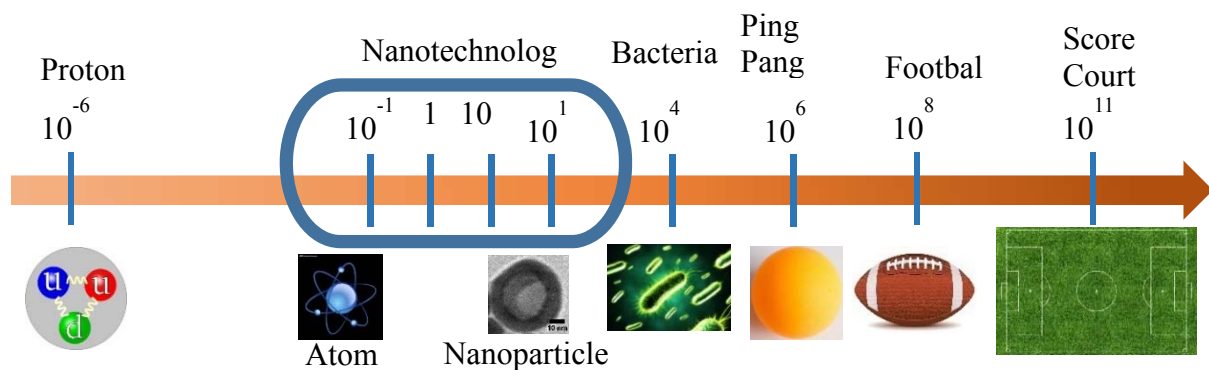


Figure 1.1: Size range of the nanomaterials and comparative sizes of bulk materials.

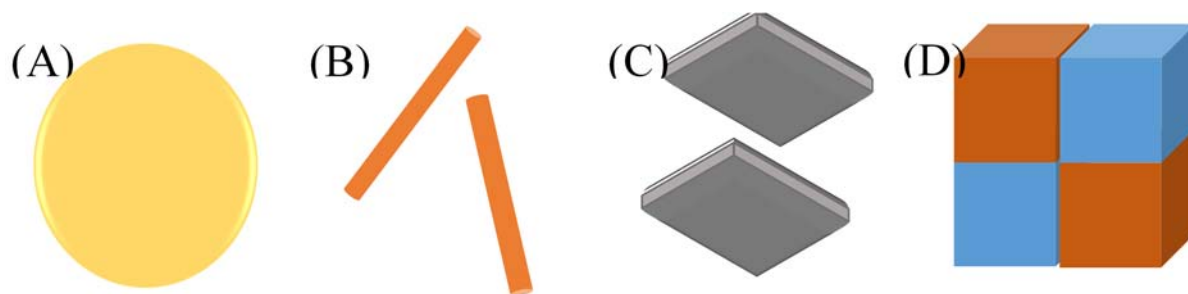


Figure 1.2: Schematic illustration of nanomaterials in (A) 0-D nanoclusters or nanoparticles, (B) 1-D, nanotubes, fibers or rods, (C) 2-D, films or coats, and (D) 3-D, polycrystals.

Among those classes of the nanomaterials, the unique 0-D nanostructure exhibit properties sparking many research forefronts in the creation of such objects with control over size, shape, and surface properties.^{27,28} When the size of NPs approaches the nanoscale, there is a significant percentage increase of the atoms on the surface which dramatically increases the surface to volume ratio. For comparison, such aspect ratio in the bulk material is quite minuscule.²⁹⁻³¹ Therefore, NPs exhibit unique and interesting properties relative to bulk materials, including surface Plasmon resonance in metal NPs,^{32,33} size-dependent photophysical properties such as quantum confinement in semiconductor NPs,^{34,35} extraordinary catalytic properties of metal NPs,^{32,33} and etc. In case of that, rational design, synthesis and characterization, and utilization of nanomaterials have gained a lot of attention since last century. In this regard, tremendous effect has put onto the investigation of the NPs science, including carbon based NPs,³⁶ metal oxide NPs,³⁷ quantum dots,³⁸ elemental metallic NPs,³⁹ and organic polymers.⁴⁰ Research in this dissertation is devoted to noble metal NPs (Ag, Au, and Pt) because of their unique catalytic activity, plasmonic tunability, and increased surface reactivity.

1.2 Nanoparticles Synthesis and Properties

Due to the importance of the NPs, there have been thousands of reports describing synthesis of different material, with morphology, size and composition control.^{31,36,41-43} Basically, it can be divided into two categories: bottom up approach and top down approach. In the bottom up approach, the synthesis usually starts with atoms or ions, which can attract other atoms or ions to form a clusters or NPs.⁴⁴ On the other hand, top down approach starts with bulk materials, which can be mechanically reduced in size to approach into nanoscale.⁴⁵

In addition, NP synthesis can be approached not only by chemical methods, but also physical methods. In the physical methods, there are microwave synthesis,^{46,47} ultra-sonication, irradiation, laser ablation,⁴⁵ ball milling, and electrochemical synthesis.⁴⁸ However, chemical methods involve chemical vapor deposition,^{49,50} sol-gel method,⁵¹⁻⁵³ inert condensation method⁵⁴ and colloidal synthesis.⁵⁵⁻⁵⁷ Among these methods, laser ablation, chemical vapor synthesis and colloidal synthesis, are the three common approaches for NP synthesis.

1.2.1 Laser Ablation

Laser ablation in solid-liquid interface is a quite famous method for fabricating self-organized nanostructures on the solid surface. A high energy pulsed laser first irradiate onto a solid target in the liquid medium, and due to the instability of evaporation of the liquid which surrounds the irradiate target, NPs can be produced and attached to the surface (Figure 1.3).⁴⁵ By applying different lasers, various ablation nanomaterials (metal, oxides, carbides, hydroxides) with size and morphology (NPs, nanotubes, and nanorods) control can be obtained.^{28,58-60} The ablation products further react with the solution in order to produce the final nanostructure. The laser ablation method can result NPs with significant dispersibility, high purity and stability.

However, it still requires specific instrument and environment, which is expensive and not commonly used.

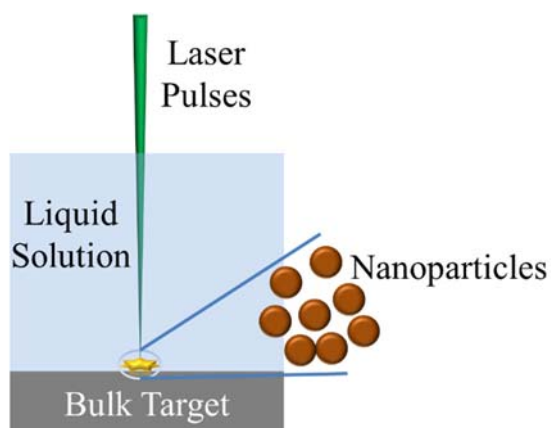


Figure 1.3: Schematic view of laser ablation for synthesizing NPs.

1.2.2 Chemical Vapor Deposition (CVD)

CVD is commonly used for producing thin film in the past decades. Typically, the reactants are firstly heated at high temperature in order to evaporate to a gas phase, then it can react with other materials to deposit onto the substrate surface resulting multilayers.⁴⁹ However, in this approach, CVD has been expanded into producing numerous types of materials with different structures, properties, and phases of precursors. Therefore, a mixture of gas reactants can be loaded into a reaction chamber, and after chemical reaction among the gas phase molecular stimulated by heat, plasma or laser, the products can be obtained out of the chamber.⁵⁰

CVD can also applied to produce NPs. Similar to other CVD synthesis, the precursor materials were first burned by plasma to yield a vapor phase, and then injected into a hot chamber. With addition of other vapor phase reactants, the chamber is over saturated with all reactant, which is called as “chemical supersaturation”. The precursors which is in the nanoparticulate form started to homogeneously nucleate into small size NPs seeds. Once the

seeds formed, the remaining reactants tend to condense onto the surface of the seeds, resulting a NP growth, but rather than further nucleation (Figure 1.4). Therefore, besides the residence time inside of the chamber, gas flow rate and pressure inside of the chamber are also two key parameters to tune the size and morphology of the NPs. More importantly, CVD also process NPs with multiple precursors at the same time, which make it an outstanding method for producing alloy NPs or doped NPs.

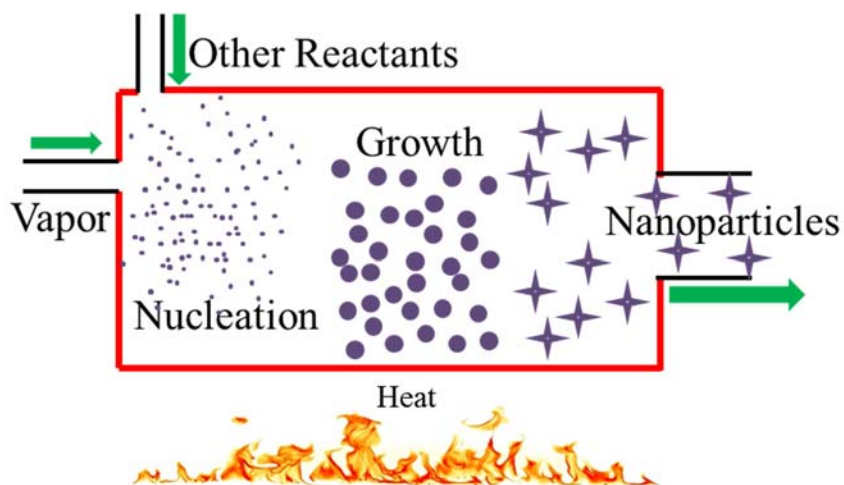


Figure 1.4: Chemical vapor deposition of NPs synthesis

However, during the synthesis of the NPs, the agglomeration always leads NPs aggregate into big chunks. Even there has been tremendous effect on redispersing or loosening the agglomeration, there are still chunks left in the product. In addition, the size dispersity is not easy to control in this method, and also it is not cost effective. Therefore, finding simple, easy and less cost method for synthesis of NPs is needed.

1.2.3 Colloidal Synthesis

There are numerous methods of solution phase synthesis of NPs, including reverse micelles synthesis, hydrothermal synthesis, sonochemical synthesis, polyol synthesis and

colloidal synthesis.^{31,61-63} Compared to other synthetic methods, solution based colloidal synthesis has significantly control over shape, size and morphologies.^{64,65} The colloidal synthesis normally has three consecutive steps: NPs' seed nucleation in the homogeneous solution, seed growth, and isolation of particles that reach the desired size. In addition, the colloidal synthesis usually require simple experimental equipment and chemicals at room temperature to obtain high quality nanomaterials. Accordingly, colloidal NPs can be synthesized through reacting appropriate salt precursors. The nucleation and growth of NPs process in the solution with presence or organic coordination ligands that dynamically adhere onto the NPs surface. The coordinating ligands that perform as a stabilizer, usually include but not limited to long-chain carboxylic acids, alkanethiols, alkylamines, and alkylphosphine oxides.⁶⁶⁻⁶⁸ The ligand molecules can tube the kinetics of the reaction process and also growth rate. Therefore, finding a proper solvent, ligand, precursor salt and reaction conditions for the colloidal synthesis becomes quite important. Figure 1.5 shows a typical colloidal synthesis of Au NPs. In this reaction, HAuCl_4 was chosen as the precursor salt and dissolve in the water solution. Citric acid was used as the surface capping ligand. With a dropwise addition of NaBH_4 aqueous solution, the solution turned from yellow color to either purple or pink indicating the formation of Au NPs.⁶⁹

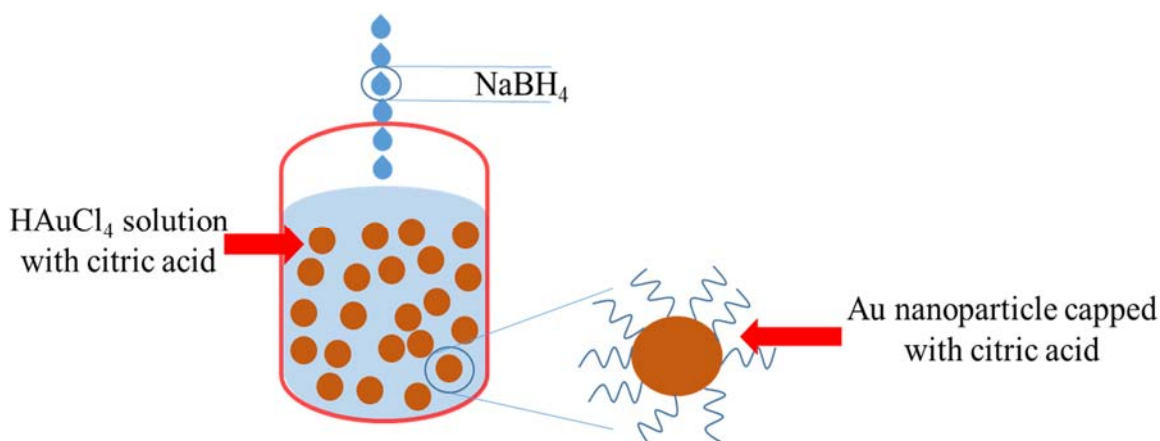


Figure 1.5: Colloidal synthesis of Ag nanoparticles.

However, the colloidal synthesis doesn't always produce the monodisperse NPs, since the growth of NPs depends on several different factors such as reaction time, concentration, choice of ligands, precursor to reducing agent ratio, and temperature. In addition, the shape and morphology of the NPs can be hardly controlled and often not very reproducible. More importantly, the surface atoms are stabilized because of the coordinating ligands, which are the drawback for direct NPs linkage and fast electron conduction after assembling them into solid state materials. However, from a device performance perspective, many applications require assembly of discrete NPs into functional solid state structures that exhibit controllable morphologies and physical properties. Therefore, assembling the NPs into functional architectures with useful and controllable physical properties is a great challenge.

1.3 Nanoparticles Assembly Methods

Numerous efforts on the assembly of nanomaterials have been reported to date, such as covalent coupling of NP surface groups,^{70,71} controlled evaporation of the solvent to produce ordered supercrystals^{3,72} or non-ordered glassy films,⁷³ and polymer or bimolecular mediated self-assembly.^{25,74,75} Among them, layer by layer assembly and superlattices formation have gained notably interest in recent years,^{72,76-79} and they are discussed below.

1.3.1 Layer by Layer Assembly

Layer by layer self-assembly method was first introduced to multilayer architectures on a non-planar surface in the later 1990s. It follows a bottom-up strategy for assembling a large number of single layers or hierarchical nanostructures. Uniformed thin films that consist functional groups on the surface are served as substrate. Monolayer of NPs formed on the surface based on the electrostatic interaction between the surface and NPs. Followed with the first

monolayer formation, polyelectrolyte deposited onto the layer and then attracted other NPs to build the next layers. This process can be reproduced for hundreds of times to produce a thick multilayers of NPs (Figure 1.6).⁸⁰ By using different kinds of NPs, capping ligands, or polyelectrolytes, layer by layer assembly can offer different superstructures with promising collective and improved functional properties for multiple applications including advanced absorbents or catalyst.

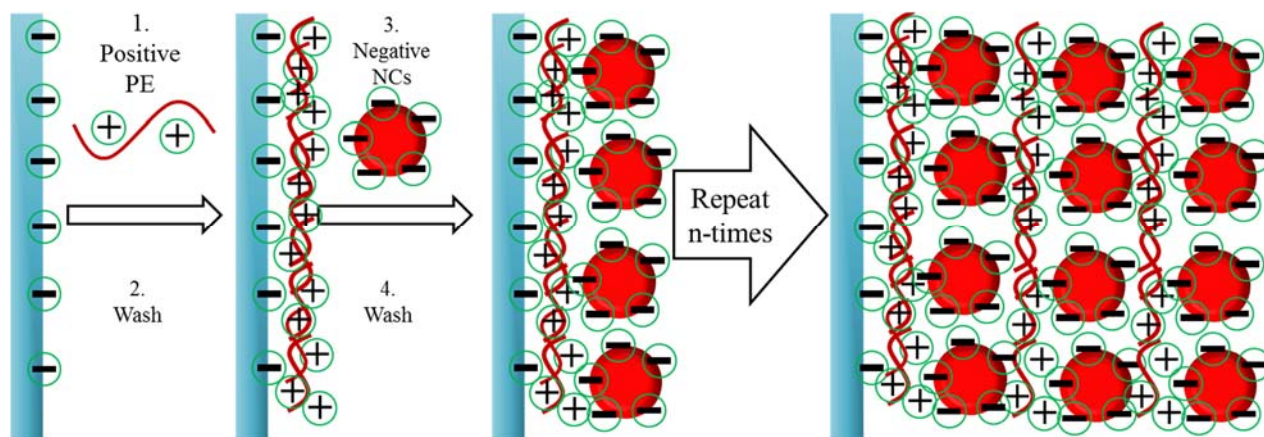


Figure 1.6: Layer-by-layer assembly of gold nanoparticles and polyelectrolyte fabricated on amine-terminated substrate.

1.3.2 Superlattices Formation

Recently, a proof-of-concept in which monodisperse NPs of inorganic solids are self-organized into ordered superlattices or glassy films through controlled evaporation of the solvent has received considerable interest. The superlattices structure accentuates the alternating setting of layers while keeping the barrier width thin enough so wave function can't decay to zero in the adjacent wells. It has also been developed to hybridization of metal NPs and semiconductor NPs in order for more applications. Such hybrid nanocrystal superlattices can combine the each NPs' properties and exhibit new properties from the interactions between the two. To date, there has

been a decent amount of reports discussing about the hybrid NPs glassy solids that show properties of each precursor NPs.^{3,72,73,78,79} Such as semiconducting lead selenide with Au NPs (Figure 1.7),⁸¹ Typically, a carbon or silicon oxide coated TEM grid is used as a substrate and placed into a Au and PbSe NPs colloidal solution. By keeping at 60°-70° at a low pressure chamber for a certain amount of time, the binary superlattices formed. It provides a new approach for engineer magnetic, electronic and optical properties of NP assembly.

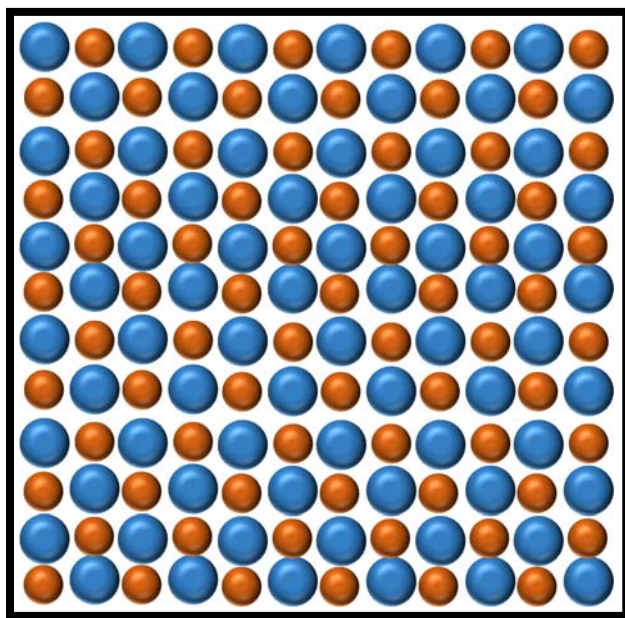


Figure 1.7: Schematic view of superlattices incorporated with semiconducting lead selenide and metallic gold nanoparticles

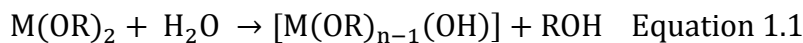
However, from a device performance perspective, the interactions between nano-sized units are essentially mediated by organic transformations, presence of which is detrimental to charge transport properties and limit the thermal stability of the assembly. Hence, investigation of new methods for the direct self-assembly of NPs into solid state structures is an important challenge for many applications. In this regard, sol-gel method caused our interests, since the

colloidal NPs can be directly self-assembled into high surface area self-supported superstructures without any intervening ligands.

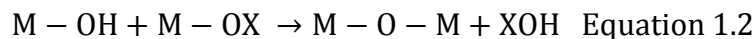
1.4 Sol-Gel Method

Sol-gel method has been known for many years and it has been extensively studied for gelation in metal oxides.^{5,6,82} A sol is a fluid colloidal system formed by the dispersion of colloidal nanoparticles (1-100 nm) in a liquid. Gel is a non-fluid heterogeneous system of liquid molecules dispersed in a solid medium with a semi-rigid jelly-like interconnected 3D network and pores in the sub-micrometer range. It was first established that metal oxide gels (e.g. SiO₂) that can be prepared through the hydrolysis and condensation of a liquid silicon alkoxide sol (Equation 1.1 and 1.2).⁵ Generally, the hydrolysis and condensation are slow processes occurring simultaneously and kinetics of the reactions is pH dependent. Under acid-catalyzed conditions, the silica monomers will polymerize mostly in linear-like structures/gels with a small degrees of cross-linkage due to the enhancement in the rate of the hydrolysis reaction over that of the condensation reaction. In the base-catalyzed reactions, highly cross-linked branched gels are produced when the rate of the condensation is higher than that of the hydrolysis. The resultant wet-gels can be dried via two different techniques: bench top dried method can evaporate the solvent to form condensed xerogels, but supercritical drying can retain the porous polymeric structure to produce an aerogel.

Hydrolysis of metal alkoxides:



Condensation of hydroxylated species:



1.5 Aerogels

Aerogel are a unique class of porous inorganic polymers that exhibit high surface area, solid contents ranging from 1-15% by volume, and densities as little as three times that of air. As such, they are ideal substrates for catalyst and sensors, and are excellent thermal insulating materials.^{5, 82-84} One of the unique features of the aerogel that makes it useful for a variety of applications is the continuous micro-(<2 nm) to meso-(2-50 nm) pore structure, which provides a facile conduit for molecules to reach the nanostructure surface. To date, a great deal of research has been conducted on aerogels based on metal oxides, amongst the traditional SiO₂, Al₂O₃, and TiO₂ are the widely studied systems.⁵ Recently, the extension of sol-gel strategy to produce metal chalcogenide,⁸⁵⁻⁸⁹ pnictide,⁹⁰ and metal aerogels^{91,92} was realized through oxidation-induced self-assembly of pre-formed NPs. The gel frameworks composed entirely of NP colloids represent an emerging class of low-density, high-surface-area, conducting superstructures in which the nanosized solids are assembled into pearl-necklace architectural model of the base catalyzed silica aerogels, without the use of intervening ligands and substrate supports that can limit the charge transport and thermal stability (Figure 1.8). However, the creation of such superstructures has been largely limited to solid NP building blocks, leaving behind opportunities to design novel nanostructures with unique and potentially tunable morphologies and physical characteristics. Therefore, we aimed to investigate the sol-gel assembly of noble metal NPs into porous aerogel superstructures.

On the other hand, if the hydrogel gets dried on the benchtop under ambient condition, there is an unhindered shrinkage due to the capillary forces of the solvent molecular evaporating from the network pores. The xerogels show a similar microstructure with both micropores and

mesopores but with a much denser network of the NPs, since majority of the mesopores and macropores collapsed during the drying process because of the surface tension of the solvent.

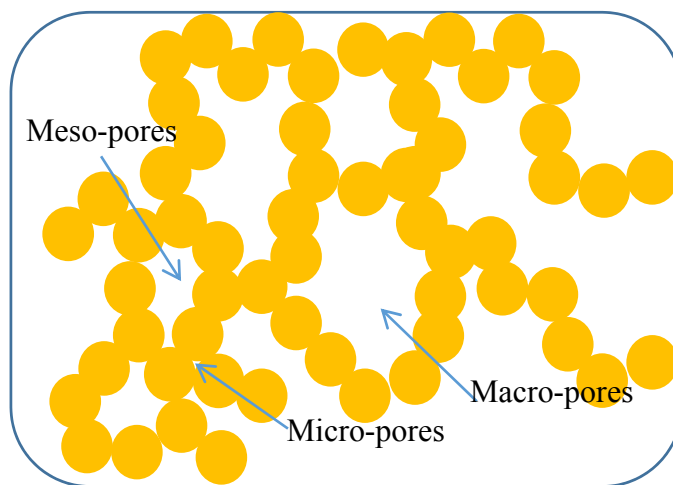


Figure 1.8: An illustration depicting the porous architecture of a based catalyzed silica aerogel.

1.6 Classes of Aerogels

As discussed in Chapter 1.5, although the aerogel started with metal oxides, there are still a lot of extensions such as metal aerogels and semiconductor aerogels. All the three classes of aerogel are discussed as follows.

1.6.1 Metal Oxide Aerogels

Silica aerogel is the most famous metal oxide aerogel and have been well established already. There have been tremendous amount of reports about the choice of precursor, the control of the synthesis, and tenability of both physical and chemical properties.⁸³ The unique properties such as optical and thermal conductivity and high surface area lead the silica aerogels to be used in many applications. The applications of silica aerogel includes catalytic supports, thermal insulation, detectors and etc.^{11,23,93,94} In addition, Alumina aerogels also caused a lot of interest. By tuning precursor alkoxide, the ratio of alkoxide to water, hydrolysis rate, drying

temperature, and pH of the solution, the final aerogel product varies from monolithic to powder, heterogeneous to homogenous, and amorphous to crystalline.⁹⁵ Moreover, anatase aerogel has gained attentions with high crystallinity, transparent monoliths, and mesoporous structures at low temperature.⁹⁶ Besides the main group elements, considerable work has been done on the lanthanide and actinide oxide aerogels too.

1.6.2 Metal Aerogels via Carbothermal Reduction

Metal aerogels attracted a lot of research interest in the past decades because of their unique optical, magnetic, catalytic, biological and sensing properties. Started in 2005, Dr. Tappan et al. first developed combustion synthesis method to produce a class of nanoporous iron foams that is similar to aerogel superstructure.⁹⁷ Then this method was applied with Cu and Au to yield nanofoams too. Another method to produce aerogel like structure is to dealloy metal-template alloy network. Until 2009, Dr. Leventis' group reported the nanosmelting method for producing iron aerogels.⁹⁸ A combination of iron oxide gel and resorcinol-formaldehyde polymer gel were mixed and molded to form a hybrid gel. Then the gel was dried supercritically producing a hybrid aerogel, followed with pyrolysis under Argon at 1000 °C. Interestingly, the resorcinol-formaldehyde dehydrates to carbon and further reduce the iron oxide to Fe, with the formation of CO₂. However, such method doesn't apply to all metals, especially for noble metals which can be hardly reduced. Also, the shape control is difficult due to the high temperature pyrolysis. Therefore, developing methods for metal aerogel synthesis with noble metals is needed to meet the potential applications of catalysis and chemical sensing.

1.6.3 Semiconductor Aerogels

Afterwards, there has been a dramatic change for the sol-gel technology which discussed in the previous section. Instead of a continuous process from the precursor molecule to the gel, the gelation of NPs forms random porous building blocks instead of precipitation. Instead of metal oxide, semiconductor aerogels are a novel class of aerogels that made of metal chalcogenide NPs. It was first reported by Dr. Gacoin group in 2001,⁸⁷ and then Dr. Brock's group carried on and expand the "sol-gel" into a new condensation strategy.^{53,88,99} Similar to hydrolysis and condensation, the semiconductor NPs such as CdSe, CdS, or CdTe that capped with thiolates, were first undergo an oxidative reaction to withdraw the surface thiol ligand and then created active sites on the highly reactive surface in order to connect with another NP. Such connection overcomes with the polyelectrolyte and intervening ligand problem, building direct interfacial linkages and highly porous hydrogel structure. By solvent exchanging and supercritical drying, semiconductor aerogels with interconnected meso- to macro-pores, optical translucency and photoluminescence properties are produced (Figure 1.9).⁸⁹ Comparing different drying techniques, the CdS xerogel exhibit quite dense structure compared the CdS aerogel. The surface area of the CdS aerogel hits 250 m²/g, which makes it a promising material for catalysis and sensing.¹⁰⁰

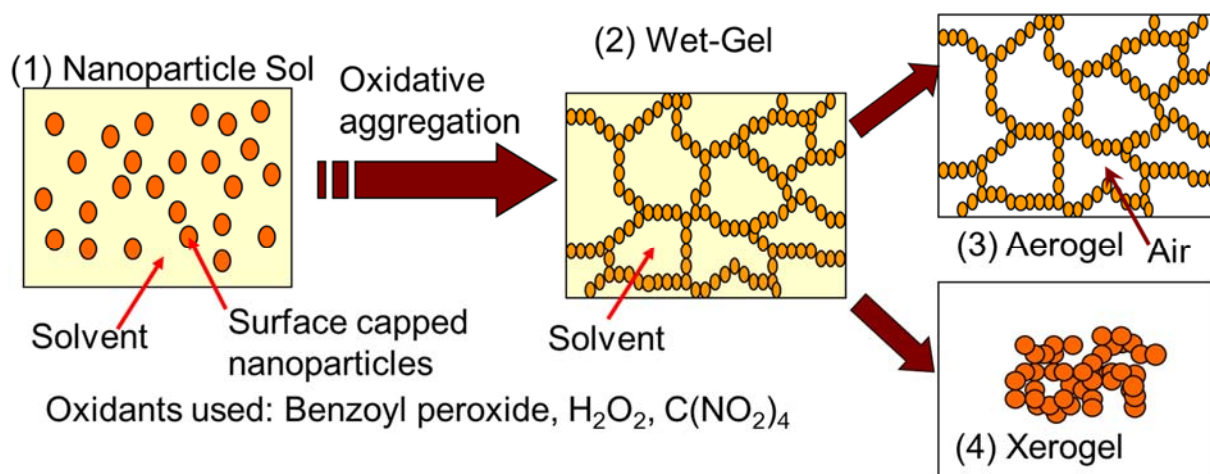


Figure 1.9 Schematic view of sol-gel condensation process of semiconductor nanoparticles into aerogel and xerogel.

1.7 Noble Metals Hollow Nanoparticles and Their Properties

Metal NPs mainly described the transitional metals such as Fe, Zn, and Co also noble metal elements including Ag, Au, Pt, and Pd. There have been numerous applications of metal NPs in many fields: catalysis, optics, biosensors, SERS, charge transport, solar cell, fuel cells and etc. Take Au NPs for example, it has been widely used in the drug delivery and CO oxidation catalysis. Nanomaterial with hollow interiors have received significant interest from the materials research community due to their unique physical properties that can be tuned by engineering the size, shape, composition, and shell thickness.¹⁰¹ In particular, hollow NSs of Au and Ag metals are known to exhibit plasmonic and catalytic properties very different from (or in some cases superior to) corresponding solid counterparts. For instance, Zhang and coworkers have demonstrated that the surface Plasmon resonance (SPR) of Au NSs can be smoothly tuned over a wide spectral region (550-820 nm) by controlling the diameter and shell thickness.^{102,103} Such tunability of plasmonic has also been reported for silica-core/Ag-shell nanostructures. In addition, hollow NSs of traditionally expensive noble metals are cost-effective, low-density

materials with all active surfaces without dead interiors.¹⁰⁴ Moreover, it is well known that the NP morphology plays a crucial role in catalysis and the hollow NSs of noble metals supported on porous substrates have been reported to exhibit superior catalytic activity than solid counterparts.¹⁰⁵⁻¹⁰⁹ However, the assembly of such materials into high-surface-area, self-supported gel frameworks composed entirely of NSs has not been reported. Recently, Eychmüller et al. demonstrated the cyclodextrin-mediated assembly of Pt NPs into aerogels.^{91,92,110,111} Very recently, our group reported the synthesis of Au/Ag and Pt/Ag, alloy aerogels via salt-mediated cross-linking of negatively charged hollow particles.¹¹² Despite recent successes in the formation of monometallic (Au, Ag, and Pt) and heterogeneous (Ag-Pt and Ag-Au) bimetallic solid NP-based aerogels, the creation of such superstructures based entirely on catalytically important metal hollows has not been reported.

1.8 Galvanic Replacement Reactions

In the last decade, the galvanic replacement reactions (GRR) have been extensively studied on metallic nanostructures. Significant interests have been putting on direct synthesis of NPs, nanotubes, nanoshells and etc. via GRR. The GRR is an irreversible reaction between colloidal soluble solid materials and metal ions in the solution. Due to the difference in the standard reduction potentials of the two metals, the reaction can lead to the deposition of the metal ion with higher standard reduction potential onto the material surface, and oxidize the metal with lower potential into ion to dissolve into the solution.^{113,114} For example, GRR offers a simple but versatile route for producing Au/Ag alloy hollow NPs (Figure 1.10). Ag/Ag⁺ has a standard reduction potential at +0.79 V and Au/Au³⁺ is +1.50 V, so when HAuCl₄ solution was added into the Ag hollow NP solution, the GRR between these two metals occurs immediately. Ag would be oxidized into Ag⁺ and bind with Cl⁻ to form AgCl that is highly insoluble in the

solution, but Au^{3+} can be reduced to Au and deposit onto the surface of NPs. (Equation 1.3)
 Since Au and Ag both have face-centered cubic structure with similar lattice constants (4.0786 Å for Au and 4.0862 Å for Ag), it can form an alloy NP surface.¹¹⁵

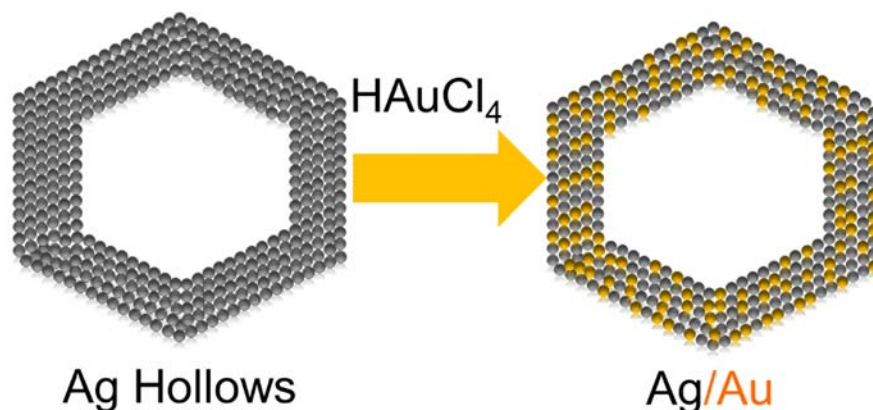
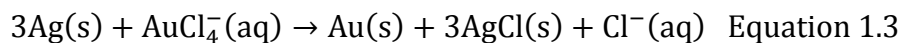


Figure 1.10 Schematic view of GRR between Ag hollow NPs and HAuCl_4 to form alloy NPs.

1.9 Surface Plasmon Resonance

There has been over a 100 years history for the SPR. In the past few decades, SPR has attracted lots of interest not only because it is powerful and sensitive spectroscopic technique, but also convenient and cost effective. When an incident light or beam goes through the solution, it can stimulate resonant oscillation of the conduction electron at the interface between a negative and positive permittivity material. If the frequency of the incident beam is similar to the natural frequency of the surface electrons oscillating against the restoring force of positive nuclei, the surface Plasmon resonance can be observed. Specifically, when it comes to the metal nanoparticles, such as Ag or Au NPs that size is comparable or even smaller than the wavelength of the incident beam (usually between 200 – 800 nm), the electric fields near the surface of the NPs can be significantly enhanced. However, because of the size of the NPs is smaller than 100

nm, the shorter field decay length can reduce the sensitivity for interference of the solution refractive index fluctuations while giving enhanced sensitivity to refractive index changes on the surface. In this case, the free conduction electrons in the metal NPs are driven into oscillation due to strong coupling with incident beam (Figure 1.11).^{116,117} The NPs optical absorption has a maximum at the Plasmon resonant frequency, which is called as the SPR of the metal NPs.

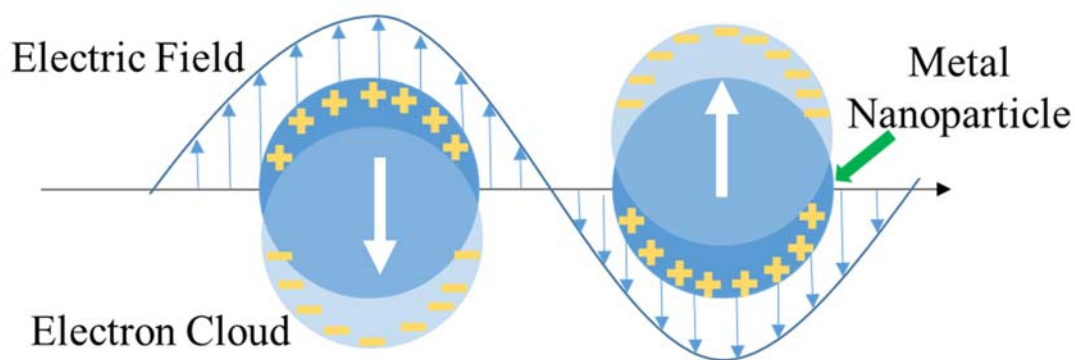


Figure 1.11: Schematic of localized surface Plasmon resonance of metal NPs.

Metal NPs SPR has been proved that it is sensitive to dimensionalities, morphology, and also size.¹¹⁷ For instance, in metal NPs, high surface to volume ratio results in more surface energy for NPs so that SPR can be tuned as a function of sizes, such as the color change in hollow Au hollow NPs going from blue to red and SPR shifted from 520nm to 840 nm.¹¹⁸ In addition, with the increase of the diameter, the full width at half maxima of the spectra also become larger, which produce broader spectra. That is caused by either the dominance of non-radiative decay from the absorption, or homogeneous/inhomogeneous distribution of the materials. The strong localized SPR in nanostructures exhibit novel phenomena like optical force enhancement, surface-enhanced sensing, transport and storage of energy, and NPs' growth control. Therefore, SPR provides a novel way for developing more complicated NPs with predictable optical response.

1.10 Surface Enhancement Raman Scattering

Surface enhanced Raman scattering (SERS) has been developed as an analytical tool to probe the molecular vibrations in the close proximity of metallic nanostructures. It provides significantly enhanced Raman signal from Raman-active analyte molecules such as Rhodamine 6G that can be absorbed onto metal substrate. When an incoming light hits the substrate, the photons can be scattered either elastically or inelastically. The elastically scattered light keeps the same wavelength as the incident light, which also means energy keeps the same. However, the energy of the inelastically scattered light changes compared to the incident light (Figure 1.12).^{119,120}

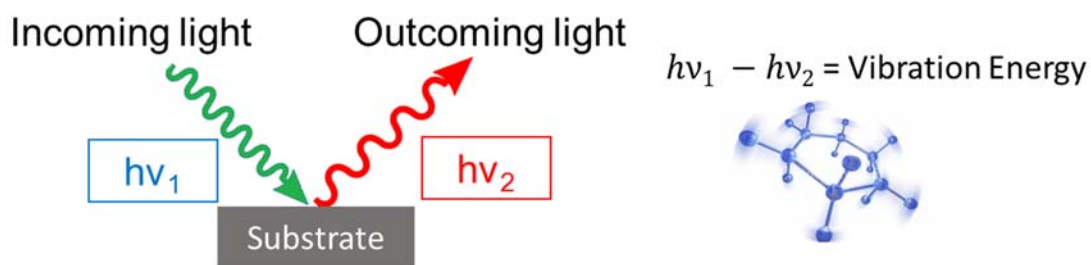


Figure 1.12: Schematic view of an incoming light getting inelastically scattered when hitting on a substrate.

The inelastically scattered light is defined as Raman scattering. The energy difference between the two lights is due to the nuclear motions of the molecules. As shown in Figure 1.13, bottom two lines are representing ground vibration state (L) and excited vibration state (M), where top two lines are meaning the virtual state which is an intermediate state. When the molecule absorbs energy in the ground state, the energy difference is defined as Stokes shift. The reverse shift happens when the molecule comes back from the excited state to the ground state, called as anti-Stokes shift. Such energy difference is the Raman shift.

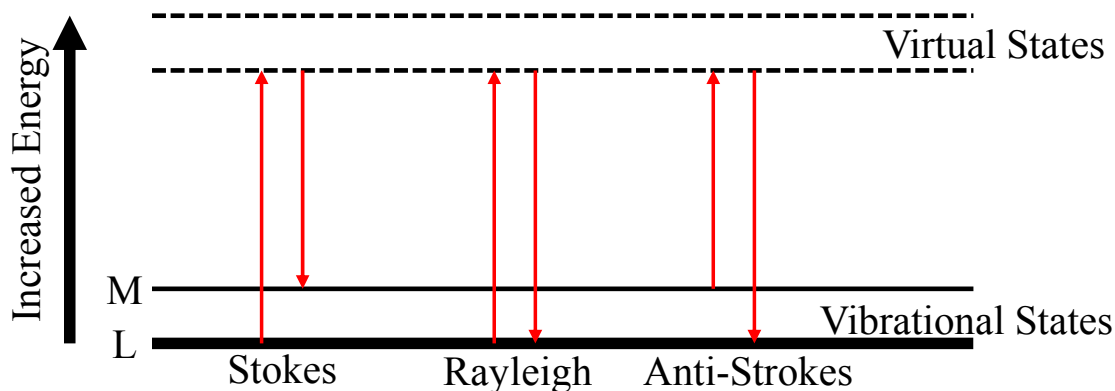


Figure 1.13: Vibrational transition of a solid.

Since the Raman shift is weak and hardly detectable, there has been a lot of effort done to enhance the signal. So far, there are two types of mechanism for the enhancement in SERS: chemical enhancement and electromagnetic enhancement. For chemical enhancement, the chemisorption of the analyte can be changed, such as tuning the catalytic properties or just simply elemental composition of the substrate. Such adsorbate-surface interaction can either amplify or deflate the signal enhancement. More importantly, the electromagnetic enhancement, which is the dominant effect, depends on the metal surface's roughness features.¹²¹⁻¹²³ The comparison of the signal intensity between enhanced single to the analyte by itself is usually called as enhancement factor (EF). Regularly the EF can be around the order of $10^4 - 10^6$, sometimes even as high as $10^8 - 10^{14}$ for outstanding substrate.

The surface enhanced Raman scattering requires interaction between the target material and substrate. Common SERS substrates include Au, Ag and Cu, because of their LSPR covering Raman range (the visible light to near IR). To date, a large number of reports about improving the SERS effect and optimizing the substrate has been done. Prominent SERS effects are reported to occur at the plasmonic NP aggregates where intense electromagnetic fields are generated at the interparticle cervices (i.e. hot-spots).^{124,125} Therefore, SERS has significantly

increase the surface selectivity and sensitivity of Raman spectroscopy, providing an outstanding interfacial system for in-situ and ambient analysis of catalytic, biological, and electrochemical applications.

1.11 Methanol Oxidation Catalysis for Direct Methanol Fuel Cells (DMFC)

Over the past few years there has been tremendous interest in using supported and unsupported metal NPs as catalysts for applications in fuel cells,^{6,108,126-131} exhaust systems as well as variety of oxidation,^{127,129,132} reduction,^{105,133} and hydrogenation^{36,134} reactions. Among them, the DMFC (Figure 1.14) has attracted much attention as a portable energy source and Pt based NP systems (Pt, Au/Pt,^{126,127} Co/Pt,^{108,128} and Ru/Pt^{129,130}) have been extensively studied as catalysts for energy generation. Inside of the DMFC, on the anode side a flow of methanol with water can interact with the catalyst layer on the electrolyte, which can be oxidized into CO₂ and H⁺ and receive electrons simultaneously (Equation 1.4). On the other hand, at cathode side a flow of O₂ can be reduced at the catalyst layer on the electrolyte, as well as donating electrons out to the anode side (Equation 1.5). During this process, electrons are transported through an external circuit to provide electricity power. Moreover, during the catalytic process of methanol on the Pt based catalyst, CO can also formed due to incomplete oxidation of methanol. CO can bind with Pt strongly to perform as a catalyst poison. In order to avoid this problem, Au is often alloyed into the catalyst which can further oxidize CO into CO₂. Therefore, developing Au/Pt/Ag hollow NPs can make a better promising material for DMFC applications.

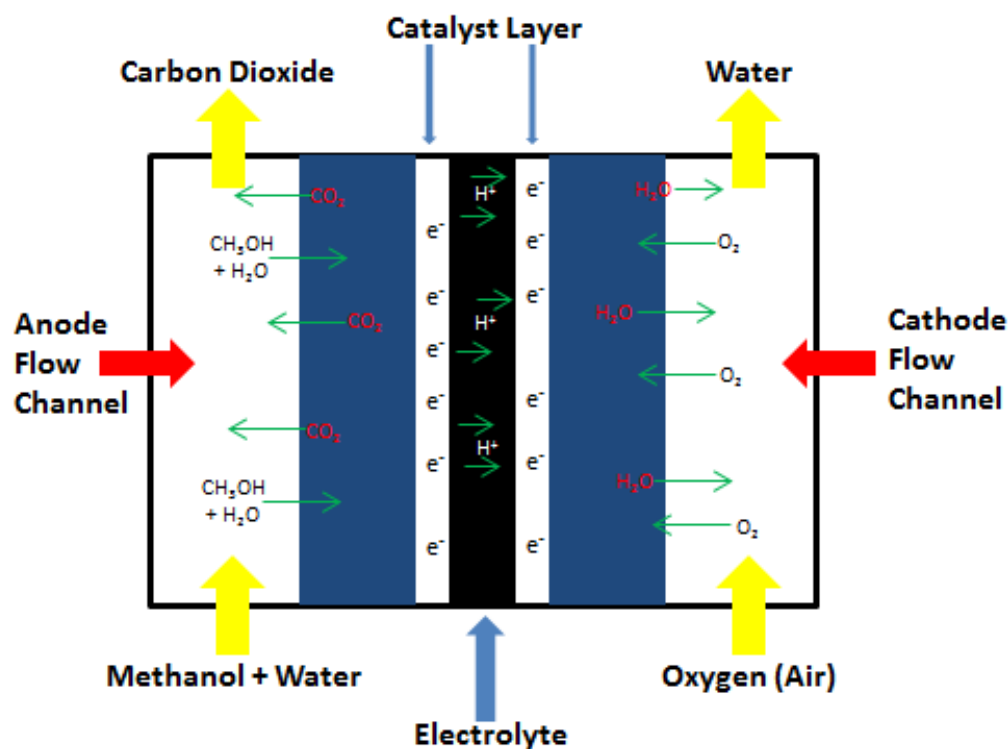
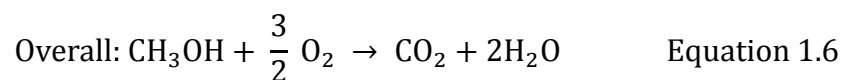
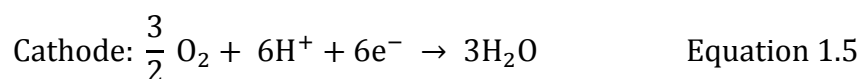
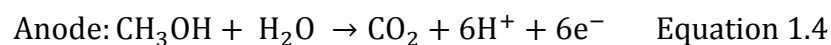


Figure 1.14: A Schematic graph of the direct methanol fuel cell with Pt film as catalyst.



In general, DMFC studies are based on supporting the catalytically active material on a mesoporous substrate (typically carbon^{23,135}) and testing the performance of the composite as a catalyst. One important aspect in constructing a high performance fuel cell catalyst is to have a good dispersion of NPs throughout the catalyst support. Many reports indicate that supported catalysts limit their efficiency due to agglomeration of NPs inside or on the surface of the support leading to pore blockage, interruption of mass transport routes as well as uneven loading

and poor utilization of the catalytically active material.^{6,127-129} In contrast, the assembly of metal hollow particles into 3-D connected gel frameworks will eliminate the necessity of substrate supports, providing self-supported nanostructures with approximately uniform dispersion of hollow NPs. Furthermore, inherently random yet continuous meso-to-macropore network that wraps around catalytic particles offers transport routes even around pore blockages and large aggregates. Moreover, the combination of hollow NPs and the pearl necklace architecture of the aerogel provides low cost materials that are atom efficient than conventional NPs and supported catalysts. Hence, these unique nanostructures displaying maximum active surface area per mass unit would be truly new materials with unmatched potential in heterogeneous catalysis. Accordingly, we intend to investigate the use of Au/Pt/Ag aerogels in DMFC studies.

1.12 Thesis Statement

Nanotechnology and nanoscience become more and more significant in various research fields. Among different morphologies of the nanomaterials, NPs has gained special interest due to the unique physical and chemical properties. Between the two categories for synthesizing NPs, top down approach and bottom up approach, the bottom up methods such as colloidal or wet-chemical synthesis use insulating organic ligands to control the NP size and shape. However, many applications require solid state structures that exhibit controllable architectures and physical properties. Therefore, these coordinating ligands are detrimental for charge carrier conduction as well as thermal stability of the products. Therefore, development of a new assembly strategy that offer direct linkage of NP that eliminating the intervening ligand interface is essential. Sol-gel method offers a promising approach for directly self-assembly of NPs into self-supported porous superstructures that with no use of intervening ligands. It has been shown in the synthesis of semiconductor aerogel, the oxidizing agents help to remove the surface ligand

and create highly reactive active sites to connect the NPs directly leads to sol-gel transformation. In addition, considering the unique properties and multiple applications of the noble metal NPs, assembling them into low density, highly porous nanostructure is of great interest. However, it is still a great challenge to apply a similar sol-gel approach for producing noble metal aerogels starting with colloidal NPs.

In order to address these questions, our first goal is to develop a novel strategy for the oxidation induced self-assembly of Ag nanostructures into high surface area, uniquely porous, highly conducting aerogels. Among noble metals, Ag is not only exhibiting tunable plasmonic and catalytic properties, but also the most cost effective. Therefore, we have used Ag hollow NPs as the starting material for metallic gel synthesis. Herein, we investigated the oxidation induced self-assembly of glutathione coated Ag hollow NPs into Ag aerogels that exhibits high surface areas and interconnected meso-to-macropore networks that can be tuned by varying the inner cavity of the hollow NPs. The resultant aerogels, which exhibiting accessibility of chemical species to both inner and outer surface of the hollow NPs, provide new perspectives for porosity control of the aerogels. Moreover, by tuning the amount of oxidizing agent used in the sol-gel process, the control over the optical transparency can be attained, producing both opaque and transparent NP superstructures.

Our second goal is to develop a new general methodology for the synthesis of Au/Ag alloy nanostructures through GRR of pre-formed Ag hollow NPs and investigate their sol-gel assembly into porous gel frameworks for SERS applications. Since both Au and Ag are outstanding SERS substrates, alloying Au and Ag together can potential give better enhancement of the Raman signals owing to synergistic effects. In addition, it has been reported that the fractal NP aggregates and highly porous Au and Ag substrates that show rapid diffusion of the analytes

are likely to exhibit greater SERS effects. Therefore, developing Au/Ag alloy aerogels with directly NP cross-linkage, porous structure, rough metallic surfaces, can combine the above advantages and produce promising SERS substrates. Herein, the conversion of Ag hollow NPs into Au/Ag NPs with three distinct morphologies has been investigated through the galvanic replacement reactions. Then, Au/Ag NPs were transformed into Au/Ag alloy aerogels. The resultant metallic aerogels composed entirely of nanosized Au/Ag metal NPs are expected to exhibit high surface areas, low densities and pore size tunability. The SERS activity of Au/Ag alloy aerogels has been studied using Rhodamine 101 (Rd 101) as the probe molecule and signal enhancement is compared with precursor NPs.

Our third goal is to investigate the sol-gel assembly of Ag-Pt-Au ternary NPs into metallic gel frameworks and study their catalytic activity in methanol oxidation. Pt-based material has been widely used in the methanol oxidation catalysis, where in-situ generated CO is produced as a byproduct. Since CO performs like a catalyst poison which strongly bind with the Pt, avoiding the CO is still a great challenge. Since Au NPs can catalyze the oxidation of CO into CO₂, alloying Au and Pt together will help to overcome the CO poisoning problem. Therefore, we have demonstrate the synthesis of Ag-Pt-Au alloy ternary NPs by using Ag hollow NPs as templates. The alloy NPs were self-assembled into highly porous ternary aerogels via oxidative removal of the surface ligands. Additionally, the Au/Pt/Ag ternary aerogels that exhibit direct metal NP linkage, and rough metallic surface, and rapid diffusion of methanol, were also tested as catalyst for the methanol oxidation.

This dissertation consists of chapter 1 as the introduction and chapter 2 describing the characterization methods, chapter 3 discussing the oxidation-induced self-assembly of Ag hollow NPs into transparent and opaque Ag hydrogel and aerogel nanostructures. Chapter 4 discusses

the direct cross-linking of Au/Ag alloy nanoparticles into monolithic aerogels for application in SERS. Chapter 5 describes the sol-gel assembly of Ag-Pt-Au ternary NPs into metallic aerogels for the application on methanol oxidation catalysis. Chapter 6 summarises the major conclusion of the dissertation and suggest potential future direction for metal aerogel.

Chapter 2: Experimental and Characterization Methods

Numerous characterization methods and techniques are required to investigate the structural, chemical, optical and physical properties of the materials. Moreover, wet gels must be dried for physical property investigation and device applications. Supercritical drying offers a promising approach to dry the wet gels into highly porous aerogels while preserving the mesoporous nanostructure. Dried gel materials and precursor NPs are characterized through powder X-ray diffraction to determine the phase purity of materials; UV-Vis spectroscopy to investigate the optical properties of NPs; transmission electron microscopy to elucidate the size, shape and morphology of NPs and aerogels; scanning and transmission scanning electron microscopy/energy dispersive spectroscopy and inductively coupled plasma mass spectrometry for studying the elemental composition and distribution; X-ray photoelectron spectroscopy to investigate the chemical state of the surface atoms; surface area and porosimetry to investigate the porosities. In addition, surface enhanced Raman scattering and cyclic voltammetry were used to test the chemical sensing and electrocatalytic properties of the NPs and aerogels. This chapter describes the above experimental techniques used to synthesize the metal hollow NPs and aerogel, and characterization techniques for elucidation of physical properties of NPs and aerogels.

2.1 Supercritical Drying

For a number of applications, the porous gel framework that exhibit high surface area is desired. Therefore, supercritical drying has been utilized for removing the solvent while preserving gel structure. When the solvent such as acetone or water exist in the hydrogel during the sol-gel transformation process, it forms a heterogeneous environment of which the surface

tension in the liquid phase pulls against any solid structure it contact with. If the solvents is allowed to evaporate via benchtop drying, the mesopores in the hydrogel break apart due to surface tension. In this case, supercritical drying can overcome this problem. Supercritical fluid, with both temperature and pressure above its critical point (Figure 2.1), exhibit no surface tension, since there is no liquid/gas phase boundary. By modifying the pressure and temperature of the supercritical fluid, the properties can be tuned to be more liquid- or more gas-like. Therefore, the supercritical fluid can “evaporate” from the porous wet-gel structure without breaking the superstructure to maintain the porosity. However, due to the high temperature and pressure needed for this method, choosing the right solvent that has lower critical point becomes quite significant. Accordingly, CO₂ and methanol are the most commonly used solvent for supercritical drying. For CO₂ specifically, when the temperature is above 39°C and pressure is above 1300 psi, liquid CO₂ transfers into supercritical phase. By slowly venting CO₂ supercritical fluid, the wet-gel can preserve the porous framework to yield an aerogel superstructure.

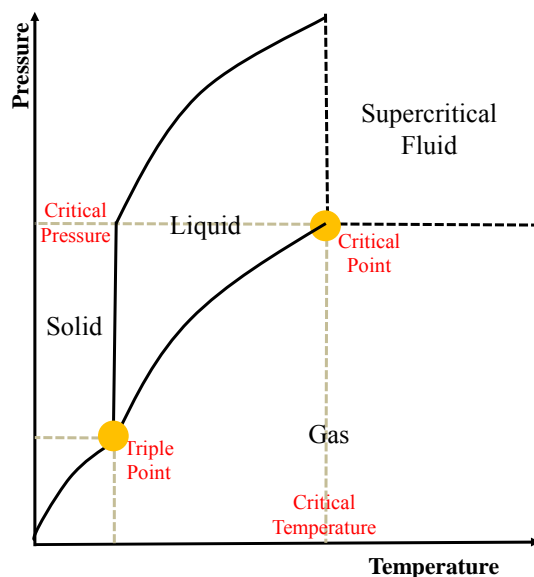


Figure 2.1: Phase diagrams show temperature and pressure effect on material state of CO₂.

In this dissertation, all the hydrogels were first washed with milli-Q filtered water and then with acetone to remove the byproducts of oxidation. Specifically, the layer of water on the top of the hydrogel was removed, and water/acetone was carefully added along the wall of the glass vial without breaking the hydrogel. This process was repeated every 2 hours until the pale yellow color of the supernatant disappears, which is about 6-8 times washing. The acetone exchanged wet-gels were transferred into a microporous capsule by a pipet and then sealed capsules were loaded into the supercritical dryer chamber and filled with liquid CO₂ at 15°C. The wet-gels were exchanged with liquid CO₂ 4-5 times over 12-16 hours to remove acetone from the gel material. Finally, the temperature was raised to 40°C and 1200 psi to achieve a supercritical fluid and kept there for 20 minutes.

2.2 Powder X-ray Diffraction (XRD)

XRD is used to gain a better understanding for the structure and phases of crystalline materials. Every crystalline material has a unique diffraction pattern which is characteristic to its crystal phase, which serve like “fingerprint” structural feature. Due to a similar length of the crystal interatomic distances and X-ray radiation wavelength, electrons inside of the atoms can create scattering effects along with the X-ray oscillating electric field, which gives specific diffractions. For the majority of the materials with unique diffraction patterns they can be characterized and identified through the Powder Diffraction Files (PDF).

In a typical PXRD, the X-ray tube generates X-rays by applying an accelerating voltage and let the electron beam interact with a metal target (Cu). The voltage used is usually between 30K – 50 kV in order to heat the tungsten filament for an ejection of high energy electrons. As the electron beams interact with the target (Cu), the 1s orbital electrons of Cu is removed due to

ionization, leaving a vacant spot to be replaced by electrons from 2p or 3p orbitals. Since the electrons at outer orbitals have high energy than from inner orbitals, such electron transition can emit energy in the X-ray form. There are mainly two types of X-ray used in PXRD, $K\alpha$ (2p-1s) for general use, and $K\beta$ for lower energy X-rays (Figure 2.2)

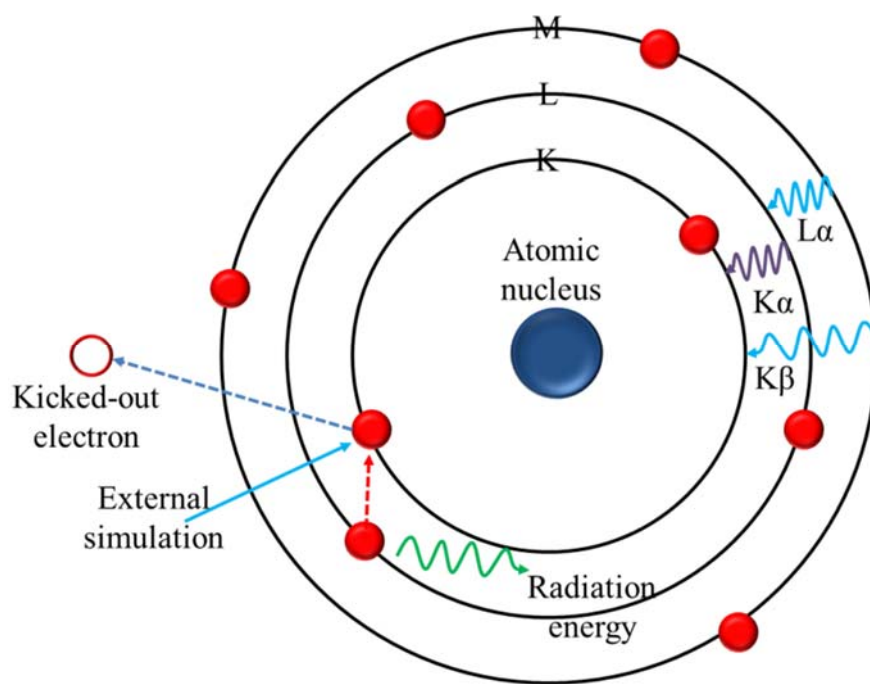


Figure 2.2: Schematic view of an atom excited by an external simulation to yield energy radiation.

When the X-ray strikes the sample as shown in Figure 2.3, it can only be partially scattered by atoms on the surface of the crystal. The rest of the X-ray can pass through the next layer of atoms, and again part of the X-ray got scattered and the other pass through. Such process results the overall diffraction pattern very similar to grating diffract of X-ray. Therefore, the spacing between each layer should be close to the radiation wavelength, so that the beams diffracted by two different layers in a phase can have both constructive interference and destructive interference. Assume two incident beam X and Y are irradiating the material and diffracted by two constructive crystal planes resulting X' and Y'. Therefore, in order to build a

constructive interference, the length of XZ plus ZY have to be an integral of the X-ray wavelength. Otherwise, Herein, diffraction peaks only shows when

$$\sin \theta = \frac{n\lambda}{2d} \quad \text{Equation 2.1}$$

with θ : angle of incident X-ray; n : integer; λ : X-ray wavelength; d : spacing between two atom layers.^{136, 137} In this case, because highly regular structure is required, so only crystal structures can diffract, and amorphous samples can't exhibit diffraction patterns.

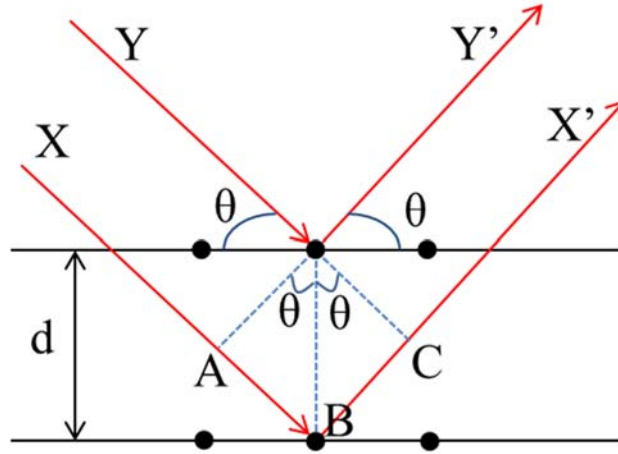


Figure 2.3: Reflection of X-rays from two planes of atoms in a crystal.

Moreover, PXRD patterns for nanoscale shows unique broadness due to the crystalline size. That is because nanomaterial has less number of lattice planes where not all the every interfering waves can be cancelled. Therefore, the peak broadness represents the crystal and it can be used to determine the particle size using the Scherrer equation (Equation 2.2) as follows:

$$t = \frac{0.9\lambda}{\sqrt{B_M^2 - B_S^2} \cos \theta} \quad \text{Equation 2.2}$$

with λ : X-ray wavelength; B_M : observed peak width; B_S : peak width of standard crystal; θ : diffraction angle. This theory will be applied in this dissertation for determining the noble metal NP sizes.

For the experiment, a Philips X'Pert X-ray diffractometer equipped with a Cu K α ($\lambda = 1.5418 \text{ \AA}$) radiation was used to record powder X-ray diffraction patterns (Figure 2.4). The incident X-ray beam angle θ first started by 15° and slowly increased to 45° . On the other side, the X-ray detector records the diffracted X-ray beam with an angle of 2θ to process and generate the whole pattern. All the XRD data in the dissertation are generated by this way. The diffraction patterns are matched with PDF database from International Centre for Diffraction Data for crystal phase identification. Scherrer equation was used for crystal size estimation.

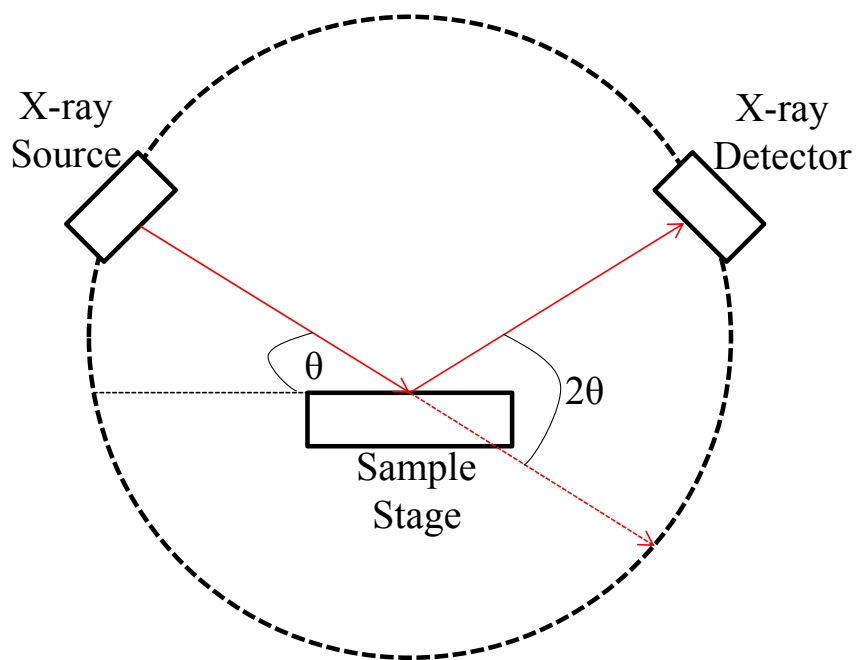


Figure 2.4: Schematic illustration of X-ray diffraction instrument.

2.3 UV-Vis Spectroscopy

UV-Vis spectroscopy refers to absorption/reflectance spectroscopy in ultraviolet-visible spectral region (200 – 800 nm). For the solution absorption spectroscopy, materials are usually dissolved in the solvent to form an optically transparent solution. When the UV-Vis light interact with a material, the incident photons excite electrons from the ground state (non-bonding electrons or π -bonding electrons) to the lowest electronic excited state. Therefore, only certain wavelength of the light can be absorbed, and that depends on the energy gap between the highest energy occupied molecular orbital (HOMO) and lowest energy unoccupied molecular orbital (LUMO) (Figure 2.5).

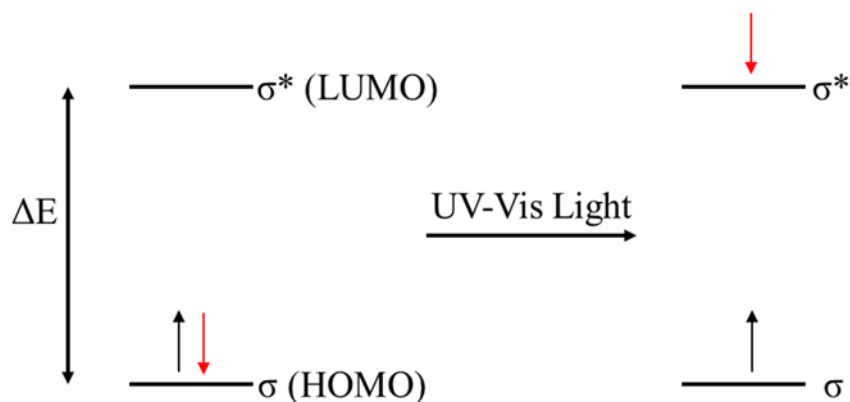


Figure 2.5: Schematic view of electron excited by UV-Vis light.

The percentage of incident photons absorbed at each wavelength can be measured by scanning a certain range of the light and recording the absorbance. Specifically, with incident UV-Vis light pass through the molecules or nanomaterial in the solution, certain wavelength of the light can be adsorbed and other transmitted through. The absorbed intensity of light is directly proportional to the concentration of the materials, and it can be calculated with Beer-Lambert law (Equation 2.3).

$$A = \log_{10} \frac{I_0}{I} = \epsilon c L \quad \text{Equation 2.3}$$

where A is the absorbance, I_0 is the intensity of incident light, I is the transmitted intensity, ϵ is the molar absorptivity, c is concentration of the solution, and L is the length of the sample. According to the equation, concentration of the solution can be calculated when A got measured through instrument.

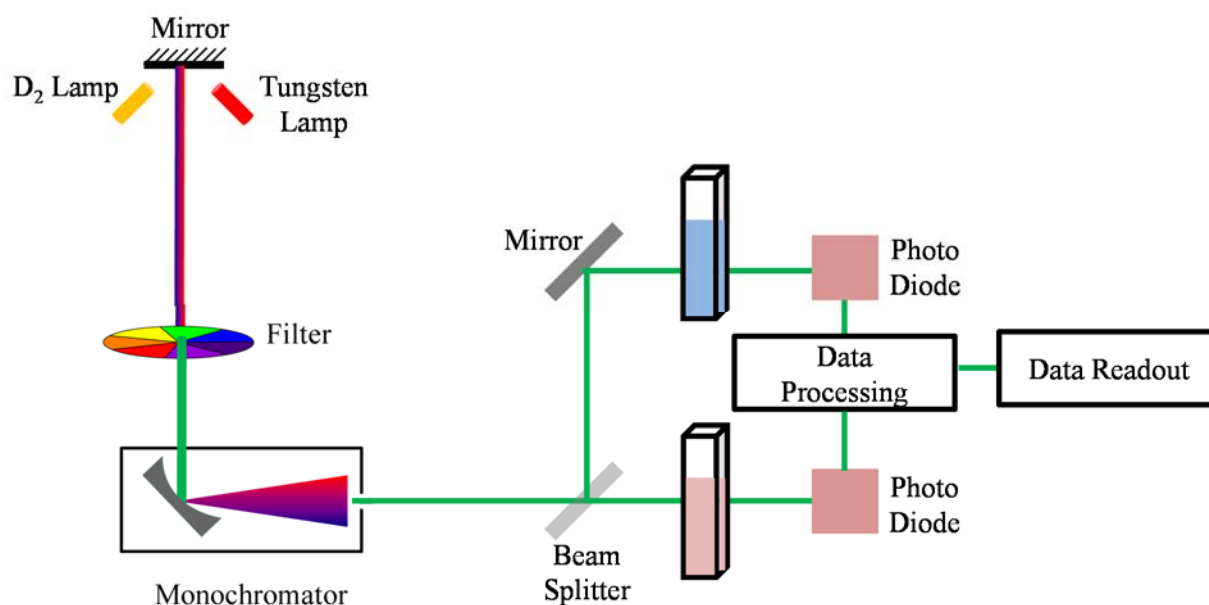


Figure 2.6: Schematic view of UV-Vis spectrophotometer.

More importantly, besides the quantitative analysis, the spectrophotometer detects different SPR of metal NPs based on their size, morphology and dimensionalities. Such localized SPR is due to the collective oscillation when the incident photons interact with the conduction band of the metal NPs. Therefore, in this work, A Cary 6000i UV-Vis-near infrared (NIR) spectrophotometer (Agilent Technologies) was used for optical absorption measurements. Double beam was applied in the characterization with one blank and the other one for sample (Figure 2.6). The light sources, a combination of deuterium lamp and tungsten lamp, give the

entire visible spectrum region that covers 200 nm to 800 nm. When the light passes the filter, which can be considered similar to a prism, the light is diffracted and only a quite narrow range of the wavelengths can pass through the filter to the monochromator at a time. After the passed light hits the beam splitter, only part of the light goes straight and pass through the cell that has the reference solution. The other part of the light is reflected by a mirror and pass through the cell with the sample solution. Both signal intensity can be observed by the photo diode and detected with the data processor to finalize the data.

2.4 Transmission Electron Microscopy (TEM)

TEM is a commonly used technique for observing material's shape and morphology in nanoscale. As shown in Figure 2.7, the electron gun at the top generates an electron beam in high vacuum.¹³⁸ Afterwards, there is a high accelerating voltage to speed the electrons in order to make sure that the electrons propagate as waves with short wavelengths that can penetrate into a sample. The beam is focused into a coherent and thin beam by passing through several condenser lenses until it strikes the TEM grid with sample. When the electron beam passes through the sample, there are interactions between the electrons and molecules in the sample. The amount of unscattered electrons which pass through is determined by the thickness and scattering potential of the sample. Such unscattered electrons can be detected by the imaging system (an image lens and a fluorescent screen couple with a digital camera) and the contrast image of the sample will be obtained. There are three different contrast applied in the TEM, including thickness contrast, diffraction contrast and phase contrast. For thickness contrast, the lighter areas in the image stands for more sample which has more electron transmitted through), and darker areas means less sample so that fewer electrons transmitted through.¹³⁹ The resolution can range from 0.5 Å to 2.5 mm, and for high resolution TEM it goes even as high as 50 million times magnifications.

Moreover, the scattered electrons can also provide the diffraction patterns, which can determine the crystal structures and calculate the lattice fringes. In this case, TEM offers a promising way for imaging at higher resolution of noble metal NPs morphology as well as the porous aerogel superstructure.¹⁴⁰

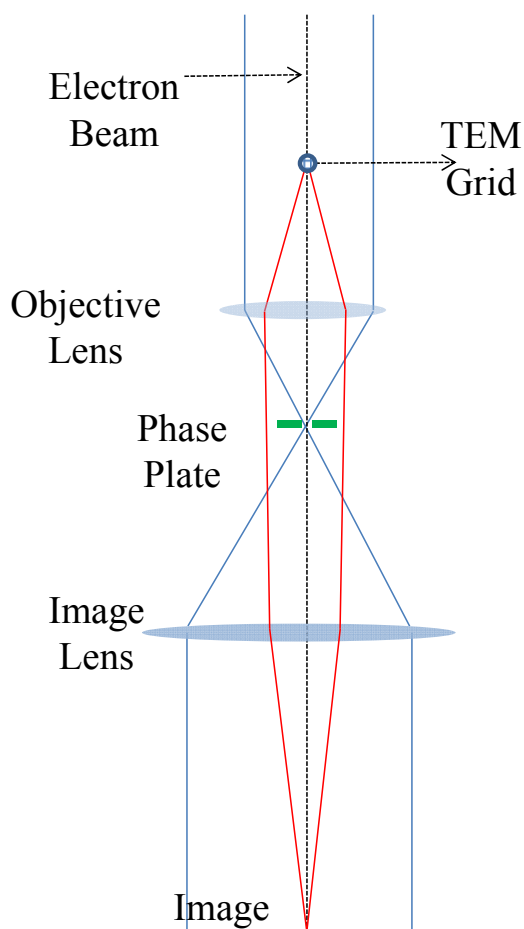


Figure 2.7: Schematic view of the inside of TEM.

Scanning transmission electron microscope (STEM) is a powerful characterization technique for imaging nanoscale materials as well as providing elemental mapping by an EDS detector. STEM shares with the same principle as the normal TEM mentioned above, which is using a focused beam of electrons to scan the sample on the TEM grid and signals are collected by the detector. However, similar to SEM, the backscattered electrons and secondary electrons

can be used for imaging in STEM with a better spatial resolution of the detector. In this case, annular dark field detector, which can exclude the transmitted beam and reveal compositional changes in the sample to obtain the elemental mapping. The total intensity observed by the detector can be recorded to show as a function of the position of illuminating probe. Since signal only presents with the atoms and vacuum has no signal at all, that leads to a brighter contrast with heavier atoms (higher intensity of scattering) in the image. Therefore, the mapping of the different mapping can also be observed.

In this dissertation, JEOL JEM-1230 TEM equipped with a Gatan ultrascan 4000 camera operating at an accelerating voltage of 120 kV. The NP samples were prepared by depositing a drop of solution onto the carbon-coated copper grid, followed by ambient evaporation of the solvent. The aerogel samples were prepared on copper grids by dispersing fine powders in acetone/ethanol via sonication and depositing a drop of suspension onto the copper grid, followed by evaporation of the solvent. The average NP sizes and hollow NPs wall thicknesses were obtained through 120-150 NPs per each sample and from 3-5 individually prepared samples. All STEM images and elemental maps were acquired in a Titan 8000-300 electron microscope equipped with a Fischione High-Angle Annular Dark Field detector (North Carolina State University) operating at 200 kV. The sample preparation is similar to TEM grids but just switch to ultrathin grids since more electrons can transmitted for a better quality image.

2.5 Scanning Electron Microscopy (SEM)/ Energy Dispersive Spectroscopy (EDS)

The SEM is widely used electron microscopy technique for microscale imaging. It uses a focused beam with high energy electrons to strike the surface of solid samples in order to generate a variety of signals that derive interactions between them. Among these signals, such interactions can result into three types of most pronounced signals: secondary electrons,

backscattered electrons, and X-rays. These three signals can be revealed to give the information for samples' surface topography, orientation of materials, crystalline structure, and elemental compositions. In order to generate the SEM image, the incident electron beam scans in a raster pattern across the surface of the sample and the emitted electrons can be detected for each position in certain area. The intensity of the signal displays the contrast of the brightness to produce the final image representing the morphology of the sample in the chosen area. Generally, SEM generates 2D images with scales from centimeters to microns, which helps to observe the overall network connections of porous materials.¹³⁹

EDS is a powerful and useful technique for elemental analysis and chemical characterization. It is usually integrated into either an SEM or STEM instrument, with an EDS X-ray detector mounted into the sample chamber. General used EDS detectors include Si and Li crystals so that they can detect the scattered electrons at low voltages with high sensitivity. In SEM, an electron beam is scanned across the analyte surface with producing a various signals. If the electron beam creates a vacancy in an inner shell (K shell) of the material molecule orbital, an electron is transferred from outer orbital (L shell or M shell) to fulfill that spot (Figure 2.2). Since electrons from outer orbital has high energies, the electron gives an emission of an X-ray beam corresponding to the element when it transferred into the inner shell. The X-ray emitted from the sample during bombardment by electron beams can be absorbed by the detector, and the intensity of backscattered electron correlates with the characteristic X-rays of the element. Therefore, EDS can be observed for qualitative elemental distribution of different compositions.

In the experiments, NPs and aerogels powder samples were placed on a carbon tape attached to an Al substrate. High resolution SEM images were acquired using Hitachi SU-70 SEM operating at 20 kV. The elemental compositions/maps of the samples were obtained from

an *in-situ* EDS in Hitachi SU-70. The atomic composition were calculated through EDAX Genesis software (Oxford Instrument).

2.6 X-ray Photoelectron Spectroscopy (XPS)

XPS, also known as electron spectroscopy for chemical analysis, is a technique that measures the elemental composition, chemical and electronic state of the elements on the surface of a material. The sample is first irradiated with a low energy X-rays, which can excite the surface atoms. If the binding energy is lower than the energy of X-ray, the electrons will emit from the atom, which is called as a photoelectron. However, only the photoelectrons at the outer surface escape from the surface, the energy of the photoelectrons can be measured through the detector (Figure 2.8).

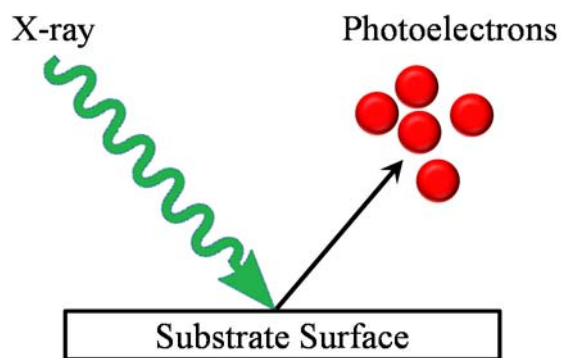


Figure 2.8: Schematic view excitation of photoelectrons.

Specifically, when a molecule or atom absorbs an X-ray photon, the electron can be excited and ejected. The kinetic energy of the ejected electron depends on the binding energy of the electron and photon energy (Figure 2.9). Since the total of binding energy and kinetic energy equals to the energy of the X-ray (Equation 2.4):

$$E_{kinetic} = h\nu - E_{binding} \quad \text{Equation 2.4}$$

with h for the Planck's constant and ν for the frequency of the X-ray. By measuring the kinetic energy, the binding energy of the electron by subtraction of the kinetic energy out of the energy of incident X-ray. Interestingly, even the same type of atom doesn't necessarily have the same binding energy due to the difference in the surrounding environment, including ligand electronegativity, oxidation states, and coordination effects. Therefore, XPS becomes a significant characterization technique for studying surface properties. Specially for thiolate capped noble metal NPs, it is a promising method to investigate chemical state change of surface atoms during the sol-gel transformation.¹⁴¹

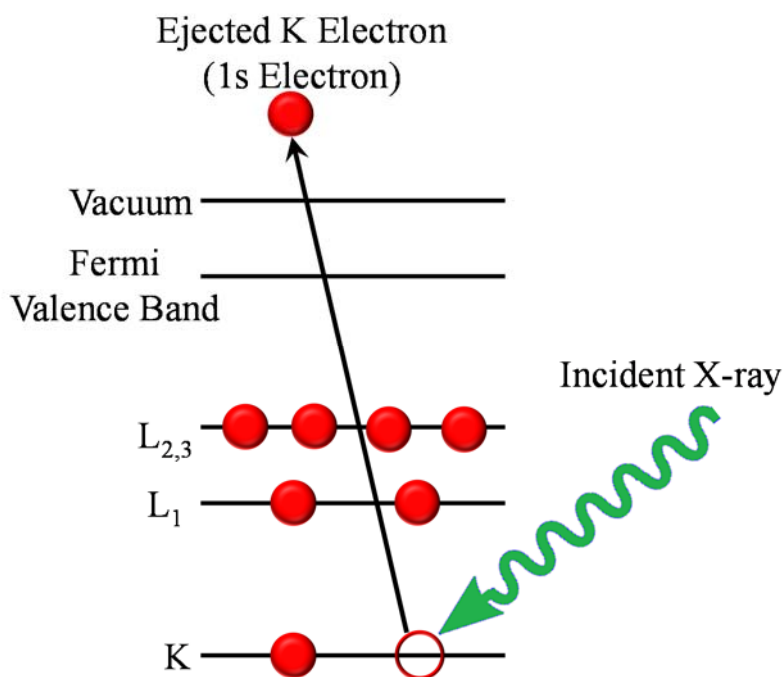


Figure 2.9: The photoemission process of an excited electron escape from the orbitals as a photoelectron.

In the dissertation, XPS data was recorded using a ThermoFisher ESCALAB 250 instrument equipped with a monochromated Al K α X-ray source. The aerogel and NP samples were pressed to be loaded onto indium foil which deposited onto a conductive carbon tape, in

order to account for the surface charging effect of the instrument. All the data were collected with peaks corresponding to different compound oxidation states, and the peak positions were calibrated through adventitious carbon (1s) at 284.6 eV.

2.7 Inductively Coupled Plasma Mass Spectrometry (ICP-MS)

ICP-MS is one of the most powerful and sensitive techniques for detecting elemental composition and isotope analysis. The great advantage of ICP-MS, compared to other analysis such as EDS, is the suitability for detecting significant low concentration of multiple elements with high sensitivity and accuracy. The ICP-MS detection limits usually are in the range part-per-billion to parts-per trillion depends on the elements. Generally, the samples were vaporized, atomized and then ionized by inductively coupled plasma with a high ionization potential energy (Argon, 15.76 eV).¹⁴² Specific ICP torch, which is made of fused quartz, creates and shapes the plasma. The sample materials are extracted through several cones to form a narrow beam and then accelerated to pass through the entrance slit to the mass analyzer. Then the ions will be separated based on their mass/charge ratio and received by the detector. The concentration of the ions can be quantified through the electronic signal converted from the ion signal. Usually a series of standards with different concentration are prepared first to observe their signal intensities. Since the concentration correlates with the number of ions detected, there is a linear correlation between the two. According to that, if the samples' concentration falls into the standard solutions' range, the concentration of unknown sample can be calculated through the intensity.

In this dissertation, ICP-MS analyses were performed with a Varian 820 MS instrument. 1 mg of each hollow NPs and aerogels was digested in freshly prepared aqua regia, and then further diluted into 10 mL in a volumetric flask with ultrapure water, and then again diluted 1000

times to meet the range of ICP-MS level. The standards were diluted into ppb level with 5 different values to plot the correlation line for quantifying the concentration of the elements.

2.8 Surface Area and Porosimetry Analysis

Since gases and vapors can be absorb by cool solids' surface and then condensed into liquid phase to fill into the pores of a porous structure, the gases and vapor absorption can be applied for measuring the pore surface information such as surface area, pore width and volume, by evacuating the absorbed materials. Such kind of absorption can due to either chemisorption (forming chemical bonds) or physisorption (Van Der Waals forces) between gas molecules and porous materials surface. Therefore, in order to determine the surface area and porosimetry of porous materials, adsorption/desorption isotherms are quite often used.¹⁴³ Specifically, N₂ adsorption/desorption analysis at 77K is applied in this dissertation. The samples were firstly loaded into sample tube and heated at 50 °C under vacuum for 24 hours to remove the contaminants. Afterwards, the sample tubes were cooled in the liquid nitrogen. With a controlled volume of nitrogen injected into the tube, the pressure can slowly reach equilibrium. The amount of nitrogen absorbed at each pressure can be plotted as a curve (Figure 2.10). The x axis represents the relative pressure verses the saturation pressure P_0 , whereas the y axis stands for the amount absorbed.

In mesoporous materials, the adsorption/desorption behavior depends both on the material surface with liquid (usually liquid N₂) interaction strength and attractive interactions between the liquid molecules, which causes not only the multilayer absorption but also capillary condensation inside of the mesopores (2-50 nm) to macropores (> 50 nm). Starting with low value of P/P_0 (0.03 – 0.4), the N₂ molecule attached onto the surface to form a monolayer, which fills the micropores (< 2 nm). The isotherm tends to exhibit a linear plot which means the N₂

absorption increases with the pressure. As the P/P_0 increases (0.5 – 0.8) and the formation of monolayer almost finished, multilayer absorption started on top of the monolayer, which fills the majority of mesopores (2-50 nm). The isotherm is a curve at this range since more layers formed with the increase of pressure. Afterwards, due to the further increase of P/P_0 (above 0.8), the gases were condensed to liquid and fill the macropores (> 50 nm) of the material, which caused a hysteresis loop in the isotherm. (Figure 2.10) Therefore, the adsorption/desorption isotherms helps with determination of surface area, pore volume, pore size distribution and other properties.¹⁴⁴ According to IUPAC classification, there are six types of isotherms (type I-VI) classified by shape (Figure 2.11), and they can be used to identify different type of materials. Type I, represents that material has extremely small micropores. Type II and IV indicate that the material either has no pores or relatively large pores. Type III and Type V are due to the greater affinity of the adsorbate molecules on the solid surface. Type VI only shows for the nonporous solid that has smooth surface. Type IV and V's hysteresis loops are due to the differences in the rate of pores filling and emptying. The hysteresis loops of the isotherms can be categorized to 4 types (type H1-H4) indicating different shapes of the pores present in the materials: cylindrical or tubular shaped (H1), bottle-shaped (H2), parallel plates (H3) and slit-shaped (H4). (Figure 2.12)

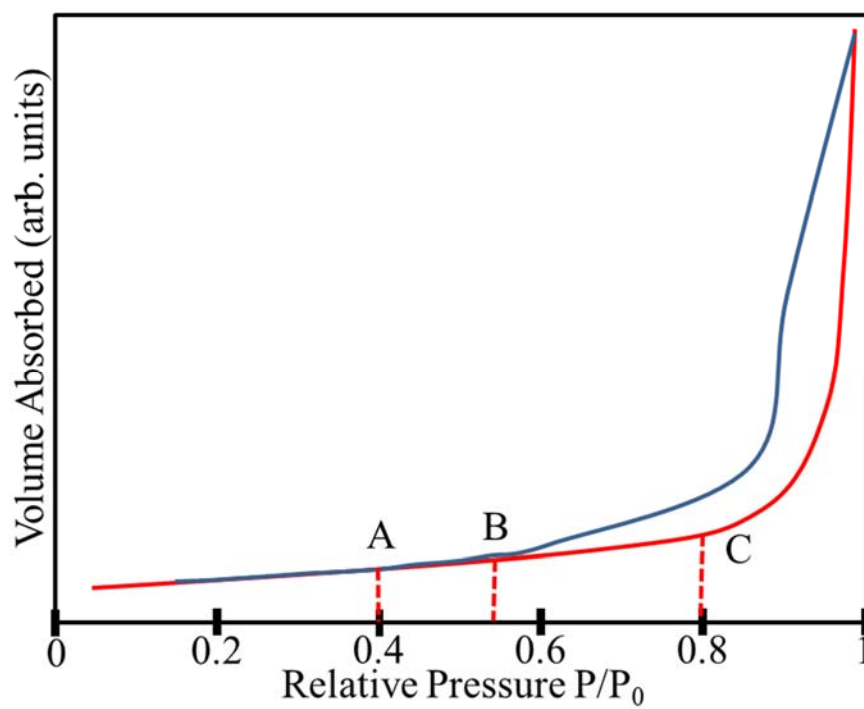


Figure 2.10: A representative N₂ adsorption (red) / desorption (blue) isotherm.

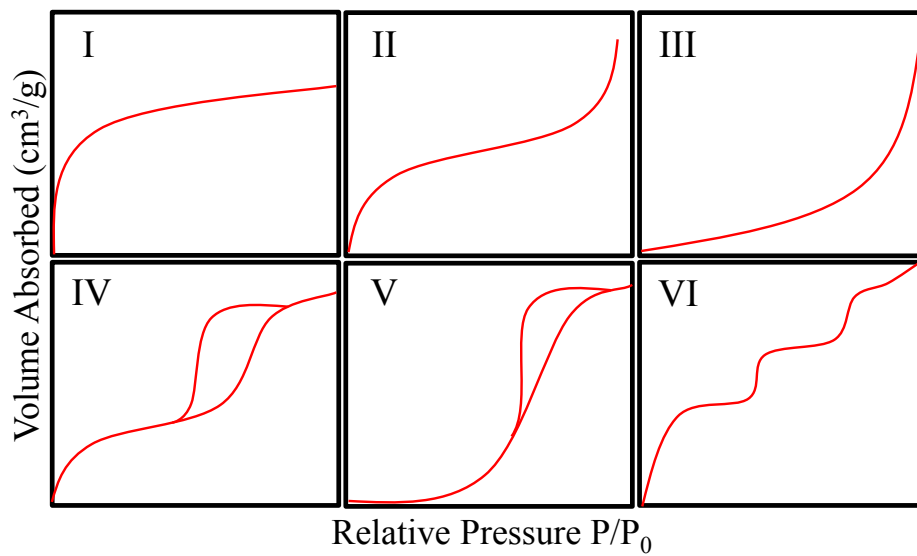


Figure 2.11: Six types of basic adsorption/desorption isotherms.

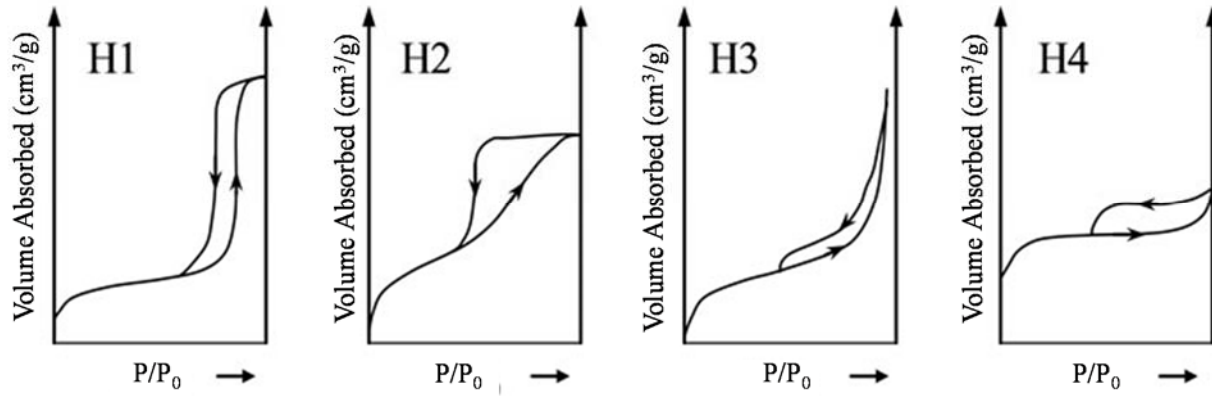


Figure 2.12: Categories of gas adsorption/desorption hysteresis loops.

In order to calculate the surface area and pore size distribution, the isotherm data were fit using the Brunauer-Emmett-Teller (BET) model to calculate the surface areas whereas the Barrett-Joyner-Halenda (BJH) model was used to determine the average pore diameters and cumulative pore volumes. BET model applied for the linear plot part (0.03-0.4) with the following equation:

$$\frac{1}{V_a \left[\left(\frac{P_0}{P} \right) - 1 \right]} = \frac{1}{V_m C} + \frac{(C - 1)P}{(V_m C)P_0} \quad \text{Equation 2.5}$$

with V_a for the volume of N_2 absorbed at given P/P_0 ; V_m for the volume of N_2 to cover the surface; C is heat absorption constant. By multiplying V_m with Avogadro's number, the number of N_2 atoms that forms the monolayers can be calculated. Since the radius of the N_2 is known (0.16 nm^2), the total area can be obtained by multiplying with N_2 atom number. As the weight of the samples was measured, so that the materials surface area is easy to get.

The BJH model is based on Kelvin equation (Equation 2.6), which quantifies the proportionality between the pore size and equilibrium gas pressure.

$$RT \ln \frac{P}{P_0} = - \frac{2\gamma V_m}{r} \quad \text{Equation 2.6}$$

where R is the gas constant; T is the absolute temperature; P is the relative pressure; P₀ is the saturation pressure; γ is the surface tension; V_m is the molar volume of the liquid and r is the mean radius of curvature of the liquid. For the N₂ desorption, the pore volume can be measured through the desorbed gas amount. The BJH model can be used to calculate the number of multiple layers using pore radius and layer thickness, so that it allows for the calculation of pore sizes from the isotherms. Therefore, the BJH model can determine the cumulative pore volume and pore diameter.

In this dissertation, The N₂ adsorption/desorption isotherms were acquired using a Micromeritics ASAP 2020 surface area and porosimetry analyzer at 77 K. All samples were degassed under vacuum at 50°C for 24 h prior to the analysis. The isotherm data were fit using the BET model to calculate the surface area values. The average pore diameters and cumulative pore volumes were obtained by applying the BJH model to desorption branches of the respective isotherms. Five independently prepared samples were analyzed for each system.

2.9 Surface Enhanced Raman Scattering

Background and principle has been thoroughly discussed in chapter 1.10.

Figure 2.13 shows the basic principle of the SERS instrument. The laser beam at certain wavelength is generated through the laser source (usually 532 nm or 785 nm). Then the beam interact with samples deposited on the substrate, noble metal aerogels or NPs. Since the beam can be scattered elastically (Rayleigh scattering) and also inelastically (Raman scattering), both

of the scattered laser beams are received by the detectors. The energy difference between the incident laser beam and Raman scattered laser equals to the change of the nuclear motions, including molecular vibrations, scissoring and stretches. The software analyzes the difference between the energy of the laser and scattered laser beam, and then the spectrum of Raman shift verses signal intensity can be obtained (Figure 2.13).¹⁴⁵

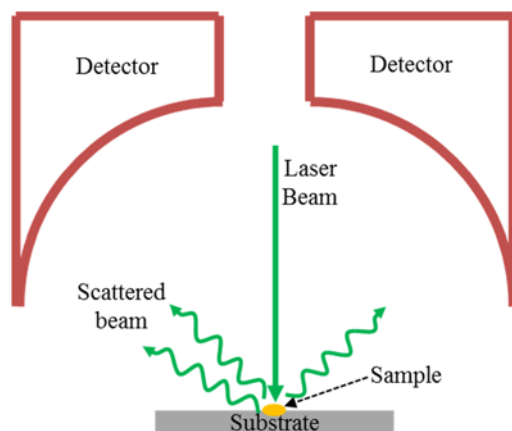


Figure 2.13: Schematic view of a sample on SERS substrate scattered incident laser beam.

SERS measurements were performed on a Horiba LABram HR Evolution Confocal Raman Spectrometer equipped with a 532 nm laser. The Rd 101 solutions (1 μM - 1 nM) were prepared in ethanol and the aerogels were immersed in each solution for 24 h with intermittent shaking. The dye solutions were decanted off then the aerogels were placed on an aluminum substrate (pan) and allowed to dry prior to spectra acquisition. The NP samples were prepared in two different ways, first the Rd 101 solutions were premixed with the Au/Ag NP sols (10 mM) for 24 h and a drop (20 μL) of this mixture was placed on an Al substrate and allowed to evaporate under ambient conditions. Second, a drop (20 μL) of the concentrated (10 mM) NP sol (without Rd 101) was placed on an Al substrate and the solvent was allowed to evaporate, producing a dried NP precipitate. Then, the Rd 101 solutions were drop casted onto as-prepared

NP precipitates. For all measurements, SERS spectra were acquired with a fixed laser power of 3 mW, 10X objective, spot size of 50 μm , receiving slit width of 500 μm , and an acquisition time of 10 s.

2.11 Cyclic Voltammetry (CV)

CV is a versatile potentiodynamic electrochemical measurement technique which can be used to study the redox behavior of materials. It offers a promising yet fast approach to evaluate the location of the redox potentials of electroactive species. It develops an electrochemical cell under conditions which voltage is in excess than the predicated value through Nernst equation (Equation 2.7). The systems includes three electrode cell submerged in an electrolyte solution, and connect to the CV instrument for measurement. Counter, reference and working electrodes are setup closely in a closed cell under an inert atmosphere to avoid the effect of oxygen. The electrolyte solution is prepared through dissolving an ionic material, such as strong acid (HNO_3 , HNO_3), base (NaOH , KOH), or salt (NaCl , KCl) in to polar solvent (water, ethanol, methanol etc.). The analyte, or electroactive species dissolves in the electrolyte solution to make the cell. After the connection to make a circuit, different potentials are applied at a specified scan rate mV/s, in order to measure the change of the current. The potential keep cycles between two predetermined voltages until reaching steady state.

$$\log K_{eq} = \frac{nE^0}{0.0592V} \quad \text{Euqation 2.7}$$

Therefore, the CV requires the measurement of current at the working electrode during cyclic potential scans (Figure 2.14). The arrow shows the direction of the initial scan. With increasing the initial potential, the anodic current increase, resulting an oxidation of the material. The I_p^{ox} is reached when all of the materials at the surface of the electrode got oxidized, and

corresponding potential is E_p^{ox} . When the potential goes to E_{max} , which is also called as switching potential, the potential scans move negatively resulting the cathodic current and reduction happens. The peak current is called as cathodic current I_p^{red} , and corresponding potential is E_p^{red} . Similar to the other peak, all the material on the working electrode got reduced.

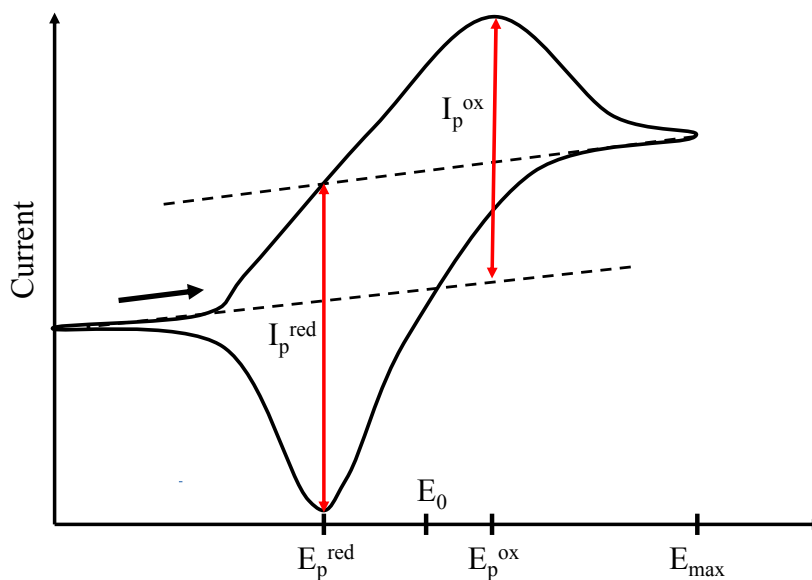


Figure 2.14: Schematic illustration of a reversible scan of CV.

The working electrodes for the electro-oxidation of methanol were fabricated by depositing a thin film of nafion-impregnated ternary alloy aerogel catalyst ink on glassy carbon electrodes (GCE, 5 mm in diameter, or 0.196 cm² in area). A mixture of 4.0 mg of the ternary alloy aerogel, 370 L isopropanol, and 30 L nafion (Aldrich, 5 wt%) was sonicated for 60 seconds to produce ternary alloy aerogel inks with a concentration of 10 g/ μ L. Electrodes with a catalyst loading of 0.6 mg were prepared by allowing the isopropyl alcohol in the deposited inks to evaporate at room temperature. The electrodes were further dried at 50 °C for 12 h and stored in a desiccator.

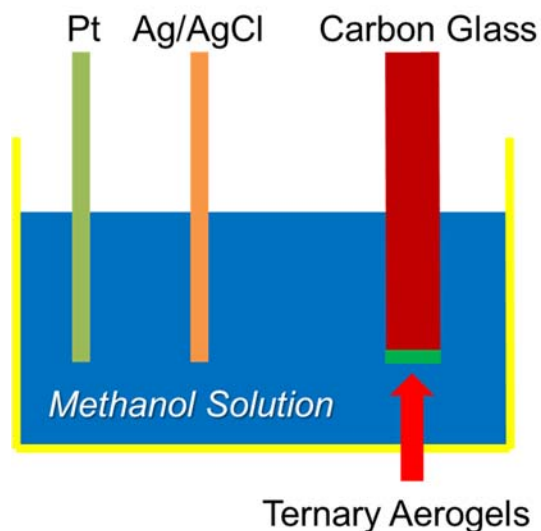


Figure 2.15: Schematic view of three electrode system of the CV for methanol oxidation catalysis experiment.

The electrochemical performance of the as-prepared ternary alloy aerogels as active electrode materials toward the electro-oxidation of methanol has been investigated by means of cyclic voltammetry (CV), chronoamperometry and electrochemical impedance spectroscopy (EIS) on CHI-401 electrochemical workstation (CH Instruments Inc.). The aqueous electrolyte solution (KOH, 1 M) was prepared with ultrapure water. Prior to any electrochemical measurement, all test solutions were deaerated using a high purity nitrogen for 1 h. All the electrochemical measurements were conducted in 1 M KOH aqueous solution containing methanol in a conventional three-electrode test cell at room temperature and under nitrogen as a protection atmosphere. Ternary alloy aerogel modified GCE, and Pt wire (CH Instruments Inc.) were used as working electrode, and counter electrode, respectively. Potentials of the working electrode were recorded against Ag/AgCl (CH Instruments Inc.) reference electrode. Activation of the ternary alloy aerogel modified GCE has been done by cycling it in 1 M KOH aqueous electrolyte in the voltage range -1.0 to 0.15 V (vs. Ag/AgCl) for 10 cycles at scan rate of 50 mV s⁻¹. Effect

of the scan rate on the electro-oxidation of methanol in 1 M KOH aqueous solution containing 2 M methanol was studied. Stability and tolerance of the as-prepared ternary alloy aerogel catalysts were evaluated by chronoamperometry in 1 M KOH aqueous solution containing 2 M methanol. The conductivity of the ternary alloy aerogel electrodes was determined in 1 M KOH aqueous solution by EIS in a frequency range of 0.01 Hz to 0.5 GHz with 5 mV AC amplitude.

Chapter 3: Oxidation-Induced Self-Assembly of Ag Nanoshells into Transparent and Opaque Ag Hydrogels and Aerogels

3.1 Introduction

The advent of nanotechnology has sparked many research forefronts in the creation of nanoscale materials with control over size, shape, composition, and surface properties.^{1,2,146} However, the development of revolutionary technologies is predicated on our ability to build, orient, and assemble nanosized solids into functional architectures with useful and controllable physical properties. Therefore, the use of oxidation induced self-assembly to produce low-density, high-surface-area, conducting aerogels from colloidal NPs has gained significant interest in recent years. Accordingly, synthesis of semiconductor aerogel from metal chalcogenides and pnictide NPs has been reported.^{43,67-69} However, application of this strategy for assembly of metal NPs has not been thoroughly investigated. Recently, Eychmüller's group established monometallic (Au, Ag, and Pt) and heterogeneous bimetallic (Ag-Pt and Ag-Au) solid NP-based aerogels via H₂O₂ oxidation of NP solloids.²⁷⁻²⁹ Moreover, our group reported the synthesis of Au/Ag, Pt/Ag, and Pd/Ag alloy aerogels via salt-mediated cross-linking of negatively charged precursor NPs.²² However, the use of cyclodextrin or other ligands for bridging is detrimental for electrical transport, interparticle coupling, and limit thermal stability of assemblies. Therefore, developing the self-assembly of highly porous self-supported gel framework that has direct noble metal NP linkage without intervening ligands has received significant interest. Therefore, in this chapter we reports the synthesis of Ag nanoshells (NSs) displaying size and shell thickness tunable plasmonics without the use of dielectric cores. Moreover, for the first time we demonstrated the extension of oxidation-induced NP condensation strategy for the assembly of Ag NSs into transparent and opaque Ag gel frameworks. The opaque hydrogel and aerogel

composed entirely of hollow NSs, exhibit enormously high surface areas and extremely low densities. More importantly, the mesoporosity of the aerogel can be tuned with different precursor NPs used. The network structure, morphology, surface area, and porosity of the NSs and aerogels are evaluated, characterized, and discussed in this chapter.

3.2 Experimental Section

Materials. Silver nitrate (99.9%) and sodium borohydride (98%) were purchased from Strem Chemicals. Tetranitromethane and L-glutathione reduced (98%) were purchased from Sigma-Aldrich. Sodium hydroxide (ACS grade) and acetone (ACS grade) were purchased from Fisher. The water used in all syntheses was 18 M Ω milli-Q filtered. All chemicals were used as received without further purification.

Synthesis of Ag NSs. Ag NSs with varying size and shell thickness were prepared by following a literature method¹⁰⁴ with further modification for the purpose of large scale production (Table 3.1). In a typical synthesis, 50 mL of water was added to a 250 mL reaction flask in ice water bath and appropriate volumes of 10 mM AgNO₃ and glutathione were added (Table 3.1). After mixing for 5 minutes, the pH of the reaction mixture was adjusted to 12 using 0.1 M NaOH, which caused an immediate color change from colorless to pale yellow indicating the formation of Ag₂O NPs. Finally, an excess of NaBH₄ (Table 3.1) was swiftly injected and the solution has turned to orange-brown, pink, or purple indicating the formation of hollow Ag NSs with varying size and shell thickness. These reactions were performed multiple times to prepare 375 μ mol of Ag NS solution (~800- 2400 mL) for the subsequent gelation studies.

Table 3.1 The volumes of 0.1 M AgNO₃, 10 mM glutathione, 0.1 M NaOH, and 10 mM NaBH₄ used in the synthesis of Ag NSs.

Sample	Plasmon band maxima (nm)	10 mM AgNO ₃ (mL)	10 mM Glutathione (mL)	0.1 M NaOH (mL)	10 mM NaBH ₄ (mL)
1	470	3.00	0.27	10.00	3.60
2	480	3.00	0.30	10.00	3.60
3	490	3.00	0.35	10.00	3.60
4	500	1.20	0.10	10.00	3.60
5	510	1.10	0.10	10.00	3.60
6	520	1.00	0.10	10.00	3.60
7	550	1.00	0.13	10.00	3.60
8	570	1.00	0.15	10.00	3.60

Preparation of Concentrated Colloidal Sols. For the preparation of concentrated Ag sols, two techniques were employed; centrifuge filtration (CF) and rotatory evaporation (RE). With CF technique, Sartorius Vivaspın centrifuge filters (MWCO 30,000) were employed. In a typical synthesis, the centrifuge filters were filled with 20 mL of the as-prepared Ag sol, followed by centrifugation at 3000 g for 6-7 minutes to remove 15 mL of water and the majority of ionic byproducts (Na⁺, NO₃⁻, OH⁻, unreacted thiolates). When the total volume was reduced from 800-2400 mL to 50 mL, an aliquot of ultrapure water (200 mL) was added to wash off the remaining byproducts. After washing twice, the final volume was further reduced to 10 mL and 0.0375 M Ag NS sol was produced (based on the moles of AgNO₃ used in the synthesis and assuming 100% reduction). In the case of RE technique, 800 mL of Ag sol was first concentrated by employing centrifuge filters (~400 mL) and then transferred to a rotary-evaporation flask. The volume was finally reduced from ~400 mL to 10 mL via rotary-evaporation without disturbing the colloidal stability of Ag NSs.

Formation of Ag Hydrogels and Aerogels. The 10 mL sol was divided into 1 mL aliquots and kept in small glass vials for the gel formation studies. For the formation of opaque Ag

hydrogels, 100 μL of 1% tetranitromethane ($\text{C}(\text{NO}_2)_4$) in acetone was added to each glass vial containing 1 mL of Ag sol. The resulting mixture was vigorously shaken and left in the dark for gel formation. For the formation of transparent Ag hydrogels, 350 μL of 1% $\text{C}(\text{NO}_2)_4$ was added to each glass vial containing 1 mL of Ag NS sol. In both cases, the gradual condensation of the Ag colloids into monolithic hydrogels was observed within 4-12 hours. In addition, different volumes of 1% H_2O_2 (50 to 500 μL) were also employed in the gel formation studies. However, with 1% H_2O_2 , formation of Ag films or mirrors were observed after 4-8 weeks.

The resulting hydrogels were first washed with ultrapure water and then with acetone to remove byproducts of the oxidation. Specifically, the water layer on the top of the Ag hydrogels was removed and the acetone was carefully added along the side wall of the glass vial without breaking the Ag monolith. This process was repeated every 2 hours until the pale yellow color (due to *in-situ* generated HNO_3 acid) of the supernatant disappears, which is about 6-8 times washing. For the preparation of Ag aerogels, CO_2 supercritical drying (SCD) was employed. In a typical drying process, the acetone exchanged Ag wet-gels were loaded into the supercritical dryer and exchanged with liquid CO_2 4-5 times over 12-16 hours at 15°C . Finally, the temperature was raised to 40°C and the wet-gels were dried under supercritical conditions for 20-30 minutes. As a comparable study, Ag xerogels were also prepared by evaporation of the solvent from acetone-exchanged wet-gels over 2-3 days.

3.3 Results and Discussion

The size and shell thickness tunable Ag NSs were prepared by fast chemical reduction of pre-formed Ag_2O NPs. The precursor Ag_2O templates were produced by the reaction of AgNO_3 with

NaOH in the presence of glutathione surfactant. Following the synthesis of the Ag₂O, an aqueous solution of NaBH₄ was quickly injected under vigorous stirring, which caused an immediate color change from pale-yellow to orange-brown, pink, or purple indicating the reduction of Ag₂O into hollow Ag nanostructures. This fast reduction step is found to be critical for the formation of narrowly disperse Ag NSs with uniform size and shell thickness. In contrast, when the reduction reactions were performed with the slow addition of NaBH₄ (0.5 mL/min.) significantly smaller solid NPs (4-6 nm) were produced (Figure 3.1). It has been proposed that the transformation of Ag₂O into hollow Ag NSs is triggered by the slow inward diffusion of NaBH₄ and rapid outward diffusion and dissolution of Ag⁺ via a nanoscale Kirkendall-type reaction.¹⁰⁴ However, in the above report the synthesis of single crystalline Ag NSs with Plasmon band centered at 480 nm is reported and the facile tunability of the NS size and shell thickness has not been reported. In a recent study, synthesis of Ag hollows with SPR maxima in the range of 455-605 nm is demonstrated by varying the nature and concentration of the reducing agent and the thiolate surfactant.¹⁴⁷ However, significantly broad plasmonic bands (full width at half maxima, FWHM = 140-550 nm) were attained owing to poor size and shell thickness control, which is also apparent in the TEM images.¹⁴⁷ Nonetheless, we found that the outer diameter and shell thickness of the Ag NSs can be tuned by varying the concentration of AgNO₃ and thiolates in the reducing mixture and consequently the size of the sacrificial Ag₂O template. This has been achieved through fine tuning the molar ratio of AgNO₃ to glutathione while keeping the moles of NaOH and NaBH₄ constant under ambient conditions. As-prepared Ag NSs display a progression in color from orange-brown to pink or purple as the SPR bands are red-shifted with increasing size and shell thickness (Figure 3.2). The FWHM of the plasmonic bands were in the range of 58-121 nm, indicating the narrow dispersity of as-prepared samples. In contrast, the solid Ag NPs

produced via slow addition of NaBH_4 exhibit a SPR maximum at 410 nm (Figure 3.1). The red shift observed in the SPR for Ag NSs is consistent with previous reports on hollow Au NSs where a similar shift is observed with increasing size and shell thickness. The TEM images of the NSs show that in all samples large hollows have been created (Figure 3.3). The elemental compositions, wavelengths of the SPR maxima, crystallite sizes, shell thicknesses, inner and outer diameters, surface areas and porosities of the selected Ag NSs used in the metallic gel synthesis are reported in Table 3.1.

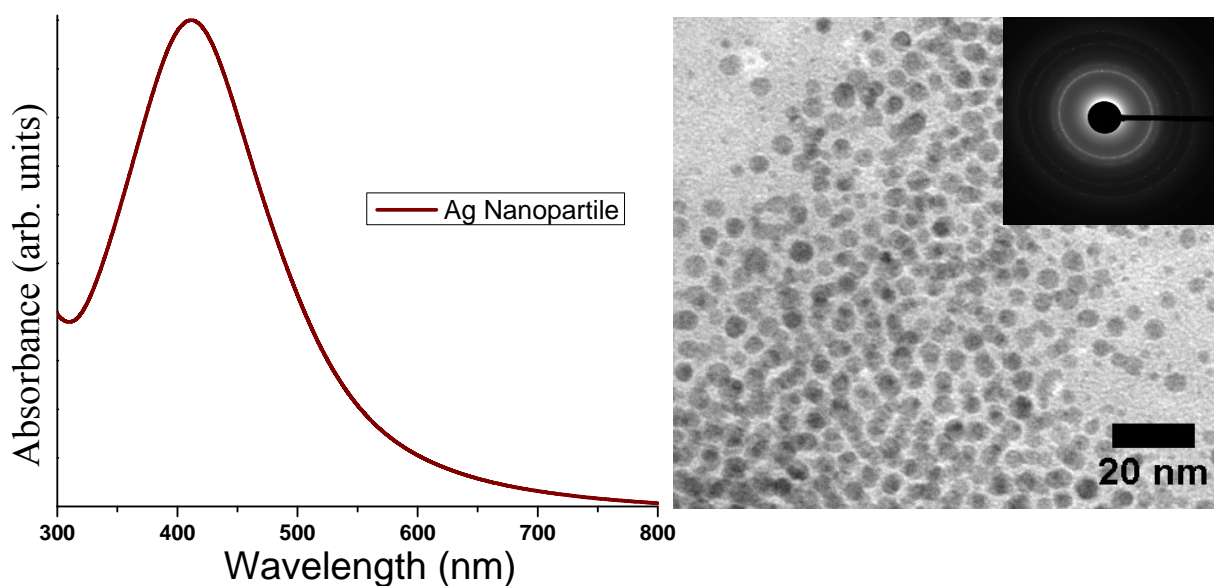


Figure 3.1: (A) UV-visible absorption spectra and (B) a representative TEM of the solid Ag NPs prepared by slow addition of NaBH_4 (0.5 mL/min.). Inset in B shows the electron diffraction pattern, which can be indexed to a cubic lattice (PDF. 01-0870-719).).

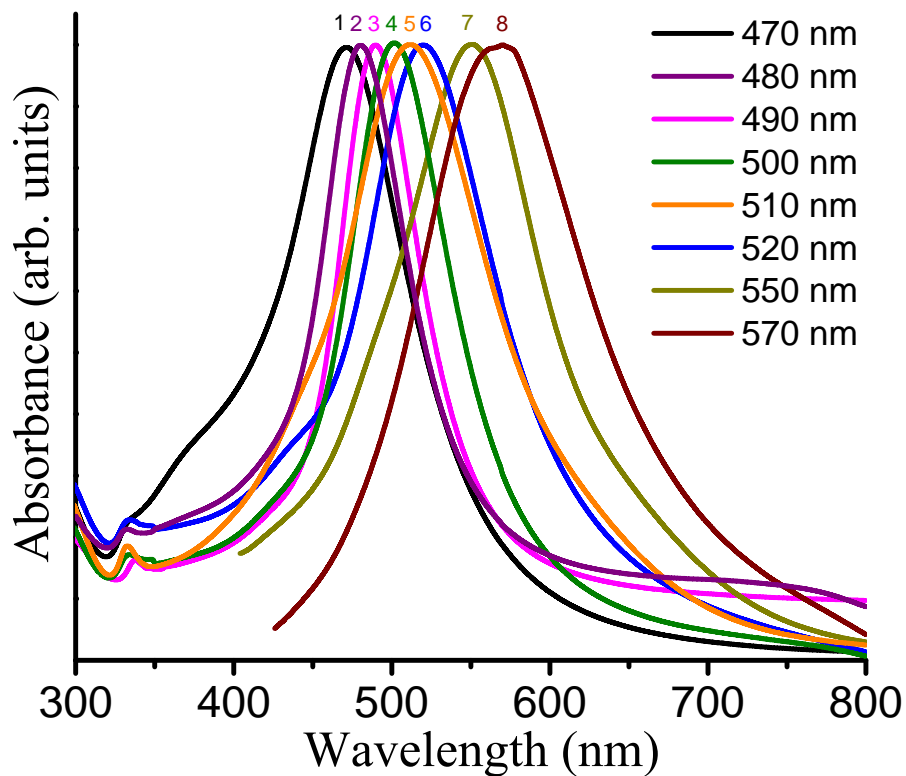


Figure 3.2: Normalize UV-visible absorption spectra of the as-prepared Ag hollow NSs (sample 1 through 8) displaying surface Plasmon resonance maxima at (1) 470, (2) 480, (3) 490, (4) 500, (5) 510, (6) 520, (7) 550, and (8) 570 nm.

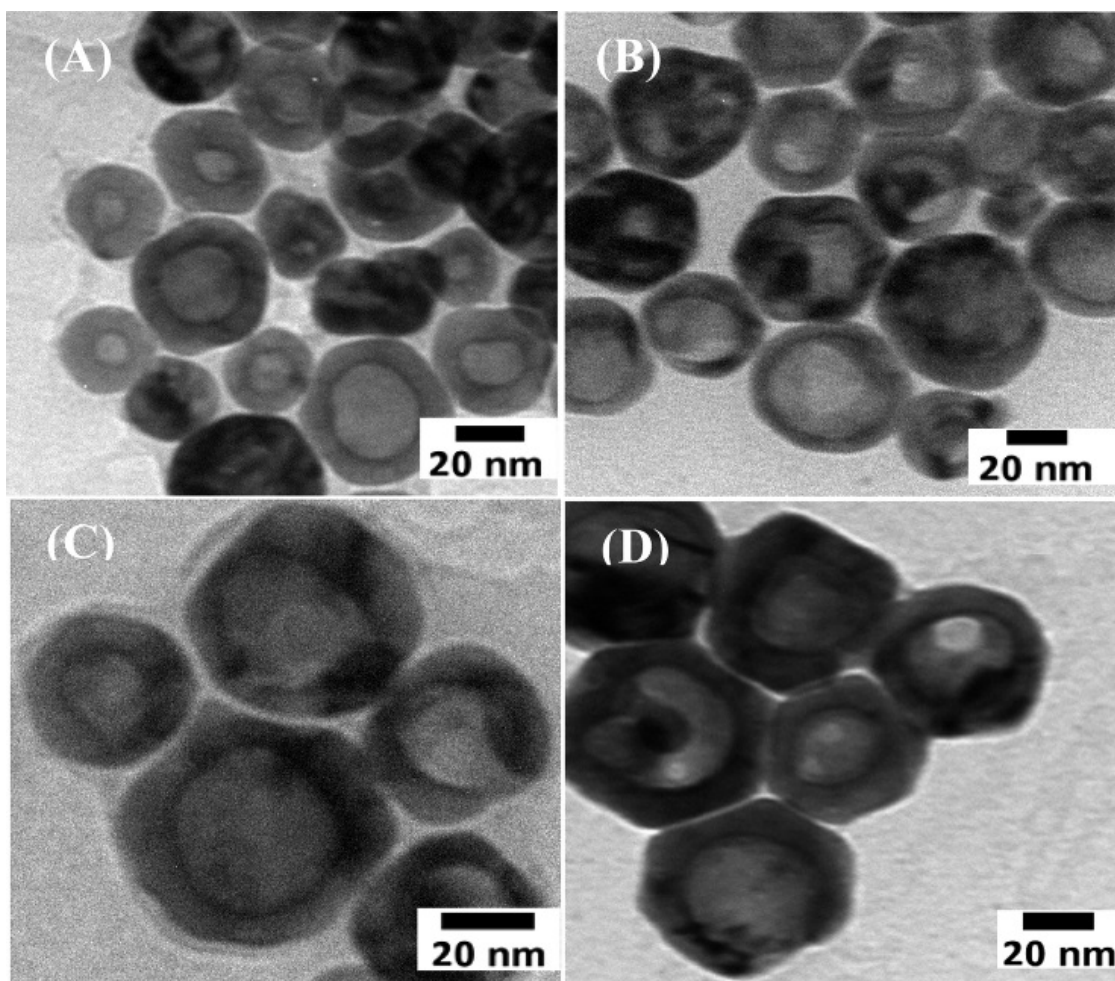


Figure 3.3: Transmission electron micrographs of the Ag hollow NSs displaying (A) 24.1 ± 4.5 , (B) 46.2 ± 5.4 , (C) 55.1 ± 6.5 , and (D) 60.1 ± 7.6 nm average outer diameters.

Table 3.2 Comparison of crystallite sizes, average shell thicknesses, inner and outer diameters, elemental compositions, wavelengths of the SPR maxima, surface areas, average pore diameters, and cumulative pore volumes of the as-prepared Ag NSs (NS I-IV) and the corresponding aerogels (AG I-IV) along with the densities of Ag Aerogels.

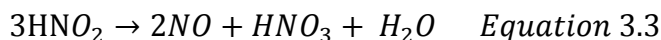
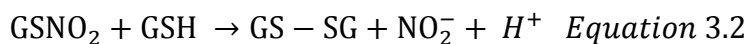
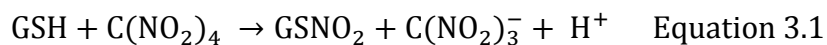
Sample	Nanoshells				Aerogel			
	NS I	NS II	NS III	NS IV	AG I	AG II	AG III	AG IV
Crystallite size (nm) ^a	16.5 ± 0.2	19.6 ± 0.2	22.5 ± 0.2	25.1 ± 0.2	12.3 ± 0.2	17.6 ± 0.2	19.5 ± 0.2	N / A
Shell thickness (nm) ^b	5.8 ± 0.9	9.1 ± 1.2	10.4 ± 1.4	11.2 ± 1.8	5.5 ± 0.9	8.9 ± 1.2	10.1 ± 1.6	N / A
Inner Diameter (nm)	12.5 ± 3.1	28.1 ± 4.8	34.3 ± 5.2	37.7 ± 6.8	11.8 ± 1.5	25.9 ± 2.1	33.1 ± 2.8	N / A
Outer Diameter (nm)	24.1 ± 4.5	46.2 ± 5.4	55.1 ± 6.5	60.1 ± 7.6	22.8 ± 1.9	43.7 ± 3.0	53.3 ± 3.5	N / A
Composition ^c	Ag 86.34% S 13.66%	Ag 85.06% S 14.94%	Ag 84.25% S 15.75%	Ag 83.48% S 16.52%	Ag 95.43% S 4.57%	Ag 96.14% S 3.85%	Ag 95.55% S 4.45%	Ag 96.40% S 3.60%
SPR maxima (nm)	480	500	510	520	N/A	N/A	N/A	N/A
Density (g/cm ³)	N/A	N/A	N/A	N/A	0.041	0.037	0.038	0.04
Surface area (m ² /g) ^d	7.6	6.2	3.1	4.9	127-160	81-98	76-127	43-46
Molar Surface area (m ² /mol) ^e	820.8	669.6	334.8	531.2	1.4-1.7x10 ⁴	0.87-1.1x10 ⁴	0.83-1.4x10 ⁴	4.7-4.9x10 ³
Cumulative Pore Volume (cm ³ /g)	0.021	0.038	0.026	0.027	0.53-0.73	0.28-0.86	0.33-1.12	0.28-0.33
Average Pore Width (nm)	5.2	15.6	12.1	16.6	10.3-17.2	12.8-21.5	20.9-21.3	19.8-21.1

^aCrystallite sizes were calculated by applying the Scherrer formula to all diffraction peaks in the PXRD pattern. ^bAverage nanoshell thicknesses were obtained by measuring the inner and outer diameter of more than 100 nanoshells from TEM images. ^cElemental compositions were obtained by SEM/EDS analysis of multiple samples, and the average values are presented. ^dSurface area values were obtained by applying the BET model to nitrogen adsorption/desorption. ^eMolar surface area values were calculated by multiplying the BET surface area by the molar mass of Ag. ^fAverage pore diameters and cumulative pore volumes were obtained by applying the BJH model to the desorption branch of the respective isotherms.

For the Ag gel synthesis, we have specifically investigated the use of 24.1 ± 4.5 , 46.2 ± 5.4 , 55.1 ± 6.5 , and 60.1 ± 7.6 nm outer diameter Ag NSs representing a wide range of NS sizes and shell thicknesses, which are designated as NS I, NS II, NS III, and NS IV, respectively. Corresponding aerogel products are termed as AG I, AG II, AG III, and AG IV, respectively (Table 3.2). In general, the sol-gel transformation of NP colloids requires highly concentrated sols that can be placed in suitable conditions for the self-assembly.⁸⁹ Typically, the destabilization of NP sol leading to controlled aggregation is achieved by oxidative removal of the surfactant ligands.⁸⁹ It was found that the glutathione functionality provides the highest colloidal stability of Ag NSs as well as efficient destabilization through oxidation as it can strongly complex with the surface Ag and the solvent water molecules. Hence, highly concentrated Ag colloids (0.03-0.05 M) coated with glutathione were prepared by using either the RE or the CF technique.

Initially, we have investigated the synthesis of Ag hydrogels using common oxidants and the concentrated colloids produced by RE technique. The introduction of $C(NO_2)_4$ or H_2O_2 into Ag sols (obtained from rotary evaporation) did not produce corresponding hydrogels; however thin

sheet-like Ag films were obtained after 1-2 months. It is likely that the ionic byproducts (Na^+ , NO_3^- , OH^-) present in the concentrated Ag sols can reduce the stability of NSs resulting in precipitation, followed by decomposition into Ag films. Hence, the purification of Ag colloids prior to the application of oxidant is found to be essential for the successful assembly of NSs. In contrast, CF technique offers an effective method to produce purified Ag colloids via removal of solvated ions along with excess water while retaining the colloidal stability of Ag NSs. Consistent with our hypothesis, monolithic Ag hydrogels were produced after the addition of $\text{C}(\text{NO}_2)_4$ into concentrated Ag sols obtained from CF technique. Nonetheless, attempts to produce Ag gels using H_2O_2 and purified colloids obtained from CF technique were not successful owing to rapid oxidation of glutathione, followed by precipitation of Ag NSs.¹⁴⁸ Conversely, the progressive removal of glutathione was only achieved by employing different volumes (50-500 μL) of 1% $\text{C}(\text{NO}_2)_4$. The addition of $\text{C}(\text{NO}_2)_4$ results in the slow oxidation of thiolates into disulfides as the primary byproduct (Equation 3.1-3.3),¹⁴⁹ creating active sites on the NS surface. Consequently, these active sites can undergo direct cross-linking to produce monolithic Ag hydrogels (Figure 3.4).



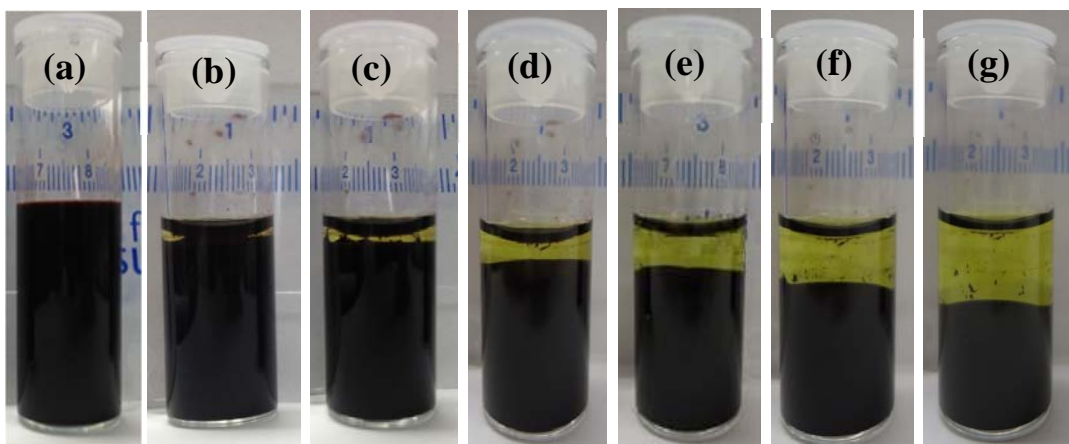


Figure 3.4: Photographs illustrating the transformation of Ag NS sol into an opaque gel and the compaction and syneresis that occurs upon gel aging: (a) concentrated Ag sol, Ag sol (b) 1 h. and (c) 1.5 h. after the addition of $\text{C}(\text{NO}_2)_4$, gel aged for (d) 2 h., (e) 2.5 h., (f) 3.5 h, (g) 5 h. The oxidant/thiolate (X) ratio is 2.2 and the bottom scale bar is in centimeters.

It was also revealed that the ability to transform Ag colloids into a nanoparticulate gel material relies in part on the kinetics by which active sites for the assembly become available on the NS surface. If no sites are available because of the strict passivation by glutathione, Ag colloids are stable in solution, whereas if too many sites become available at one time, rapid precipitation can occur. Therefore, the gelation kinetics can be tuned by varying the quantity of the oxidant relative to the amount of thiolate (glutathione) present in the solution. Accordingly, we found that up to a minimum molar ratio of oxidant/thiolate, $X_{\min} = 1.1$, Ag colloids are highly stable in solution and the gelation is not observed. Above X_{\min} , the rapidity at which gel formation occurs increases with increasing X , until the kinetics are so fast that a precipitate forms in lieu of a gel at $X = 13.2$ (i.e. $12X_{\min}$). At high concentrations of $\text{C}(\text{NO}_2)_4$, the large number of active sites facilitates the interparticle cross-linking, resulting in more compact Ag hydrogels. Likewise, significant polymerization during the gel aging results in dense hydrogels. Therefore,

as a preliminary investigation, the gelation was studied with different molar ratios of oxidant/thiolate. We found that the $X=1.65$ provides the optimum conditions to produce opaque Ag hydrogels retaining the precursor NS morphology, high surface area and porosities. Thereafter, opaque Ag hydrogels were produced primarily with $X=1.65$. Interestingly, when the $X > 7.7$ yellow-brown colored transparent Ag hydrogels were obtained (Figure 3.5). Notably, the transparent hydrogels experienced a much slower condensation rate in comparison to opaque Ag hydrogels. As-synthesized Ag hydrogels were aged under ambient conditions for 6-8 hours and the byproducts of the oxidation (disulfides and sulfonates) were removed by exchanging the solvent 6-8 times with acetone over 1-2 days. Finally, the acetone-exchanged wet gels were dried using supercritical CO₂ to produce monolithic Ag aerogels.

As-prepared Ag aerogels were black (opaque hydrogels) or brownish-black (transparent hydrogels) in color and showed a 5-10% volume loss when compared to acetone-exchanged wet-gels. Interestingly, the monoliths of Ag aerogels exhibit densities as little as 0.037-0.041 g/cm³, representing ~0.4% of the density of bulk Ag. This study offers a novel approach for the construction of metal aerogels with control over physical properties through fine tuning the oxidant/thiolate molar ratio, providing great advantage over previously reported metal NP condensation strategies,⁹¹ which appeared to lack such control over gelation kinetics.

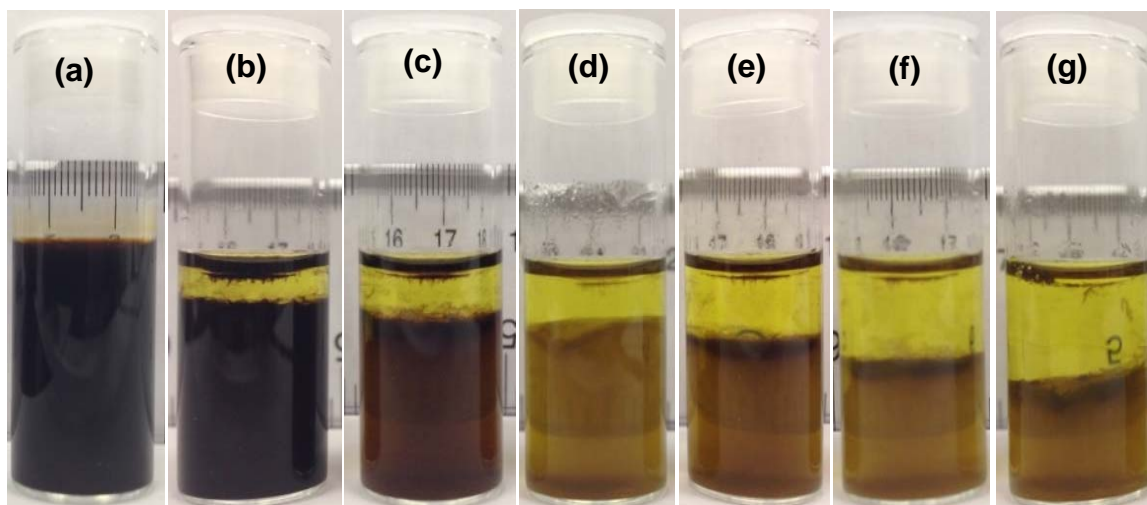


Figure 3.5: Photographs showing the condensation of opaque Ag sol into transparent Ag hydrogel: (a) concentrated Ag sol; (b) sol 2 h. after treatment with $C(NO_2)_4$, gel aged for (c) 4 h., (d) 6 h., (e) 8 h., (f) 10 h., and (g) 12 h. The oxidant/thiolate molar ratio (X) is 7.7.

The oxidative removal of the glutathione ligands from Ag NSs and subsequent SCD drying has no apparent impact on the structure and crystallinity of the Ag NSs that make up the gel framework (Figure 3.6). The X-ray diffraction patterns of the Ag aerogels and xerogels are characteristic of the cubic Ag phase (PDF # 01-0870-719) with broadening of Bragg reflections owing to nanoparticulate nature of the material. The diffraction peaks corresponding to precursor Ag_2O (PDF # 01-0870-719) were not observed in the powder patterns of Ag hollows and corresponding gel products indicating the successful reduction of Ag_2O to metallic silver. Average crystallite sizes estimated based on Scherrer analysis suggest that the Ag crystallites within the gel frameworks are slightly smaller than those of precursor NSs, which is consistent with the TEM measurements (Table 3.2). This can be attributed to oxidative etching of the Ag hollows by $C(NO_2)_4$ and the HNO_3 acid byproducts during self-assembly, which has been

proven to reduce the size of Ag particles.^{150, 151} Nevertheless, the core crystal structure remains unchanged upon gelation and subsequent aero-/xero-gel formation.

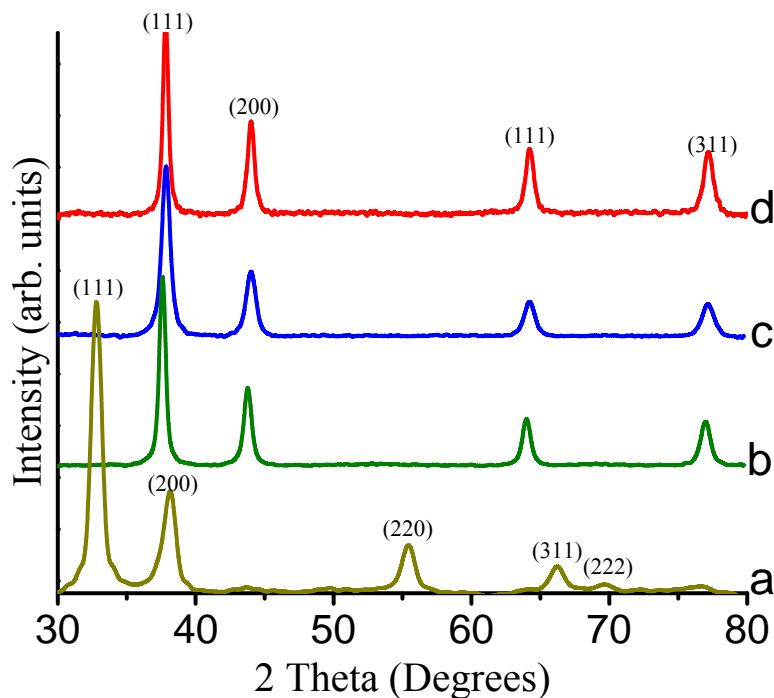


Figure 3.6: Powder X-ray diffraction patterns of the cubic Ag₂O NPs (a) along with the 24.5 ± 4.5 nm outer diameter cubic Ag NSs (b) produced from Ag₂O templates. PXRD patterns of the corresponding Ag aerogels (c) and xerogels (d) produced via oxidative-assembly of Ag NSs.

The elemental compositions of the precursor NSs and aerogels were investigated by employing the SEM/EDS on several individually prepared samples and the average results are shown in Table 3.2. The precursor NSs prepared by the reduction of Ag₂O exhibit two prominent peaks in the EDS spectrum corresponding to Ag and S with atomic ratios in the range of 83-86%: 17-14% (Figure 3.7). In addition, peaks corresponding to oxygen and carbon are also observed in the Ag NSs, which can be attributed to surface bound glutathione ligands. Upon gelation and aerogel formation, no peak for oxygen is detected indicating the successful reduction of Ag₂O to

metallic Ag and the removal of glutathione during the precursor NS synthesis and oxidation-induced self-assembly, respectively. Moreover, the S content is dramatically reduced to 3-5 % in the aerogel product, which further confirms the oxidative removal of glutathione (Table 3.2). As described earlier, Ag hydrogels can also be prepared by varying the oxidant/thiolate molar ratio (X value) in the concentrated colloidal solutions. Using the above phenomena oxidative removal of glutathione can be further established by the fact that the atomic percentage of the S decreases as 5.5, 4.7, 4.1, 2.8, and 2.1% in the corresponding aerogel product when the oxidant/thiolate molar ratio (X) is systematically increased from 1.1, 1.7, 2.2, 3.3, and 4.4, respectively.

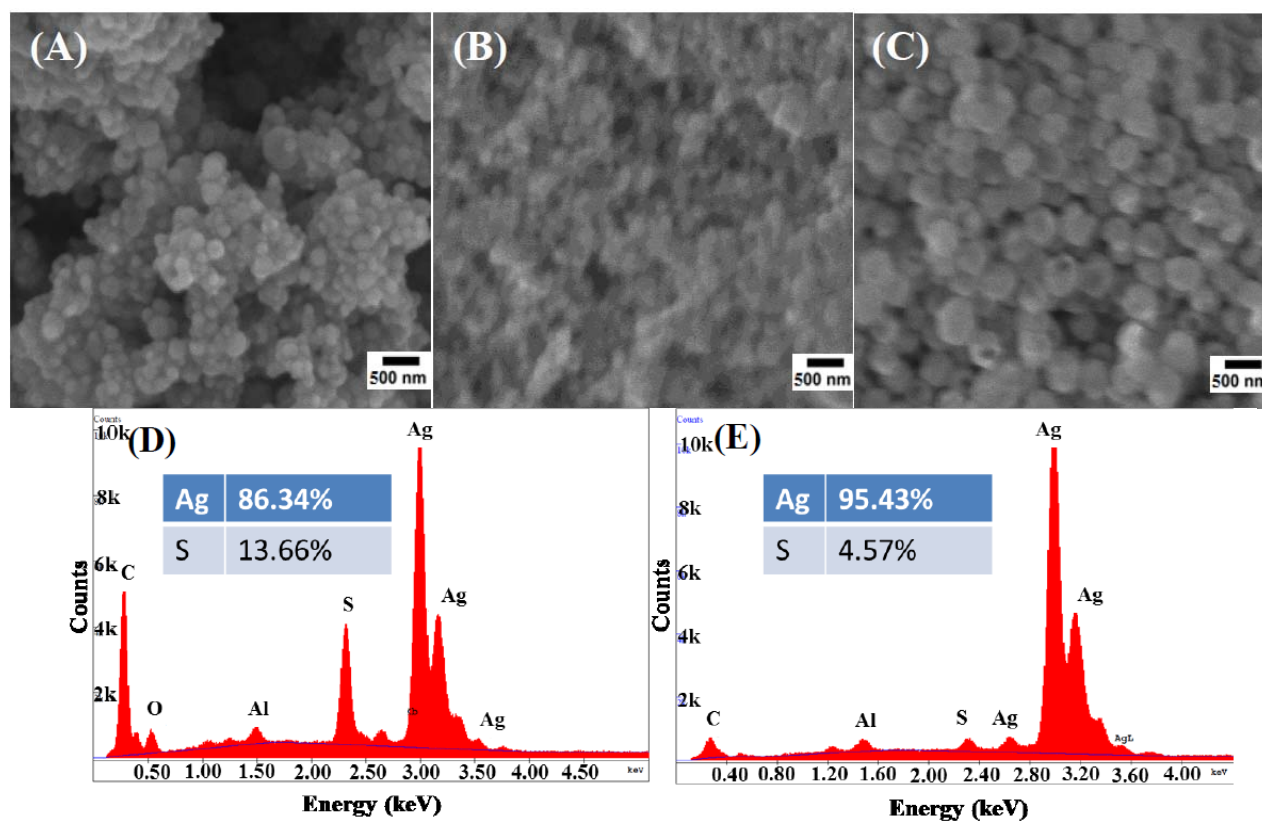


Figure 3.7: SEM images of the as-prepared Ag aerogels (A) and xerogels (B) assembled from 24.1 ± 4.5 nm Ag NSs (C) along with the representative SEM/EDS spectra of the 24.1 ± 4.5 nm outer diameter Ag NSs (D) and corresponding Ag aerogels (E).

In order to monitor the oxidation state of Ag throughout the self-assembly, XPS studies were performed on Ag NSs, corresponding opaque and transparent Ag gel materials. Ag ($3d_{5/2}$) binding energy of 367.6 eV was obtained for precursor NSs indicating nearly complete reduction of Ag_2O to metallic Ag (Figure 3.8A). The Ag metal exhibits a binding energy of 368.0 eV for Ag ($3d_{5/2}$),¹⁵² the negative 0.4 shift observed can be attributed to the presence of surface Ag^+ species that are coordinated to glutathione ligands. Further, the analysis of O (1s) spectrum indicates a binding energies of 530.56 eV and 531.35 eV for O (1s) which can be assigned to the C=O and C-O bonds of the glutathione moiety (Figure 3.8B). The small peak at 533.5 eV in the O (1s) spectrum is likely caused by trapped surface contaminants from exposure to ambient air. If significant Ag_2O is present in the precursor NSs binding energy of 529.0 eV is expected.¹⁵³ The side hump observed at 366.9 eV for Ag ($3d_{5/2}$) can be assigned to Ag-S-C surface states likely formed through coordination of glutathione.¹⁵² Moreover, the S (2p) spectrum (Figure 3.9) has a binding energy of 161.9 eV for S (2p), which can be assigned to the S^{2-} linking the surface Ag^+ with glutathione.¹⁵⁴ In contrast, significant changes in the XPS spectra were observed upon gelation and aerogel formation. In the corresponding opaque and transparent aerogels, the Ag ($3d_{5/2}$) spectra (Figure 3.8C-D) indicate the disappearance of the Ag-S-C species with only metallic Ag present at 368.1 eV. This observation is consistent with the removal of glutathione moiety from precursor NSs and suggests that the oxidation-induced self-assembly has no effect on the valence state of Ag. Further, the examination of the S (2p) spectra of both transparent and opaque aerogels indicate the formation of additional S species, which are likely to produce through oxidation of glutathione into disulfides and sulfonates (Figure 3.9).¹⁴⁸

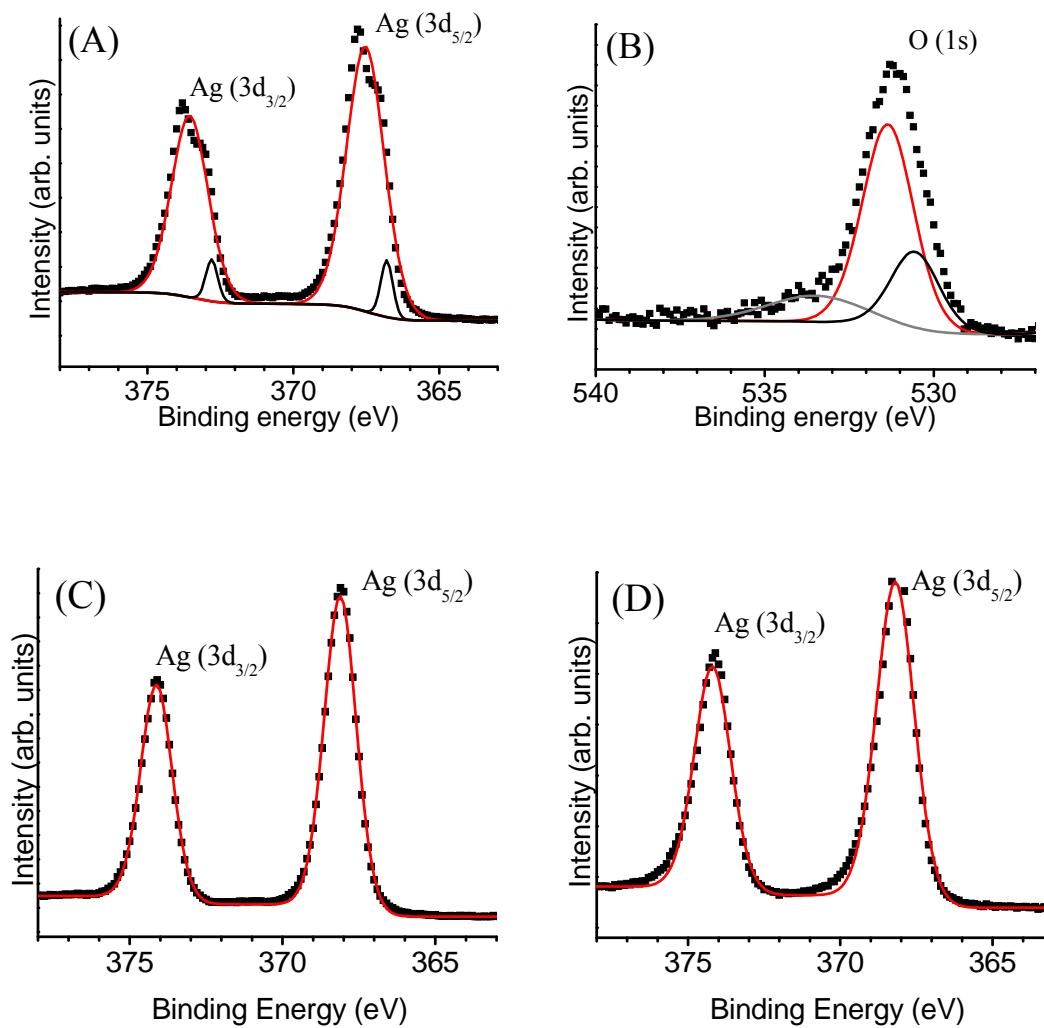


Figure 3.8: The (A) Ag (3d_{5/2}) and (B) O (1s) XPS spectra of the precursor NSs along with the Ag (3d_{5/2}) spectra of the aerogels produced from (C) opaque and (D) transparent Ag hydrogels. The dotted lines represent spectral data. Solid black, gray and red lines are the fitted deconvolutions.

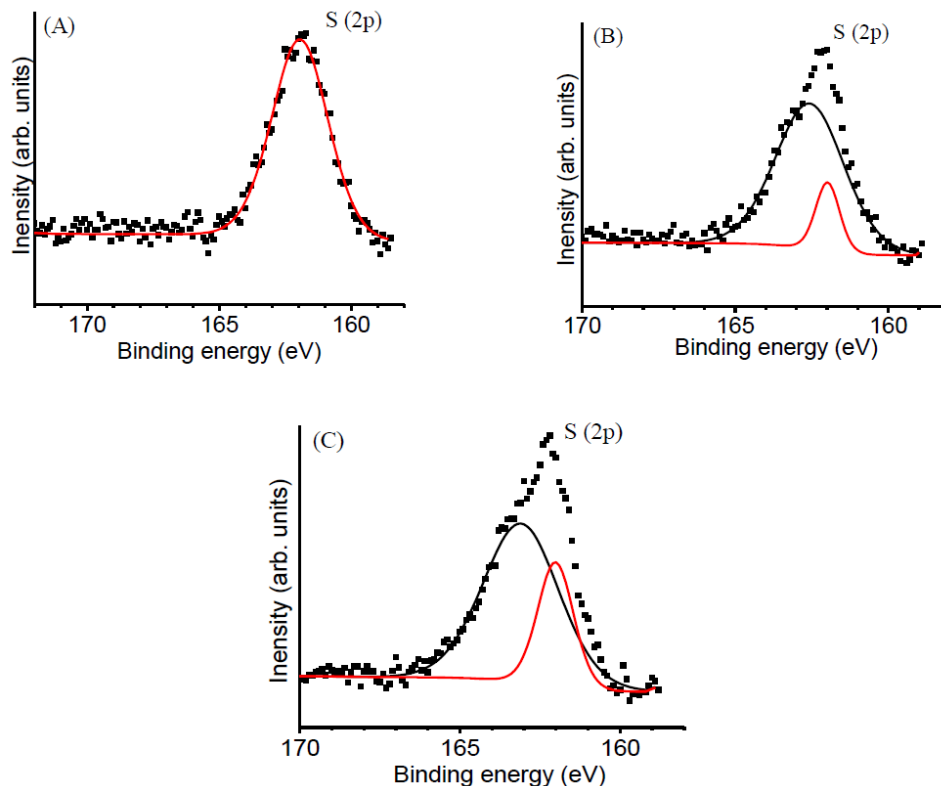


Figure 3.9: The S (2p) XPS spectra of the (A) precursor Ag NSs and the aerogels produced from (B) opaque and (C) transparent Ag hydrogels. The dotted lines represent spectral data. Solid black and red lines are the fitted deconvolutions.

Transmission (TEM) and scanning (SEM) electron microscopies were employed to investigate the morphology of Ag NSs, corresponding opaque and transparent Ag aerogels. As shown in Figure 3.3, precursor NSs exhibit hollow morphology with narrowly dispersed size and shell thickness, which is consistent with the tunable plasmonics observed in the visible spectrum (Figure 3.2). Representative SEM and TEM images of opaque aerogels are shown in Figure 3.10A and 3.3.11A-D, respectively. SEM images indicate the highly porous morphology of the aerogel product displaying pearl necklace aggregates of precursor particles (Figure 3.10A). In contrast, a larger degree of fusion and densification is observed in the bench-top dried xerogel samples (Figure 3.10B and 3.11E). Similarly, the TEM images of the aerogels assembled from

NS I, NS II, and NS III particles exhibit an inter-connected network of Ag hollows that have typical dimensions in the same scale as precursor particles (Figure 3.11A-C and Figure 3.12). Thus, the corresponding Ag aerogels (AG I-III) are likely to produce through direct cross-linking of hollow NSs into fractal aggregates and are morphologically similar to traditional base-catalyzed silica aerogels.⁵ However, the gel frameworks assembled from NS IV particles exhibit significant changes in morphology (Figure 3.11D) in comparison to precursor NSs (Figure 3.3D). The AG IV product consists of an inter-connected network of large Ag hollows and small NPs, which are appeared to result from breakup of the precursor NSs. The origin of small NPs can be attributed to lower stability of significantly larger hollows that can breakup into smaller NPs (6–20 nm) upon oxidation-induced self-assembly. However, the presence meso (2–50 nm) to macro (> 50 nm) porous network with a wide range of pore diameters is clearly visible in all aerogel samples.

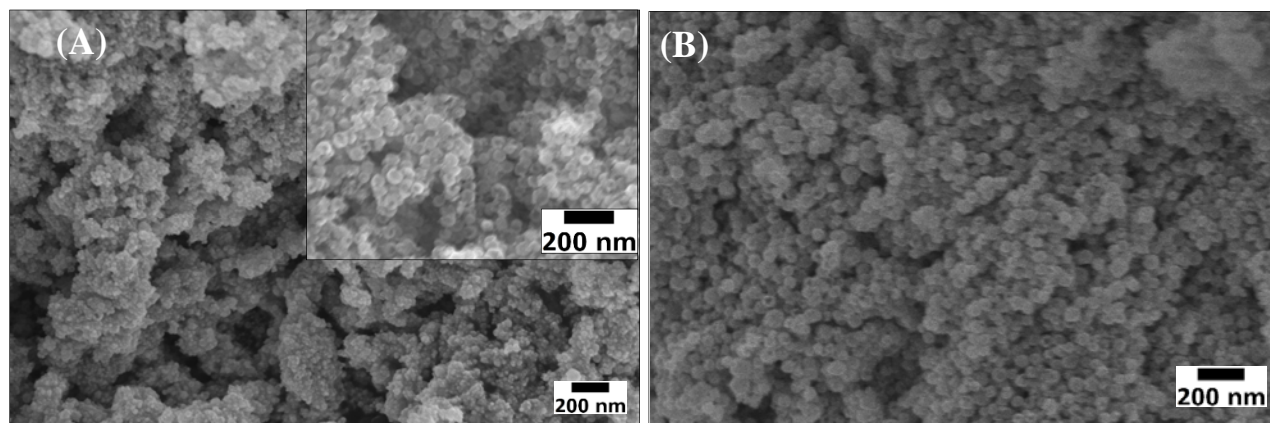


Figure 3.10: Representative SEM images of opaque (A) Ag aerogels and (B) xerogels assembled from 24.1 ± 4.5 nm outer diameter Ag NSs. Inset in (A) shows the high resolution SEM image depicting the inter-connected network of Ag hollow particles.

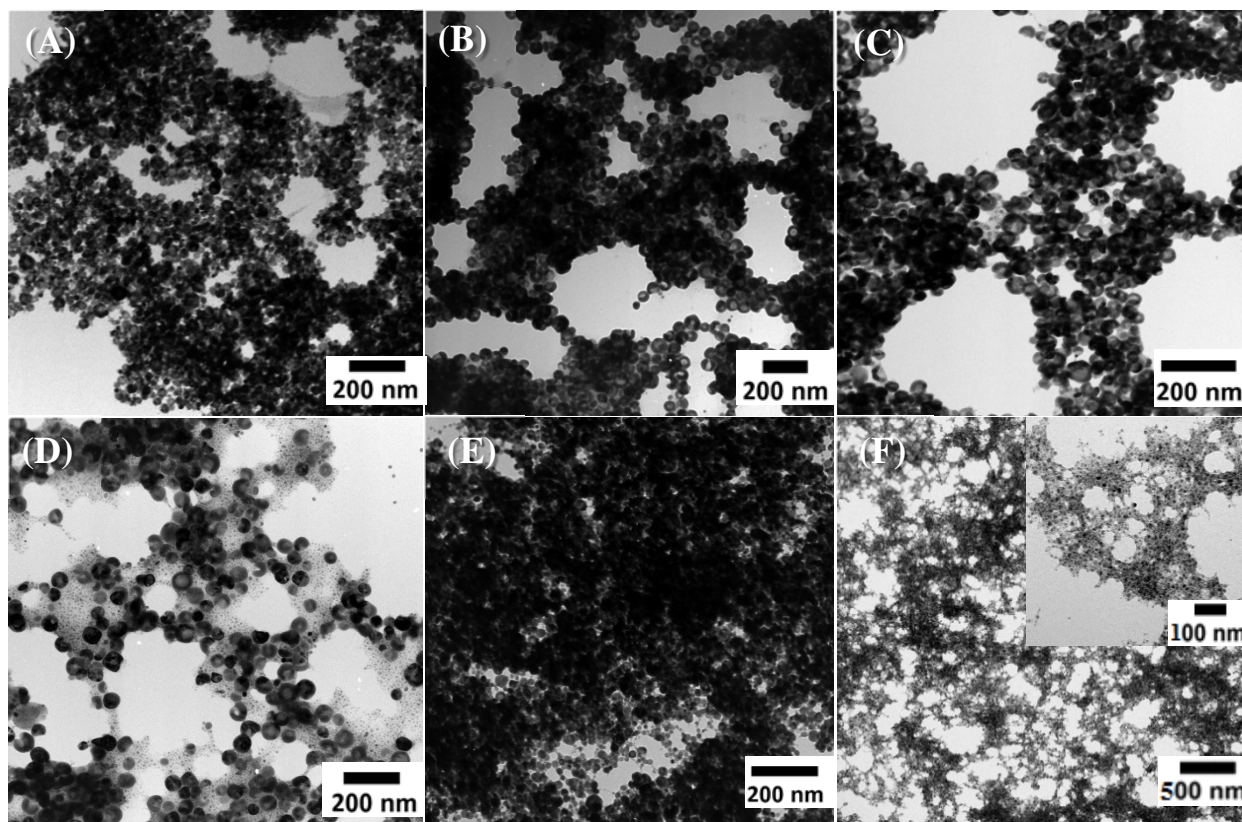


Figure 3.11: TEM images of the aerogels assembled from (A) 24.1 ± 4.5 nm, (B) 46.2 ± 5.4 nm, (C) 55.1 ± 6.5 nm, and (D) 60.1 ± 7.6 nm outer diameter Ag NSs. TEM images of the (E) xerogels and (F) aerogels derived from 24.1 ± 4.5 nm outer diameter NSs and transparent hydrogels, respectively. The inset in F shows the magnified image of the sample F. The dark contrast areas in A-F represent multiple layers of particles depicting the 3-dimensional connectivity of Ag NSs.

As discussed above, if a large excess of oxidant is used in the self-assembly process, optically transparent Ag gel materials can be produced (Figure 3.5). TEM analyses of the corresponding aerogels exhibit significantly smaller (3.2-7.6 nm) NPs that are 3-dimensionally linked together to produce pearl necklace aggregates (Figure 3.11F and Figure 3.13). It is likely that the precursor NSs are no longer stable as hollows in the transparent hydrogels hence, can

breakup into significantly smaller NPs (3.2-7.6 nm) in the presence of excessive oxidant ($X > 7.7$). It was revealed that the oxidative removal of glutathione generates HNO_3 acid as a byproduct resulting in a slightly acidic Ag sol (Equation 3.3). The in-situ generated HNO_3 is likely to etch the larger Ag hollows into significantly smaller NPs yielding transparent Ag hydrogels (Figure 3.5). Relatively slower condensation rate observed in the formation of transparent hydrogels is likely caused by the slower etching rate of Ag by in-situ generated HNO_3 acid. Previously, it has been reported that the transparent chalcogenide gel materials can be produced when the size of NP aggregates falls below the wavelength of visible light.^{86,87,155,156} Brock et al. have extensively studied the gelation kinetics of CdSe NPs and concluded that the smaller NPs can undergo reaction limited colloidal aggregation resulting in aggregates that are smaller than the wavelength of visible light, leading to optical transparency.¹⁵⁵ Whereas, with larger NPs, the aggregates formed at the gelation point are much larger than the wavelength of visible light, resulting in increased scattering and opacity. Likewise, the Ag hydrogels assembled from larger hollows (~24-60 nm) exhibit opaque gel materials while the smaller NP building blocks (~3.2-7.6 nm) can potentially result in transparent Ag gel materials.

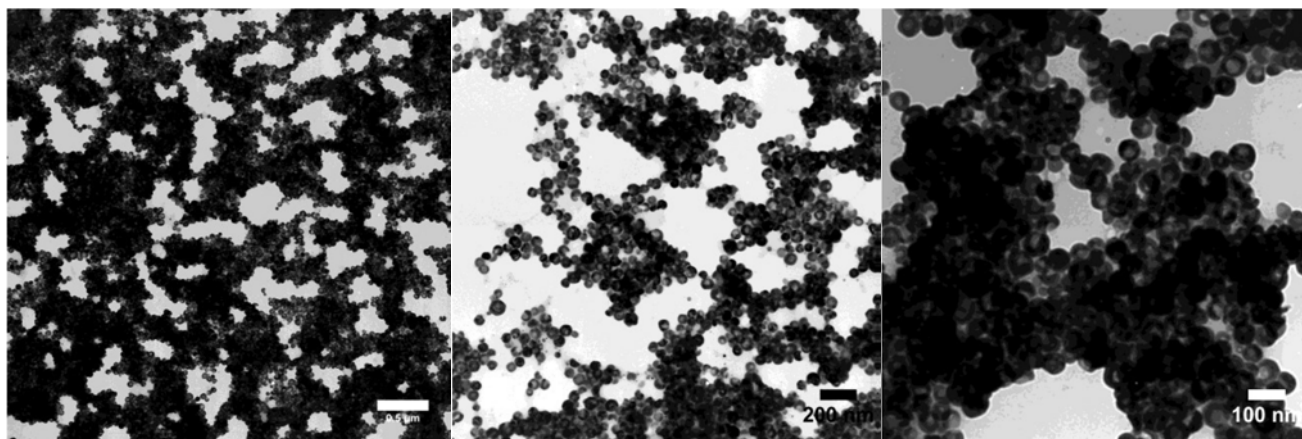


Figure 3.12: Representative TEM images of the opaque Ag aerogels assembled from of 46.2 ± 5.4 nm outer diameter Ag NSs. The oxidant/thiolate molar ratio is 1.65.

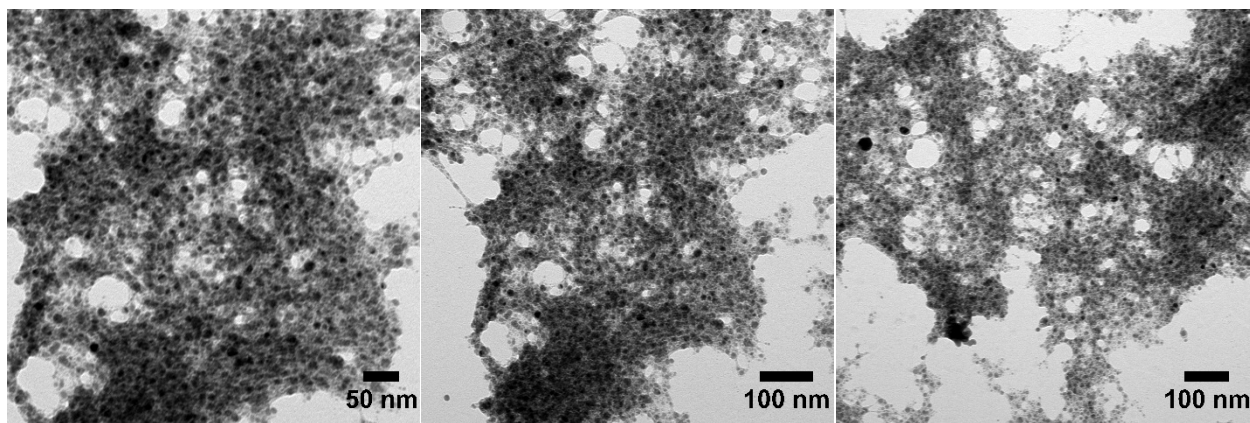


Figure 3.13: Representative TEM images of the Ag aerogel prepared from transparent hydrogels produced via self-assembly of 24.1 ± 4.5 nm outer diameter Ag NSs. The oxidant/thiolate molar ratio is 7.7.

The low-density, highly porous structure of the metallic Ag aerogels is further reflected in the surface area and porosimetry plots modeled from the nitrogen adsorption/desorption isotherms (Figure 3.14). Both transparent and opaque Ag aerogels exhibit similar-shaped isotherms that can be classified as a type IV curve, characteristic of a mesoporous (2-50 nm) material with a sharp upturn in the high-relative-pressure region that corresponds to a type II curve indicating the capillary condensation and some degree of macroporosity (>50 nm).^{143,144} The shapes of the hysteresis loops of all samples reveal a combination of H1 and H3 character suggesting the presence of cylindrical-shaped and slit-shaped pores, respectively.¹⁴⁴ The surface area calculated based on Brunauer-Emmett-Teller (BET) model is in the range of 43-160 m²/g (~ 4.7 - 17.2×10^3 m²/mol) for opaque aerogels whereas the aerogels produced from transparent hydrogels exhibit a slightly higher surface area (175-182 m²/g or 18.9 - 19.7×10^3 m²/mol), which is consistent with the significantly smaller NPs present in the transparent Ag gel frameworks (Figure 3.11F). In general, a systematic decrease in surface area with increasing outer diameter and shell thickness of precursor NSs is observed for AG I through AG III samples (Table 3.2). In

contrast, the hollow Ag NSs are significantly less porous and exhibit BET surface areas in the range of 3.1-7.6 m²/g (~334-821 m²/mol). The enormously high surface areas obtained for Ag aerogels in comparison to precursor NSs can be attributed to low-density highly porous architecture of the aerogel framework, which provides the superior accessibility of chemical species to inner and outer surfaces of the hollows, offering new perspectives for future applications.

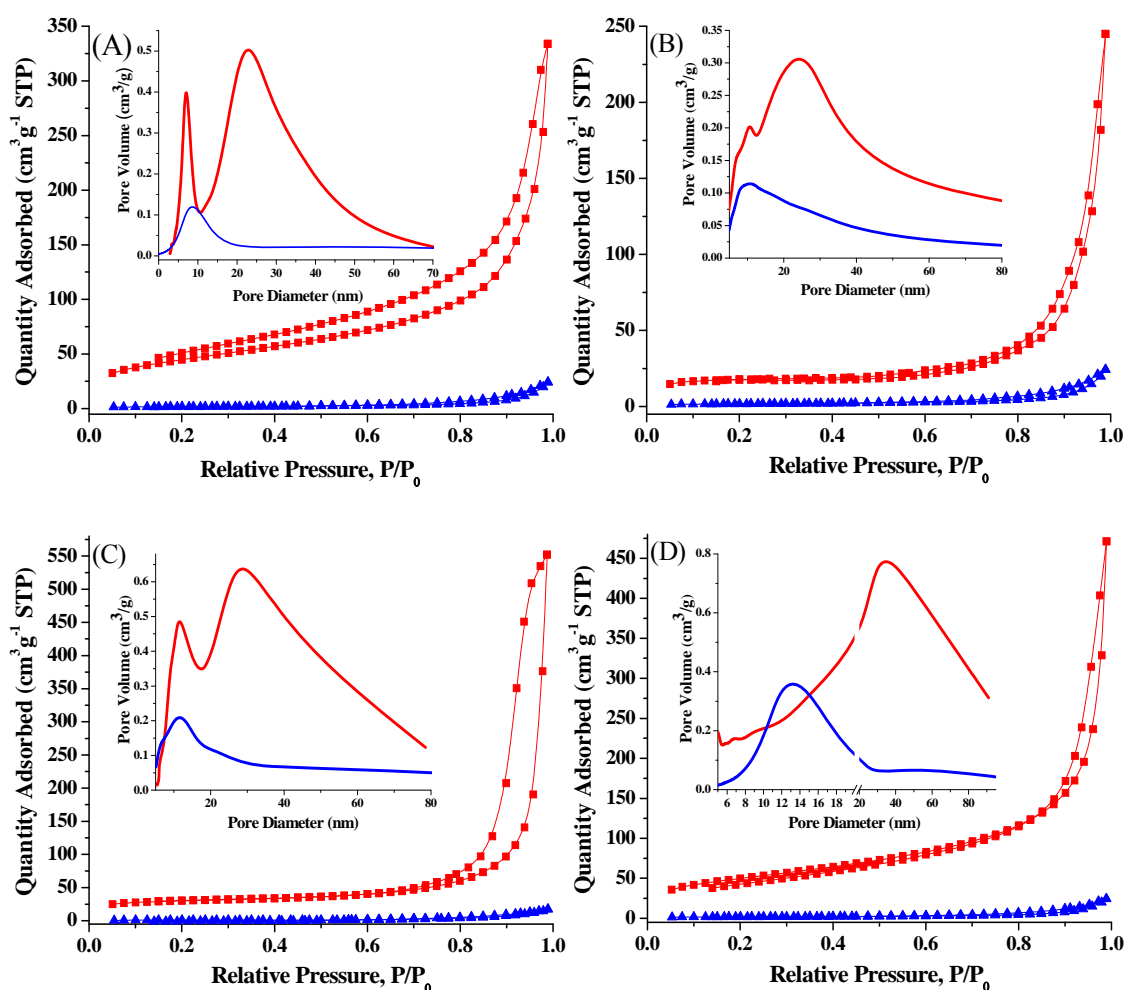


Figure 3.14: Nitrogen adsorption/desorption isotherms of precursor Ag NSs (blue) and corresponding aerogels (red) assembled from (A) 24.1 ± 4.5, (B) 46.2 ± 5.4, (C) 55.1 ± 6.5 nm

outer diameter Ag NSs and (D) the aerogels produced from transparent hydrogels. Respective BJH pore distribution plots of Ag NSs (blue) and aerogels (red) are shown as insets.

The average pore diameters and cumulative pore volumes of the Ag aerogels were obtained from the desorption branches of the nitrogen adsorption/desorption isotherms using Barrett-Joyner-Halenda (BJH) model. As a comparable study, pore size distribution plots of precursor NSs were also modeled using the respective isotherms. The pore distribution analyses (Figure 3.14A-D insets) of transparent and opaque Ag aerogels exhibit a broad range of pore sizes, extending from the meso-to-macro-pore region, yielding average diameters in range of 10.3-21.3 nm (Table 3.2). Interestingly, the opaque Ag aerogels retaining the hollow morphology of precursor NSs exhibit two distinct pore distributions in the mesoporous (2-50 nm) region. For instance, the aerogels assembled from 24.1 ± 4.5 nm outer diameter NSs demonstrate a narrow pore distribution centered at ~ 7 nm and a much broader pore distribution ranging from 15-50 nm (Figure 3.14A inset). In contrast, precursor NSs exhibit a single pore distribution centered at ~ 8 nm, which is likely to arise from the hollow cavity of the particles. Accordingly, the narrow pore distribution centered at ~ 7 nm of the aerogel product can be attributed to hollow interior of the precursor NSs whereas the latter distribution reflects the continuous meso-to-macro-pore network created by the 3-dimensional assembly of Ag NSs. The relative area under those two distributions represents the contribution from each towards the cumulative pore volume and the gel framework assembled from 24.1 ± 4.5 nm Ag NSs exhibits $\sim 17\%$ and $\sim 83\%$ contribution from NS pores and network pores, respectively. Similar pore distributions were obtained for aerogels assembled from 46.2 ± 5.4 and 55.1 ± 6.5 nm outer diameter NSs as they retain the hollow morphology of the nano-sized constituents (Figure 3.14B and C). Therefore, unlike the traditional metal oxide or the dense NP based gel materials, the metallic aerogels reported in this

study are unique nanoarchitectures that can exhibit tunable surface areas and porosities even within a traditionally non-ordered superstructure. This unique pore size tunability can in principle be useful in the selective analysis of chemical species as a function of the inner diameter of the NSs, which can potentially create customized gel frameworks for future catalytic and sensing applications. In contrast, the aerogels constructed from 60.1 ± 7.6 nm outer diameter Ag NSs (Figure 3.15) and the transparent Ag hydrogels (Figure 3.14D) exhibit a single pore distribution that corresponds to network pores owing to lack of hollow particles in the corresponding gel structures.

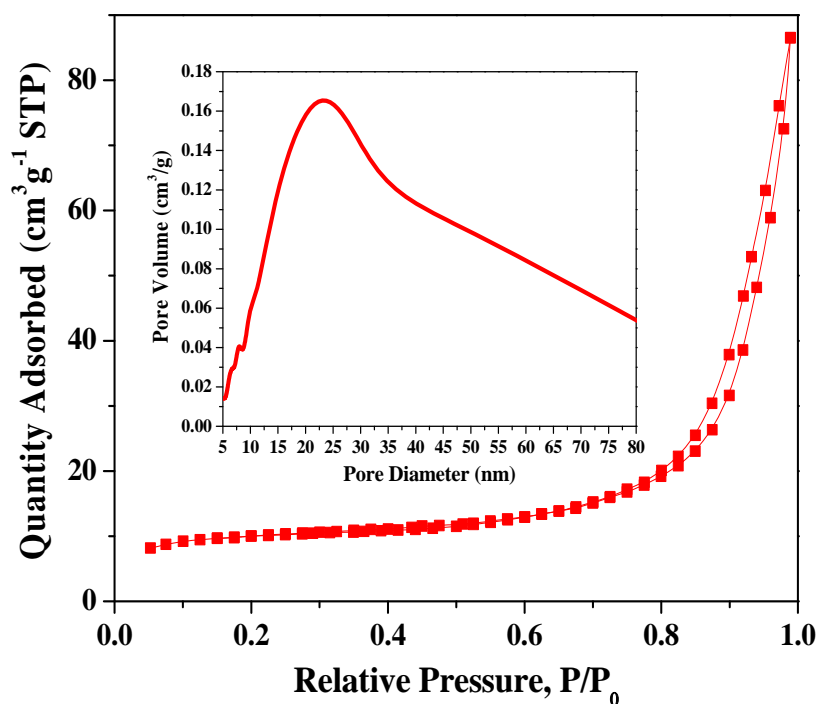


Figure 3.15: Nitrogen adsorption/desorption isotherm of the Ag aerogels assembled from 60.1 ± 7.6 nm outer diameter Ag NSs. The corresponding BJH pore size distribution plot is shown as an inset. The aerogels were degassed at 50°C for 24 h. prior to the analysis.

3.4 Conclusion

In conclusion, we have successfully synthesized different sizes and shell thicknesses of the Ag hollow NPs with tunable SPR from 470 nm to 570 nm. Due to the existence of coordinating ligand glutathione, the Ag hollow NPs solution can be concentrated using centrifuge filters to yield high-concentrated sols. With the introduction of the oxidizing agent, tetranitromethane, glutathione functionality can be removed from the surface as disulfides, leaving active spots on the Ag hollow NPs surface to build direct cross-linking between NPs. By changing the oxidant/thiolate ratio, the morphology, opacity, surface area and porosity of the aerogel were tuned. The resultant aerogels exhibit pearl necklace morphology of the base-catalyzed silica aerogel, and interconnect meso-to-macro porous structures offering new perspectives for functional applications. More importantly, as prepared opaque Ag aerogels porosity of the opaque aerogel can be partially tuned through using different inner diameter of the precursor hollow NPs. These unique properties of the Ag hydro/aerogels make them attractive for potential use in electrocatalysis, chemical sensing applications.

Chapter 4: Direct Cross-Linking of Au/Ag Alloy Nanoparticles into Monolithic Aerogels for Application in Surface Enhanced Raman Scattering

4.1 Introduction

Noble metal alloy NPs with unique catalytic activity, plasmonic tunability, and increased surface reactivity have gained noteworthy interest due to their enormous potential in advanced technologies. Among these applications, SERS has been a surface-sensitive technique that enhances Raman scattering by molecules adsorbed on the metal substrate. The extent of SERS enhancement generally depends on the nanoscale characteristics of the plasmonic substrates such as morphology, size, and degree of colloidal aggregation. Although extremely high SERS effects with single molecule detection have been reported for periodic arrays of Ag NPs, self-organized Au and Ag NPs in solution, and nanoporous metal foams, reliable substrates with uniform and reproducible SERS effects are yet to be developed for practical applications. Wang's group reported that the fractal NP aggregates are efficient materials to generate high electromagnetic fields and greater SERS effects, whereas a number of other studies suggest the highly porous, rough metallic surfaces have the potential to offer optimal SERS effects. Therefore, assembling Au and Ag together into porous NP aggregates can potentially increase the SERS effects. Since the oxidative sol-gel assembly of Ag hollow NPs has offered a promising approach for producing Ag aerogel, further expansion this technique to make Au/Ag alloy aerogel as the SERS substrate may be better for SERS application and more cost effective. In this case, alloying Au with the Ag hollow NPs and assemble them into aerogels with directly cross-linked NPs can exhibit mesoporous and rough metallic surfaces, which enable rapid diffusion of analytes to plasmonic hot-spots and stronger SERS intensities can be observed.

In this chapter, three distinct morphologies of Au/Ag alloy NPs and hollow NPs has been synthesized with Ag hollow NPs as sacrificial template. In addition, three different morphologies of Au/Ag alloy aerogels via oxidative self-assembly of the corresponding NPs were also reported. The resultant aerogels exhibit high surface areas, low densities and tunable pore size distribution. The SERS activity of alloy aerogels is studied using Rhodamine 101 (Rd 101) as the probe molecule and significant signal enhancement is achieved. The aerogels' physical and chemical properties, as well as SERS performance are thoroughly discussed.

4.2 Experimental Section

Materials

Silver nitrate (99.9%) and sodium borohydride (98%) were purchased from Strem Chemicals. Hydrogen tetrachloroaurate (III), tetranitromethane ($\text{C}(\text{NO}_2)_4$) and L-glutathione (GSH) reduced (98%) were purchased from Sigma-Aldrich. Ascorbic acid (98%), Rhodamine 101 inner salt (99%), sodium hydroxide (ACS grade), ethanol (ACS grade) and acetone (ACS grade) were purchased from Fisher. The water used in all syntheses was 18.2 M Ω Milli-Q filtered. All chemicals were used as received without further purification.

Synthesis of Ag Hollow NPs

Size and shape controlled Ag hollow NPs were prepared by following a literature synthetic method.¹⁵⁷ Briefly, 50 mL of Milli-Q filtered water was added to a 250 mL round bottom flask and kept in an ice-water bath. To this solution, 1 mL of 10 mM AgNO_3 and 100 μL of 10 mM GSH were added, followed by the addition of 10 mL of 0.1 M NaOH with vigorous stirring. After 2 min, a freshly prepared NaBH_4 solution (3.6 mL, 10 mM) was swiftly injected to produce Ag hollow NPs. The resulting mixture was stirred at room temperature for 30 min and used for

subsequent GRRs. The Ag hollow NPs with different outer diameters and wall thickness were produced by varying the AgNO₃: GSH molar ratio as reported in the literature.³¹

Synthesis of Au/Ag Alloy NPs

The Au/Ag hollow NPs were prepared by GRRs of the as-synthesized Ag hollow NPs with hydrogen tetrachloroaurate (III). In a typical synthesis, a solution of ascorbic acid (200 μ L, 10 mM) was mixed with the Ag hollow NP solution and appropriate volumes of 0.5 mM HAuCl₄ were injected at a rate of 1 mL min⁻¹, which were 7.00 mL, 11.00 mL, and 14.00 mL to produce Au/Ag alloy NP I, II, and III, respectively. The resulting solutions were stirred slowly for 30 min during which a color change from orange-brown to pink or purple-blue was noted, indicating the growth of Au/Ag alloy NPs.

Preparation of Concentrated Colloidal Sols of Au/Ag NPs

The concentrated Au/Ag NP sols were produced by employing the centrifugal filtration technique and Sartorius Vivaspin centrifuge filters (MWCO 300,000). Typically, the centrifuge filters were filled with 20 mL of the as-prepared NP sol and centrifuged at 3500 rpm for 10 min to remove excess water and ionic byproducts. This process was continued multiple times to reduce the total volume of NP sol from ~600 mL to 8 mL to produce a concentrated (10 mM) Au/Ag sol.

Preparation of Au/Ag Alloy Hydrogels and Aerogels

As-prepared Au/Ag sol was divided into 2 mL aliquots and 50 μ L of 1% C(NO₂)₄ was added to each aliquot. The resulting mixtures were kept in the dark after vigorous shaking. The gradual condensation of the NP sols into solvent swollen, opaque hydrogels was noted within 4-6 h. The resulting hydrogels were washed with acetone multiple times to remove the byproducts of oxidation and unreacted C(NO₂)₄. The CO₂ supercritical drying was employed to produce Au/Ag

alloy aerogels. In a typical drying process, the acetone exchanged gels were loaded into the supercritical dryer and exchanged with liquid CO₂ at 15 °C. Finally, the temperature and pressure of the system were raised to 40 °C and 1200 psi for 20 min. to produce Au/Ag alloy aerogels.

4.3 Results and Discussion

Recently, our group reported the synthesis of size and shape controlled Ag hollow NPs that exhibit tunable inner and outer diameters, wall thicknesses, and surface Plasmon resonances (SPR) via fast chemical reduction of preformed Ag₂O NPs.¹⁵⁷ The precursor Ag₂O NPs were produced by a reaction of AgNO₃ with NaOH in the presence of GSH surfactant. The rapid reduction of Ag₂O NPs yields hollow Ag nanostructures via Kirkendall effect in which the differences in diffusion rates of Ag₂O (outward, fast) and NaBH₄ (inward, slow) result in the depletion of matter in the particle interior.^{104,158} Since there are no reports on the synthesis of Au/Ag alloys by employing sacrificial hollow templates, initial efforts were focused on the investigation of Au/Ag alloy nanostructures that can be produced via galvanic replacement of the hollow Ag NPs. It has been reported that the size dispersity and morphology of Ag NP precursors influence the morphology of alloy nanostructures produced via GRRs.¹⁵⁹ Accordingly, hollow Ag NPs with three distinct inner and outer diameters and wall thicknesses were employed in the GRRs. As-prepared Ag templates exhibit outer diameters of 38.2 ± 9.1, 46.2 ± 5.4, 55.1 ± 6.5 nm, wall thicknesses of 5.8 ± 0.9, 9.1 ± 1.2, 10.4 ± 1.4 nm, and SPR maxima at 480, 500, 510 nm, respectively (Figure 4.1). These NPs were allowed to react with HAuCl₄ in the presence of a co-reductant (ascorbic acid) to facilitate the growth of Au/Ag alloy NPs.^{160,161} Although the larger difference in reduction potentials of Au³⁺ and Ag⁺ allows the galvanic replacement under ambient conditions, the presence of ascorbic acid is expected to

facilitate the alloying process and control the size-dispersity of alloy NPs. It was noted that the production of enclosed Au/Ag alloy nanostructures is stringently depend on the outer diameter and wall thickness of the precursor NPs. If GRRs were performed on the larger hollows with outer diameter of 55.1 ± 6.5 nm and wall thickness of 10.4 ± 1.4 nm, the template broke apart and a wide dispersity of Au/Ag alloy nanostructures (2-30 nm) were obtained (Figure 4.2). The smallest Ag hollow NPs, with outer diameter of 38.2 ± 9.1 nm and wall thickness of 5.8 ± 0.9 nm, retained an enclosed hollow structure. However, the resultant Au/Ag alloys exhibit a wider dispersity of aggregated NPs (Figure 4.2). Therefore, to produce enclosed Au/Ag alloy nanostructures with narrower size dispersity, the precursor Ag hollow NPs with 46.2 ± 5.4 nm outer diameter and 9.1 ± 1.2 nm wall thickness were employed in the GRRs. It should be noted that the unreacted NaBH_4 must be decomposed prior to GRRs; otherwise HAuCl_4 will be inadvertently reduced by residual NaBH_4 to produce a heterogeneous mixture of Au and Ag NPs.

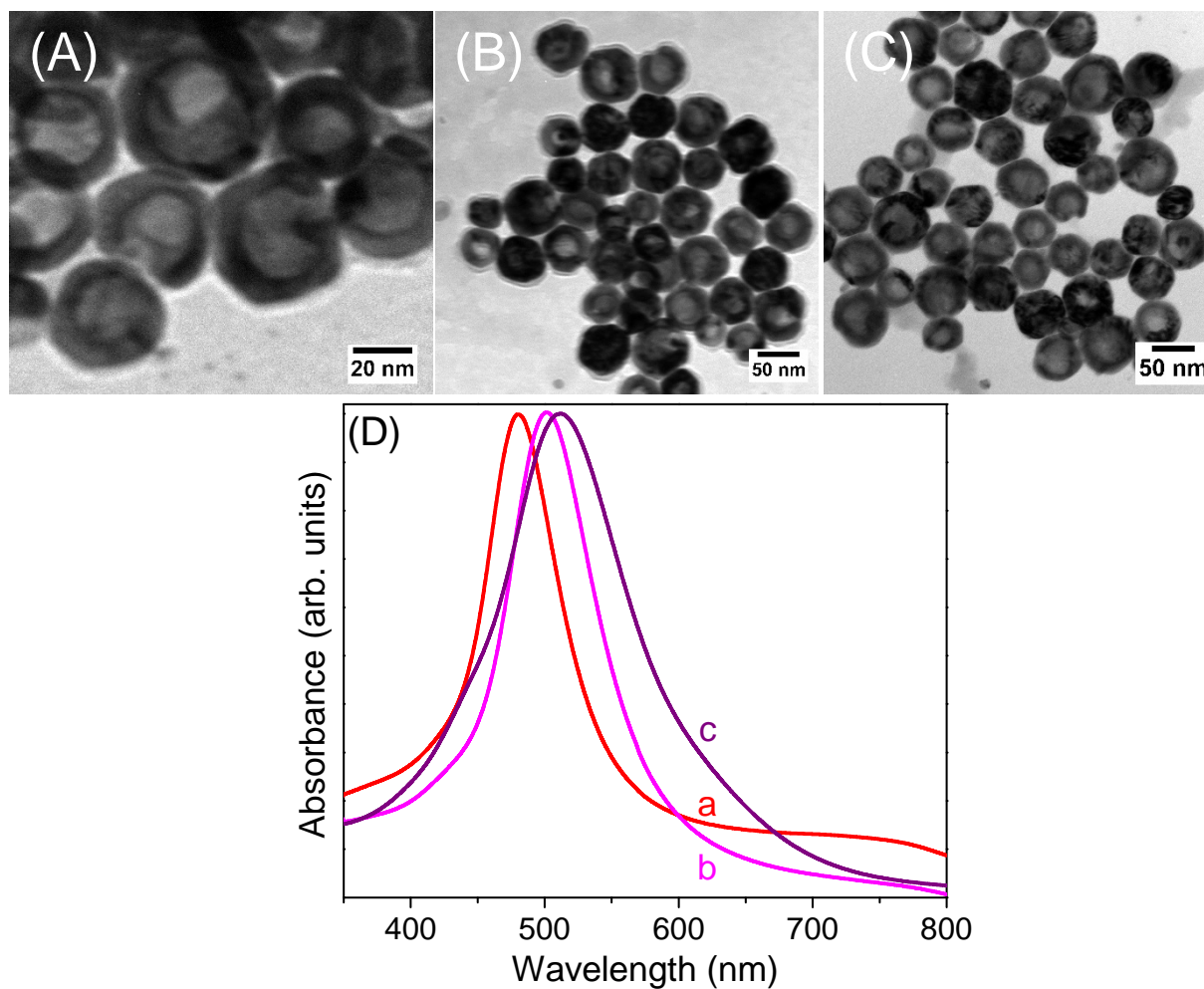


Figure 4.1: Representative TEM images of the Ag hollow NPs with average outer diameters of (A) 38.2 ± 9.1 , (B) 46.2 ± 5.4 , and (C) 55.1 ± 6.5 nm, displaying (D) surface Plasmon resonance maxima at (a) 480, (b) 500, and (c) 510 nm, respectively.

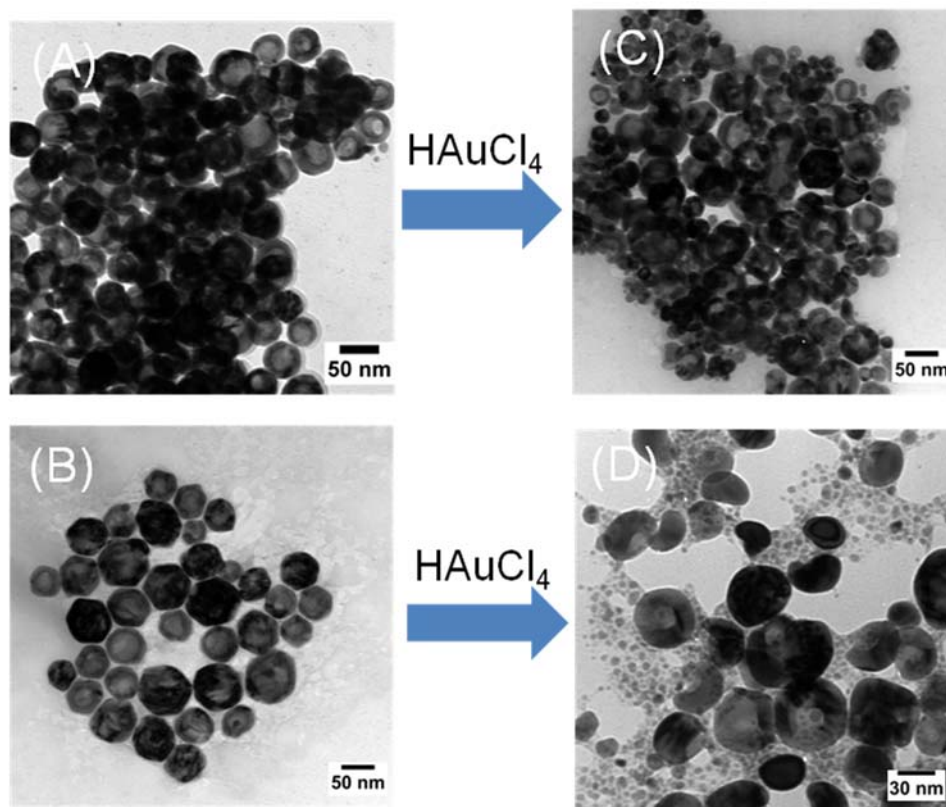


Figure 4.2: Low resolution TEM images of Au/Ag alloy NPs produced via galvanic displacement of Ag hollow NPs with (A) 38.2 ± 9.1 nm and (B) 55.1 ± 6.5 nm outer diameters and 5.8 ± 0.9 nm and 10.4 ± 1.4 nm wall thickness, respectively. TEM images of resultant Au/Ag alloy NPs are shown in (C) and (D), respectively.

The optical properties of Au and Ag NPs are governed by the morphology and composition. It has been reported that SPR of the Au¹⁰³ and Ag¹⁵⁷ hollow NPs can be tuned over a wide spectral region (550-820 and 480-570 nm, respectively) by varying the outer diameter and wall thickness. Similarly, the Au/Ag alloy NPs exhibit composition dependent plasmonic absorption in the visible spectrum.¹⁶² Therefore, we have systematically studied the morphological and optical evolution of Au/Ag alloy nanostructures as a function of the molar ratio of Au: Ag (m value) employed in the GRRs. In this study, alloy NPs were produced starting with $m = 0.14$ and the

physical properties were investigated up to $m = 0.72$ (Figure 4.3). It was revealed that the synthesis of Au/Ag hollow NPs, retaining the original morphology of Ag templates, can be achieved up to $m = 0.35$ with minimum or no alterations to outer diameter and wall thickness (Figure 4.4B and Table 4.1). The STEM-EDS elemental maps of the resultant Au/Ag hollow NPs indicate the homogeneous solid solution behavior (Figure 4.5). Notably, upon further increasing the m value ($0.35 < m < 0.56$), Au/Ag hollow NPs surface decorated with smaller Au NPs (2-5 nm) were obtained, likely due to heterogeneous nucleation of the Au^{3+} on the Au/Ag hollow NPs (Figure 4.4C).¹¹⁵ The STEM-EDS elemental maps of the reaction product indicate the presence of Au and Ag throughout the hollow structure; however the smaller NPs are appeared to be rich in Au (Figure 4.6). The number of smaller NPs increases with increasing m , likely due to increased heterogeneous nucleation. Interestingly, when m is further increased to 0.72, the template broke apart resulting in significantly smaller (3-10 nm) Au/Ag alloy NPs (Figure 4.4D and Figure 4.7). These morphological changes of alloy nanostructures are accompanied by a red shift in SPR maxima from 500-540 nm (Figure 4.8).^{27, 31, 163, 164} Therefore, the size, shape, and composition of Au/Ag hollow NPs and consequently the plasmonic absorption can be tuned by varying the morphology of hollow Ag template and/or the m value employed in the GRRs.

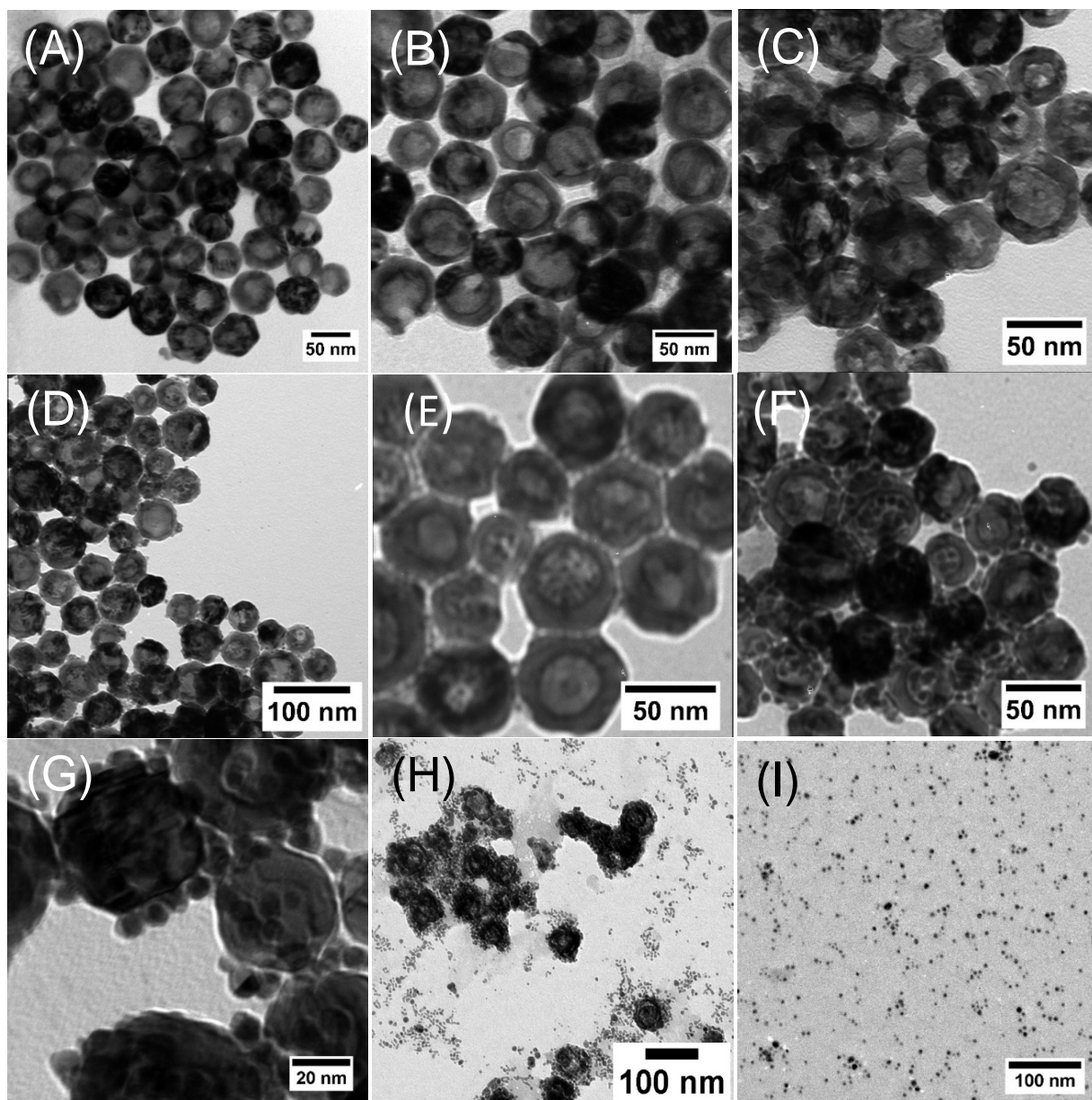


Figure 4.3: Low resolution TEM images of Au/Ag alloy NPs produced with m value of (A) 0, (B) 0.14, (C) 0.28, (D) 0.35, (E) 0.42, (F) 0.49, (G) 0.56, (H) 0.63, and (I) 0.72. The precursor Ag templates exhibit an average outer diameter of 46.2 ± 5.4 nm and wall thickness of 9.1 ± 1.2 nm. The Au/Ag hollow NPs completely break apart into significantly smaller alloy NPs when $m > 0.72$.

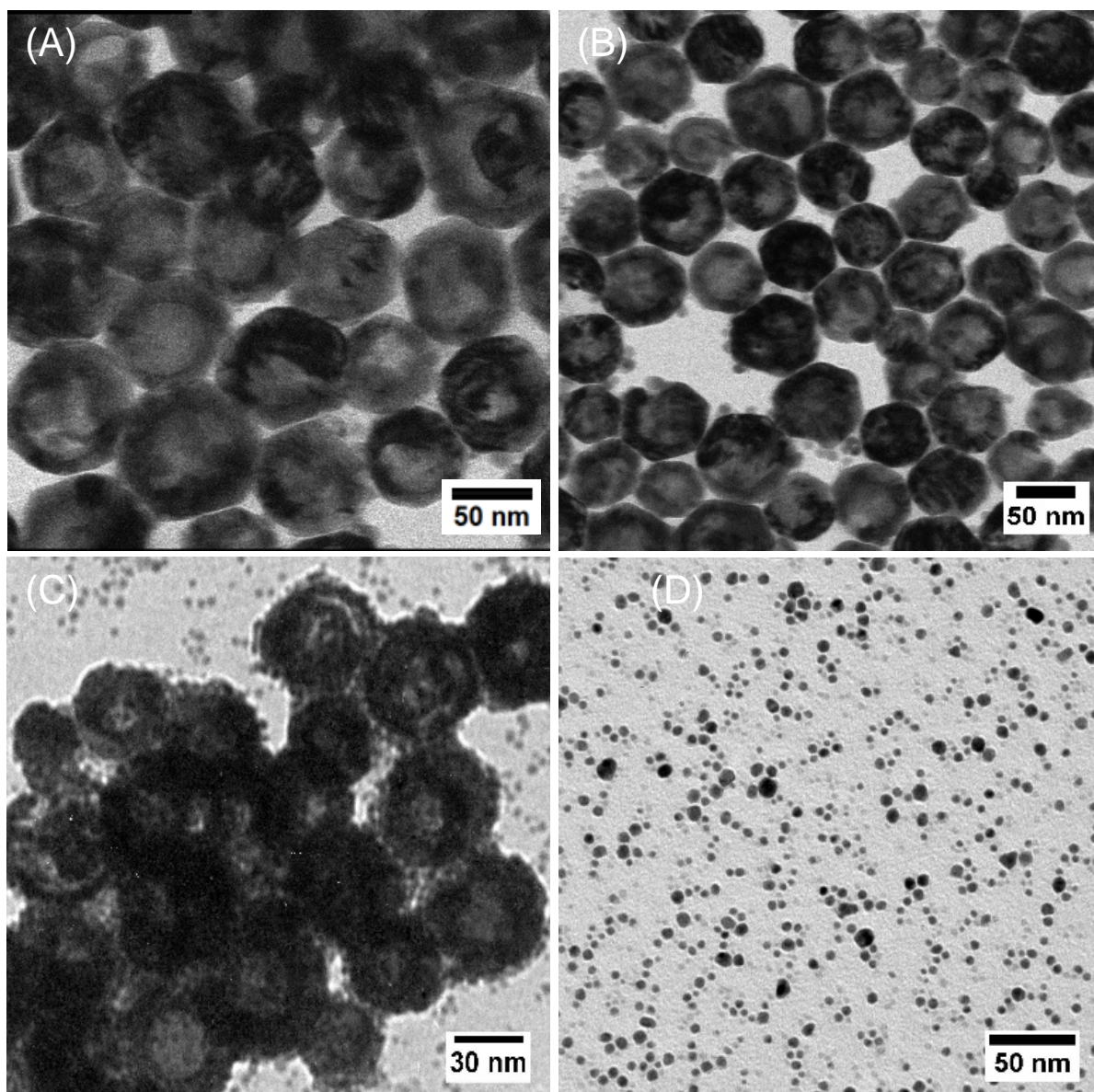


Figure 4.4: TEM images of the (A) precursor Ag hollow NPs that exhibit 46.2 ± 5.4 nm average outer diameter and 9.1 ± 1.2 nm shell thickness along with (B) Au/Ag alloy I, (C) II and (D) III produced via galvanic replacement with $m = 0.35$, 0.56 , and 0.72 , respectively.

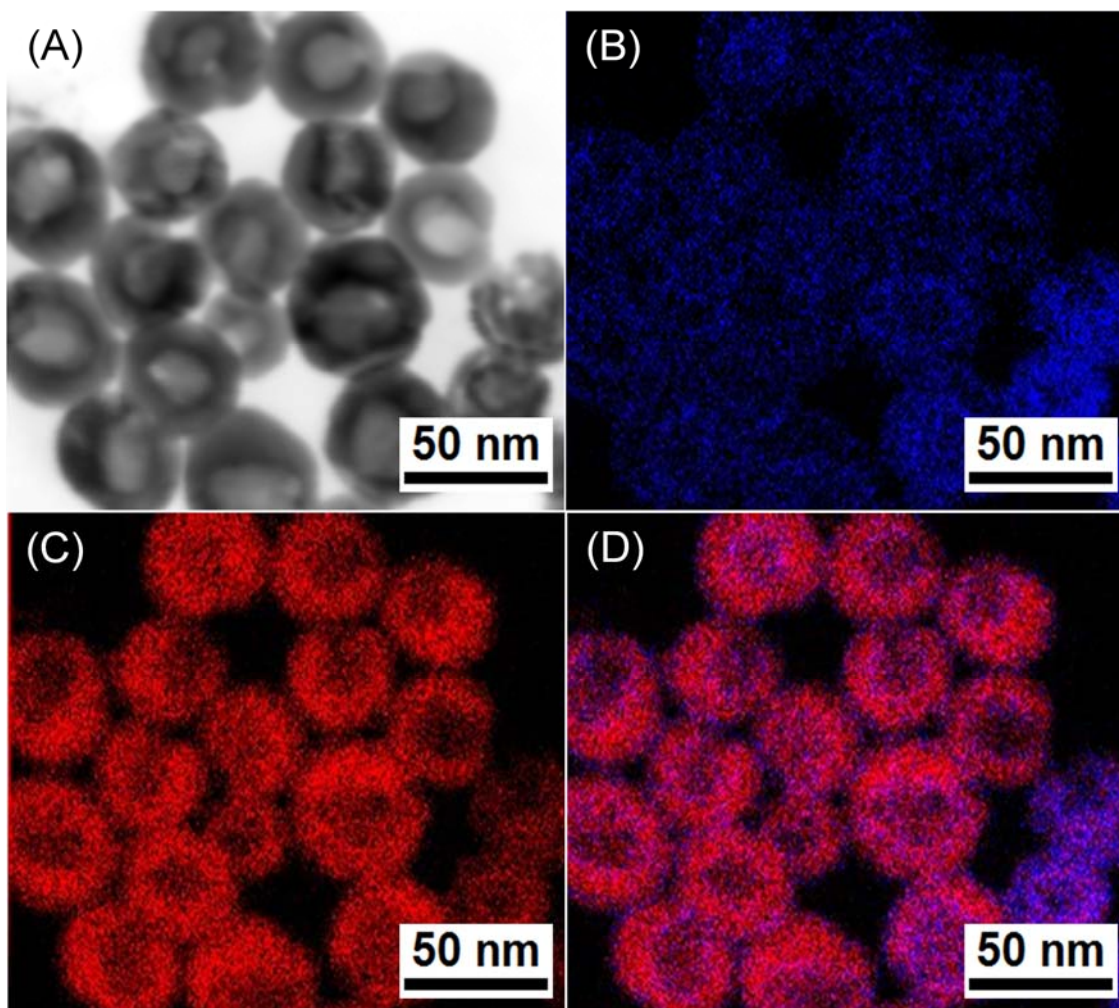


Figure 4.5: (A) TEM image of Au/Ag alloy I along with STEM-EDS elemental maps of (B) Au, (C) Ag, and (D) overlay of Au and Ag maps indicating the homogeneous distribution of elemental components throughout the nanostructure.

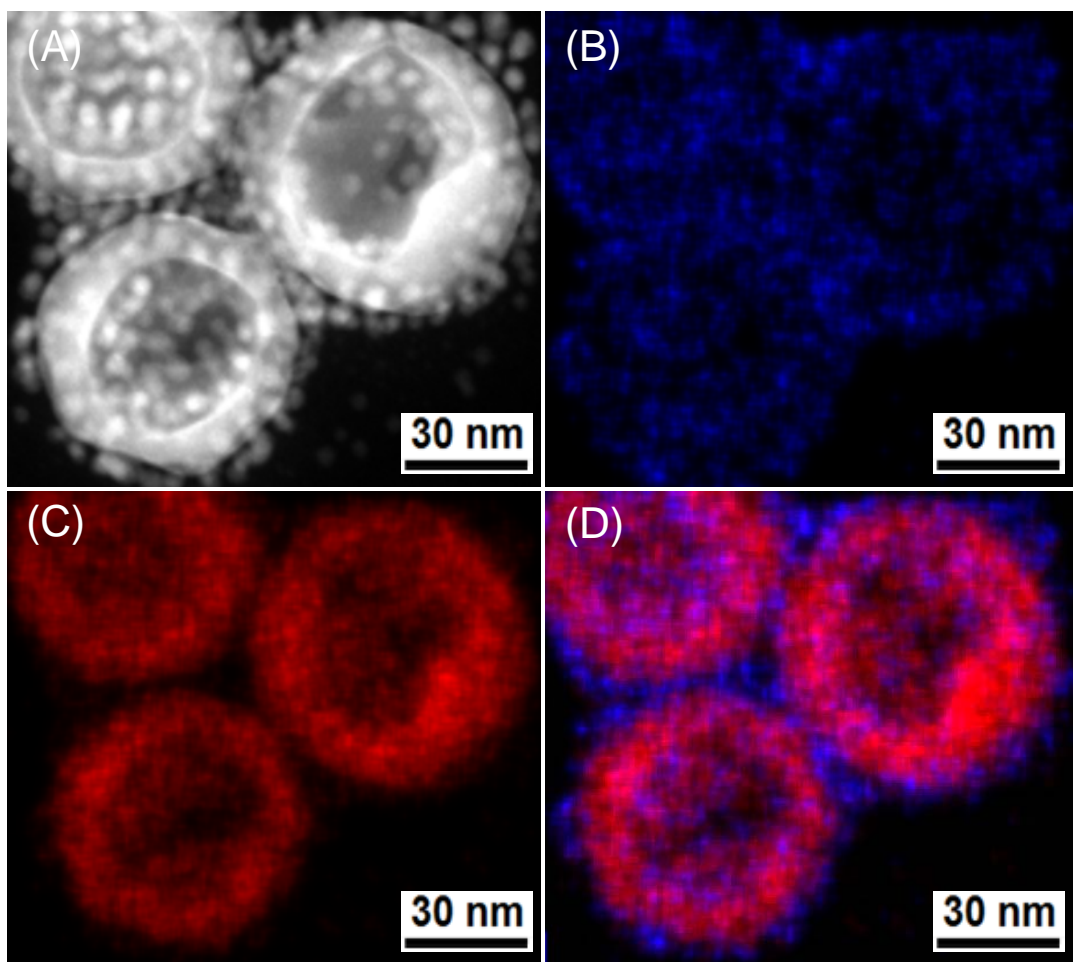


Figure 4.6: (A) STEM image of Au/Ag alloy II along with elemental maps of (B) Au, (C) Ag, and (D) overlay of Au and Ag maps indicating the homogeneous distribution of elemental components throughout the larger hollow NPs and the heterogeneous nucleation of smaller Au NPs.

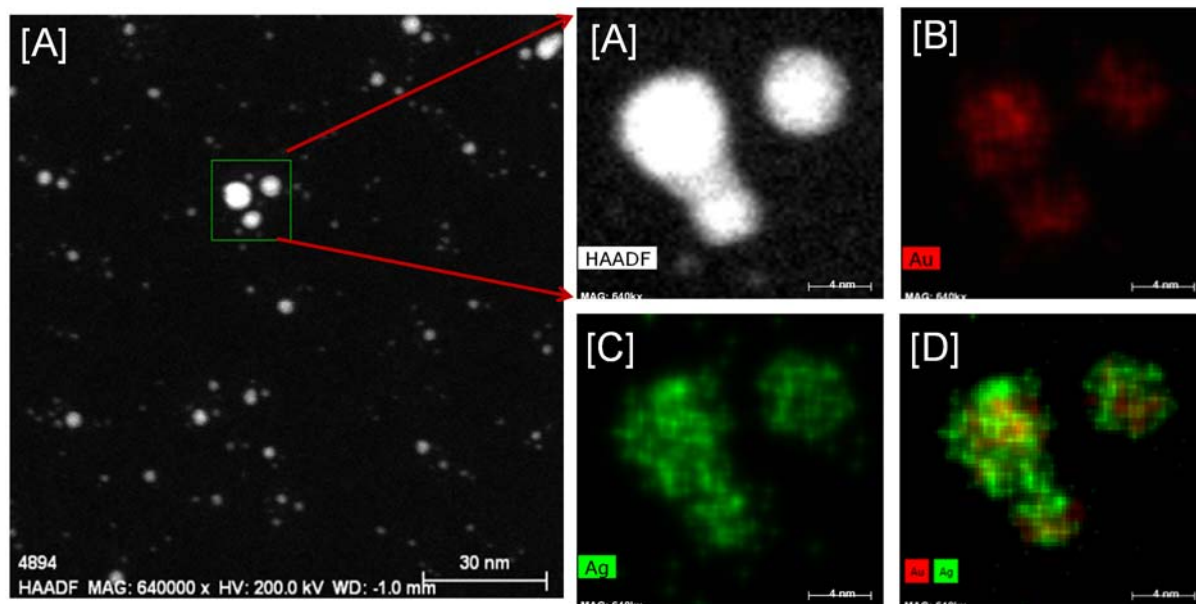


Figure 4.7: STEM-EDS elemental maps of Ag/Au alloy NP III: (A) the dark field STEM image; EDS elemental maps of (B) Au and (C) Ag with (D) overlay image of Ag and Au.

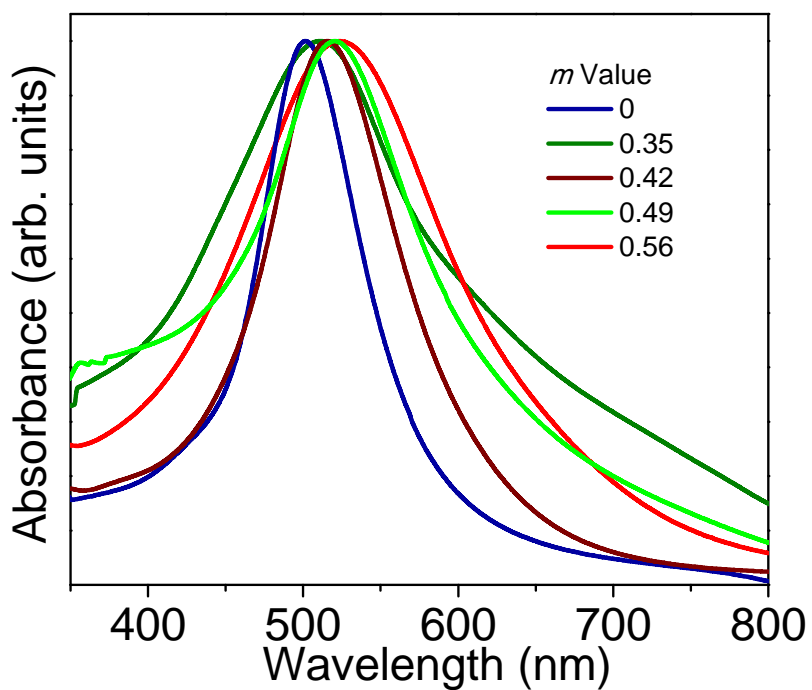
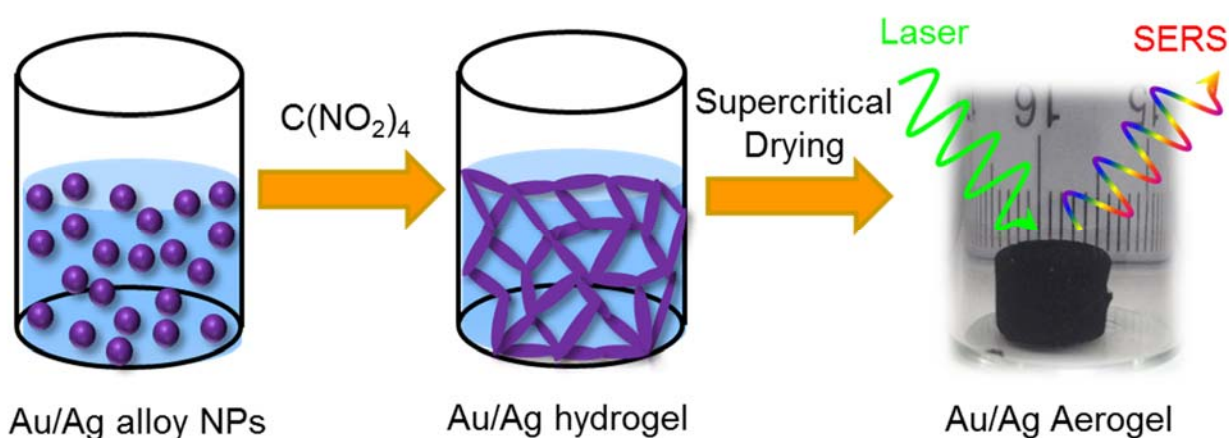


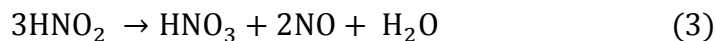
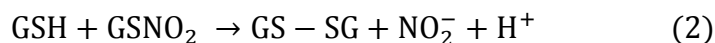
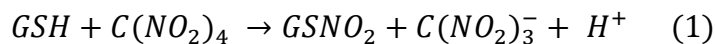
Figure 4.8: Normalized UV-Visible absorption spectra of Au/Ag alloy NPs shown in Figure 4.3 along with the corresponding m values used in the synthesis.

Au/Ag alloy NPs with three distinct morphologies were employed in the sol-gel transformation, which were designated as alloy I, II, and III produced with $m = 0.35, 0.56, 0.72$, respectively. These alloys exhibit SPR maxima at 510, 525, and 540 nm, which are red shifted from that of the precursor Ag hollow NPs (Figure 4.9). For Au/Ag alloy I, the hollow NPs retained the spherical shape and the shell thickness is uniformly distributed around the hollow interior (Figure 4.4B). This suggests that the oxidation of Ag template initiated uniformly over the entire shell of the particle. However, a significant increase in full width at half maximum (FWHM = 112 nm) due to changes in the composition is noted, which is consistent with previous reports on Au/Ag alloy NPs.^{165, 166} For Au/Ag alloy II, the smaller Au NPs, decorated on the larger hollow NPs, caused a further red shift in plasmonic maximum to 525 nm and a slight increase in broadness (FWHM = 147 nm). It is possible that the smaller NPs decorated on the surface act as plasmonic antenna resulting in broadening of the SPR.^{167,168} For Au/Ag alloy III, hollow Ag templates completely broke apart into smaller, polydisperse, and asymmetrical NPs. The subsequent SPR maximum is 540 nm and the FWHM has increased to 178 nm, which is consistent with previous reports on Au/Ag alloy nanostructures.^{31,165,169}



Scheme 4.1: A Schematic illustration of the oxidation-induced self-assembly of Au/Ag alloy NPs into monolithic aerogels for application in surface enhanced Raman scattering.

As-prepared alloy NPs were purified and concentrated by excessive washing with ultrapure water, followed by centrifuge filtration to remove ionic byproducts (Na^+ , Cl^- and BO_2^-)¹⁵⁷ of the synthesis. The gelation was induced by addition of 100 μL of 1 % $\text{C}(\text{NO}_2)_4$ to 2 mL of 10 mM Au/Ag sol. The addition of $\text{C}(\text{NO}_2)_4$ facilitates the oxidation of surface thiolate (GSH) to sulfenyl nitrates (GS-NO_2) and disulfides (GS-SG), creating low coordinated active sites on the NP surface (eqn. 1 and 2).¹⁴⁹ The formed active sites are highly reactive allowing direct interfacial linkages resulting in NP condensation to macroscopic hydrogels (Scheme 1 and Figure 4.9).¹⁷⁰ Upon gelation, the hydrogels were loaded into microporous capsules and dried with supercritical CO_2 to produce Au/Ag alloy aerogels. The resultant aerogels appear black and exhibit ~5-10% volume loss compared to precursor hydrogels. The reason for this remarkable contrast in color as opposed to those of bulk alloys is that the Au/Ag NPs in the aerogels are still acting as individual entities despite being directly cross-linked into fractal networks. In these individually acting building blocks, the superposition of the SPR is likely responsible for the black color. Accordingly, Au/Ag aerogels exhibit continuous absorption in the visible spectrum (Figure 4.10). The densities of as-prepared alloy aerogels are 0.051-0.055 g/cm^3 , representing ~0.5% of those of the corresponding Au/Ag bulk alloys (11.5-13.6 g/cm^3).



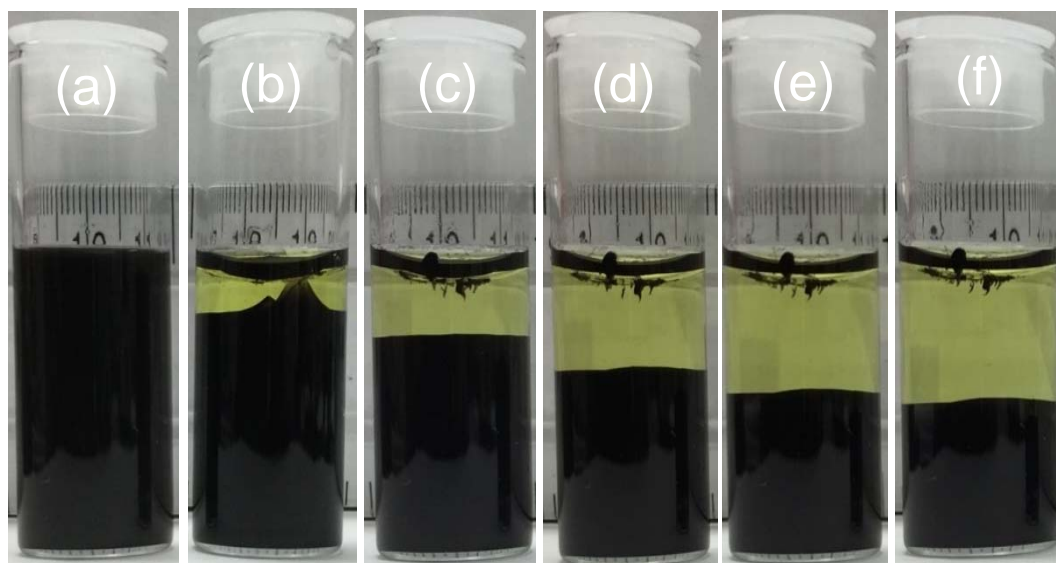


Figure 4.9: Photographs illustrating the transformation of Au/Ag NP sol into a hydrogel as a function of time: (a) concentrated Au/Ag sol, (b) hydrogel produced 2 h after oxidation of surface thiolates, along with the gel aged for (c) 3 h, (d) 4 h, (e) 5 h, and (f) 6 h.

Table 4.1 Crystallite Sizes, Wall Thicknesses, Particle Sizes, Elemental Compositions, and Wavelengths of the SPR Maxima of Au/Ag Alloy NPs along with the Densities, Surface Areas, Average Pore Diameters and Cumulative Pore Volumes of Au/Ag Alloy Aerogels produced via Oxidation-Induced Self-Assembly.

Sample	Precursor NPs				Au/Ag Aerogels		
	Ag Hollow NPs	Au/Ag Alloy I	Au/Ag Alloy II	Au/Ag Alloy III	Aerogel I	Aerogel II	Aerogel III
Crystallite size (nm) ^a	19.0 ± 0.2	17.8 ± 0.2	14.5 ± 0.2	16.72 ± 0.2	11.1 ± 0.2	4.5 ± 0.2	4.2 ± 0.2
Wall thickness (nm) ^b	9.1 ± 1.2	8.9 ± 1.8	8.7 ± 1.1	N/A	5.9 ± 1.2	6.7 ± 1.5	N/A
Average outer diameter (nm) ^b	46.2 ± 5.4	45.1 ± 3.6	44.0 ± 5.5	6.1 ± 1.8	40.8 ± 6.1	44.5 ± 4.3	11.5 ± 3.2
Composition by SEM/EDS ^c	Ag 85.2%	Ag 53.7%	Ag 53.5%	Ag 46.7%	Ag 41.4%	Ag 41.6%	Ag 46.6%
	S 14.8%	Au 30.4%	Au 32.3%	Au 41.1%	Au 53.5%	Au 53.7%	Au 49.5%
		S 15.9%	S 14.2%	S 12.2%	S 5.1%	S 4.7%	S 3.9%
ICP-MS ^{c,d}		Ag 60.8%	Ag 63.5%	Ag 64.8%	Ag 44.2%	Ag 37.4%	Ag 48.3%
		Au 39.2%	Au 36.5%	Au 35.2%	Au 55.8%	Au 62.6%	Au 51.7%
SPR maxima (nm)	500	510	525	565	N/A	N/A	N/A
Density (g/cm ³)	N/A	N/A	N/A	N/A	0.051	0.055	0.052
Surface area (m ² /g) ^e	N/A	N/A	N/A	N/A	67	71	73
Molar surface area (m ² /mol) ^f	N/A	N/A	N/A	N/A	10.59 x 10 ³	11.22 x 10 ³	11.17 x 10 ³
Average pore width (nm) ^e	N/A	N/A	N/A	N/A	14.8	14.7	15.5
Cumulative pore volumes (cm ³ /g) ^e	N/A	N/A	N/A	N/A	0.29	0.31	0.34

^aCrystallite sizes were calculated by applying the Scherrer equation to (111), (220), (311) reflections of the PXRD patterns. ^bAverage wall thicknesses and outer diameters were obtained

by TEM analysis of 120-150 NPs per each sample and from 3-5 individually prepared samples. ^cElemental compositions were obtained via multiple analysis of individually prepared samples and the average values are presented. ^dAtomic percentages of Au and Ag were obtained by ICP-MS analysis with an average of 3-5 individual measurements. ^eSurface areas were computed by fitting the BET model to nitrogen adsorption/desorption isotherms whereas the average pore diameters and cumulative pore volumes were computed by applying the BJH model. ^fMolar surface areas were computed using molar mass of the alloy aerogels on the basis of atomic composition.

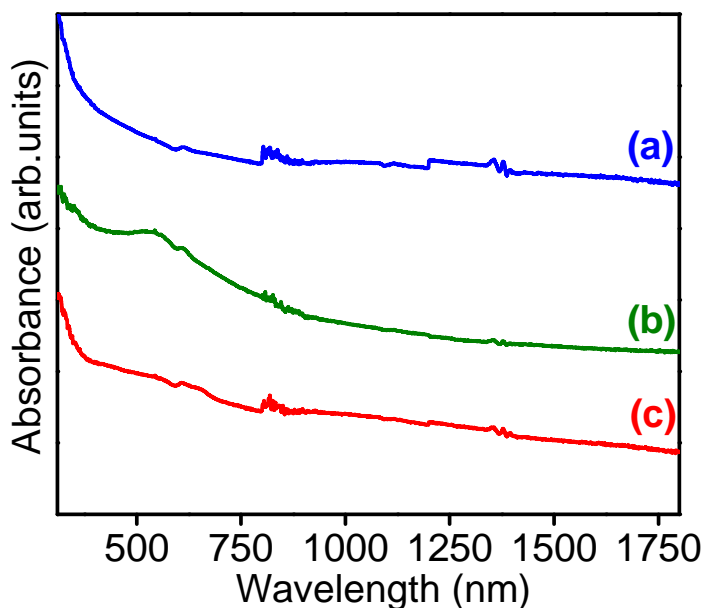


Figure 4.10: Solid state absorption spectra of Au/Ag aerogel (a) I, (b) II, and (c) III.

Low resolution TEM was employed to study the morphology of Au/Ag alloy aerogels (Figure 4.11). The aerogel I consists of an interconnected network of hollow NPs that exhibit similar dimensions to precursor NPs suggesting the retention of original morphology, upon sol-

gel assembly (Figure 4.11 and Figure 4.12). However, a number of smaller NPs were also observed (< 5 %) likely due to breakup of the larger hollow NPs. A significant reduction in outer diameter and wall thickness is noted upon oxidative removal of surface thiolates owing to dealloying of Ag by in-situ generated $\text{HNO}_2/\text{HNO}_3$ acids (Table 4.1).¹⁵⁷ In contrast, the TEM images of alloy aerogels II exhibit a vastly different superstructure. It was revealed that the in-situ generated acids can breakup the larger hollow NPs into smaller alloy NPs that undergo direct cross-linking to produce a nanoparticulate gel framework (Figure 4.11 and Figure 4.13). Interestingly, a large number of unbroken hollow NPs are randomly distributed throughout the nanoparticulate gel matrix. Conversely, the TEM images of aerogel III indicate a highly branched wire-like morphology with typical thickness of 11.5 ± 3.2 nm (Figure 4.11 and Figure 4.14). This nanostructure does not exhibit individual NPs well separated from each other but rather a complex fused assembly (Figure 4.11F). A similar morphology is reported for Au-Ag and Pt-Ag heterogeneous NP based aerogels produced via chemical oxidation of the citrate stabilized Au, Ag, and Pt NPs.^{91,171} Despite significant differences in gel morphology, the TEM images of the alloy aerogels indicate the highly porous nature of the materials, consisting of a large number of mesopores (2–50 nm) and macropores (>50 nm) throughout the superstructures (Figure 4.11 and Figure 4.15).

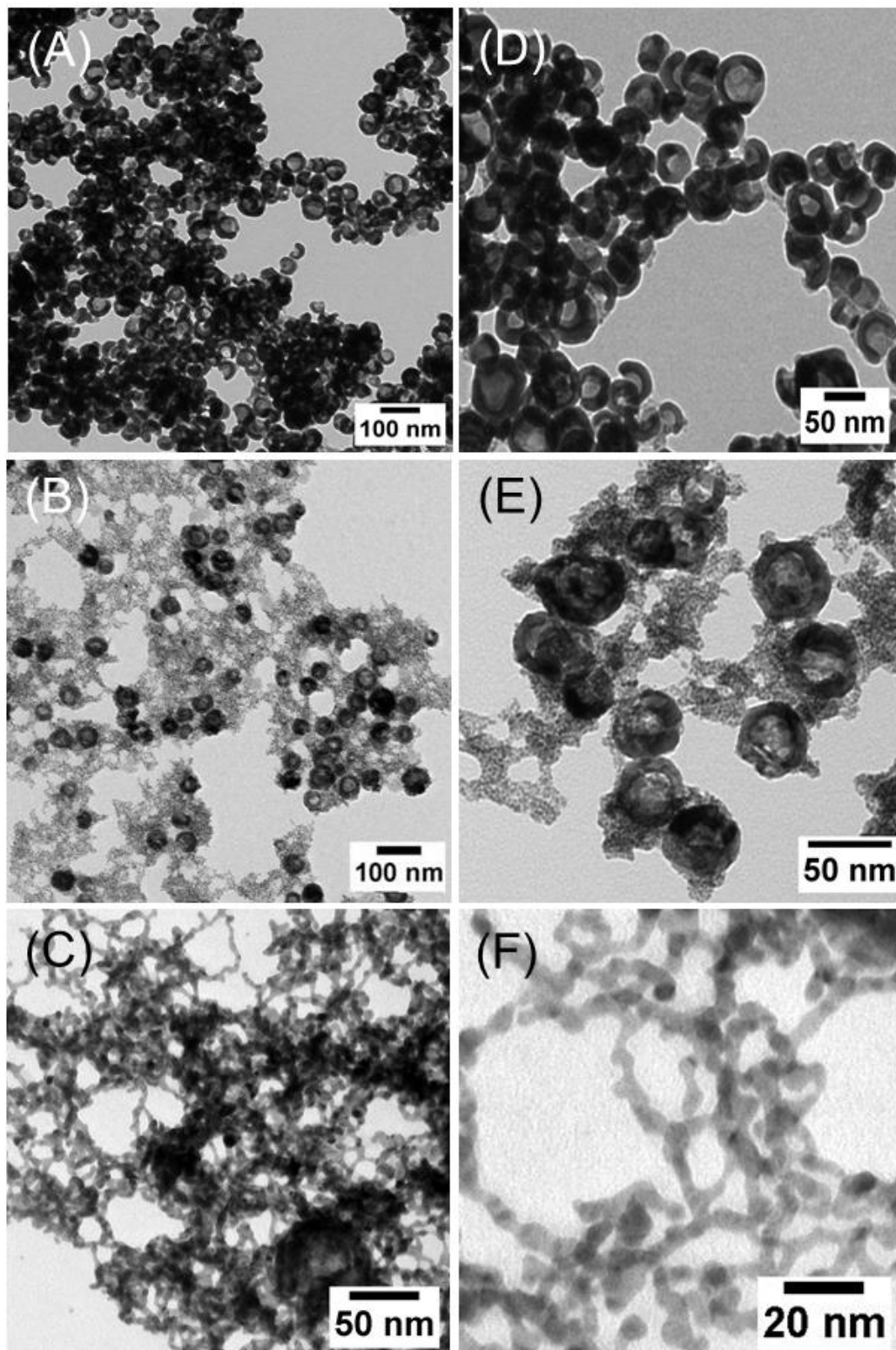


Figure 4.11: Low resolution TEM images of Au/Ag alloy aerogel (A) I, (B) II, and (C) III along with magnified electron micrographs of the aerogel (D) I, (E) II, and (F) III.

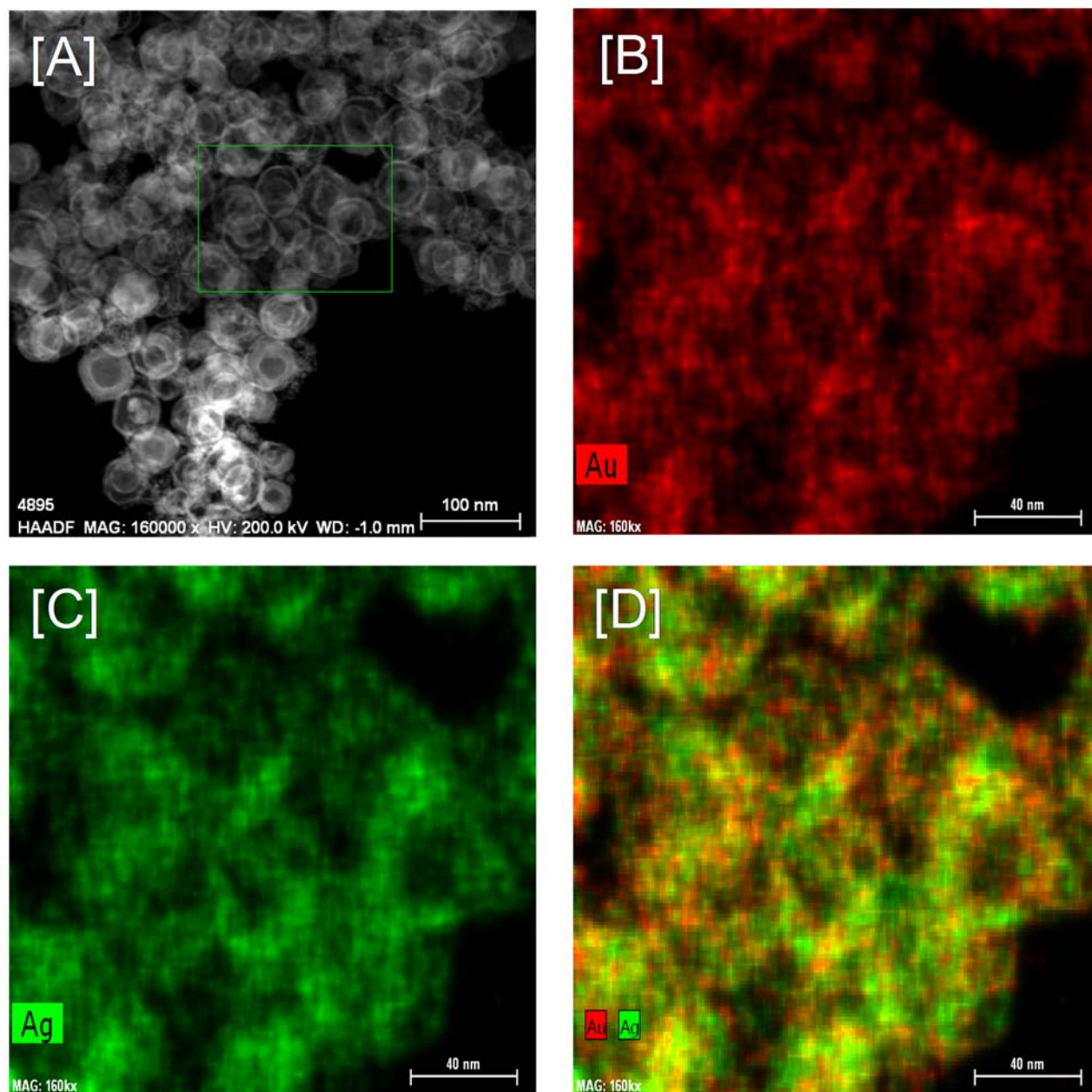


Figure 4.12: STEM-EDS elemental maps of Ag/Au alloy aerogel I: (A) the dark filed STEM image; EDS elemental maps of (B) Au and (C) Ag with (D) overlay image of Ag and Au.

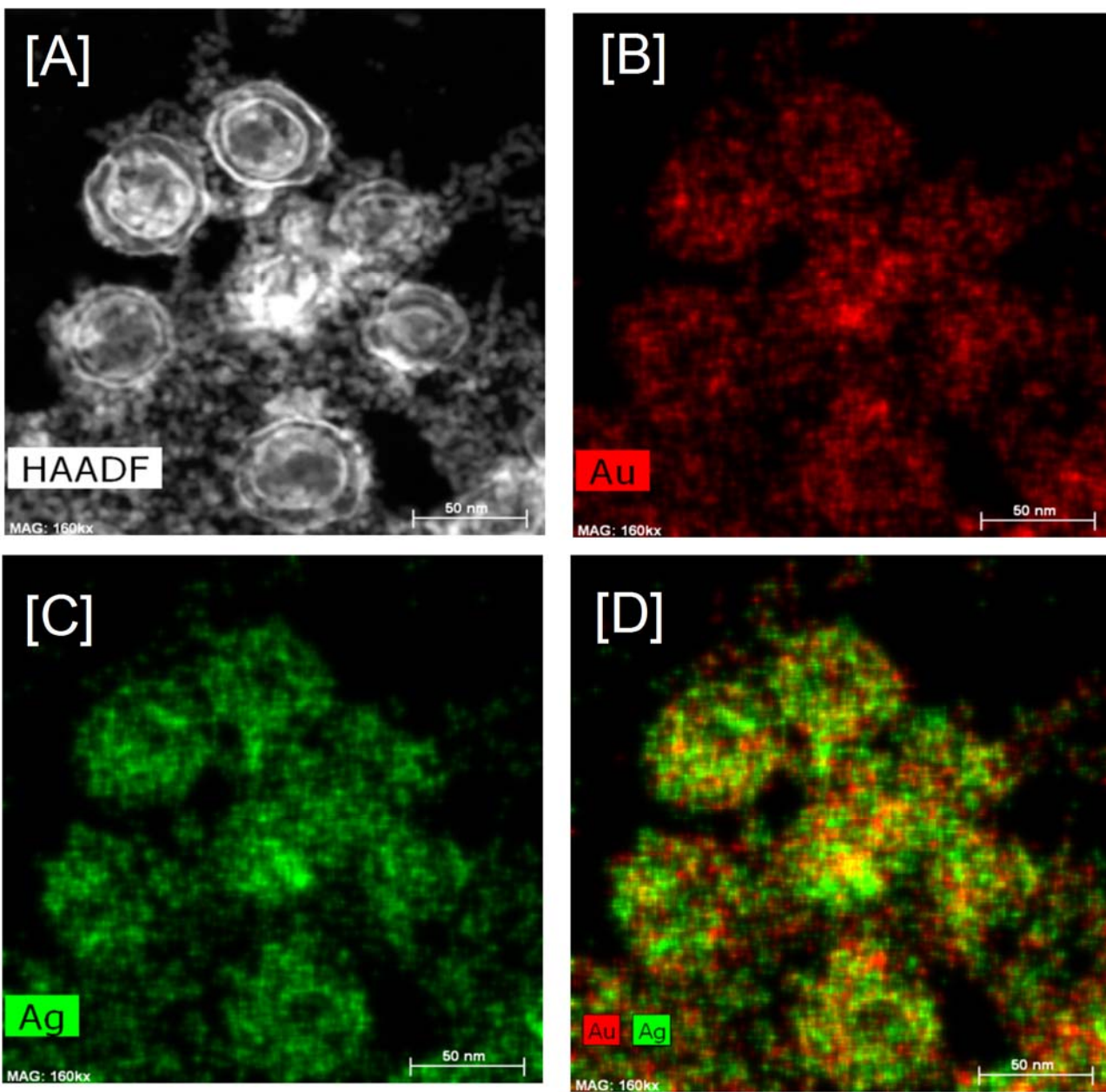


Figure 4.13: STEM-EDS elemental maps of Ag/Au alloy aerogel II: (A) the dark filed STEM image; EDS elemental maps of (B) Au and (C) Ag with (D) overlay image of Ag and Au.

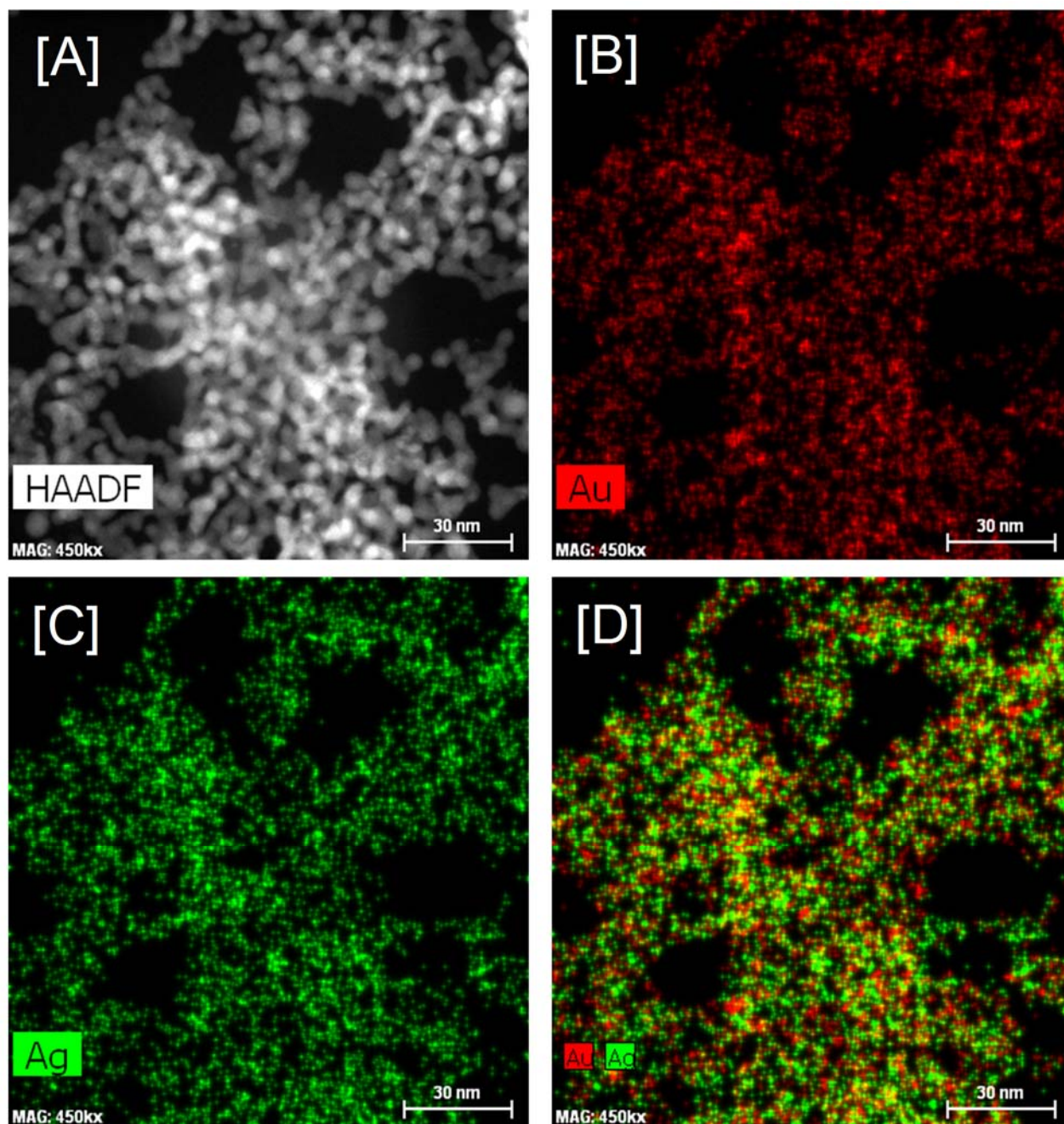


Figure 4.14: STEM-EDS elemental maps of Ag/Au alloy aerogels III: (A) the dark filed STEM image; EDS elemental maps of (B) Au and (C) Ag with (D) overlay image of Ag and Au.

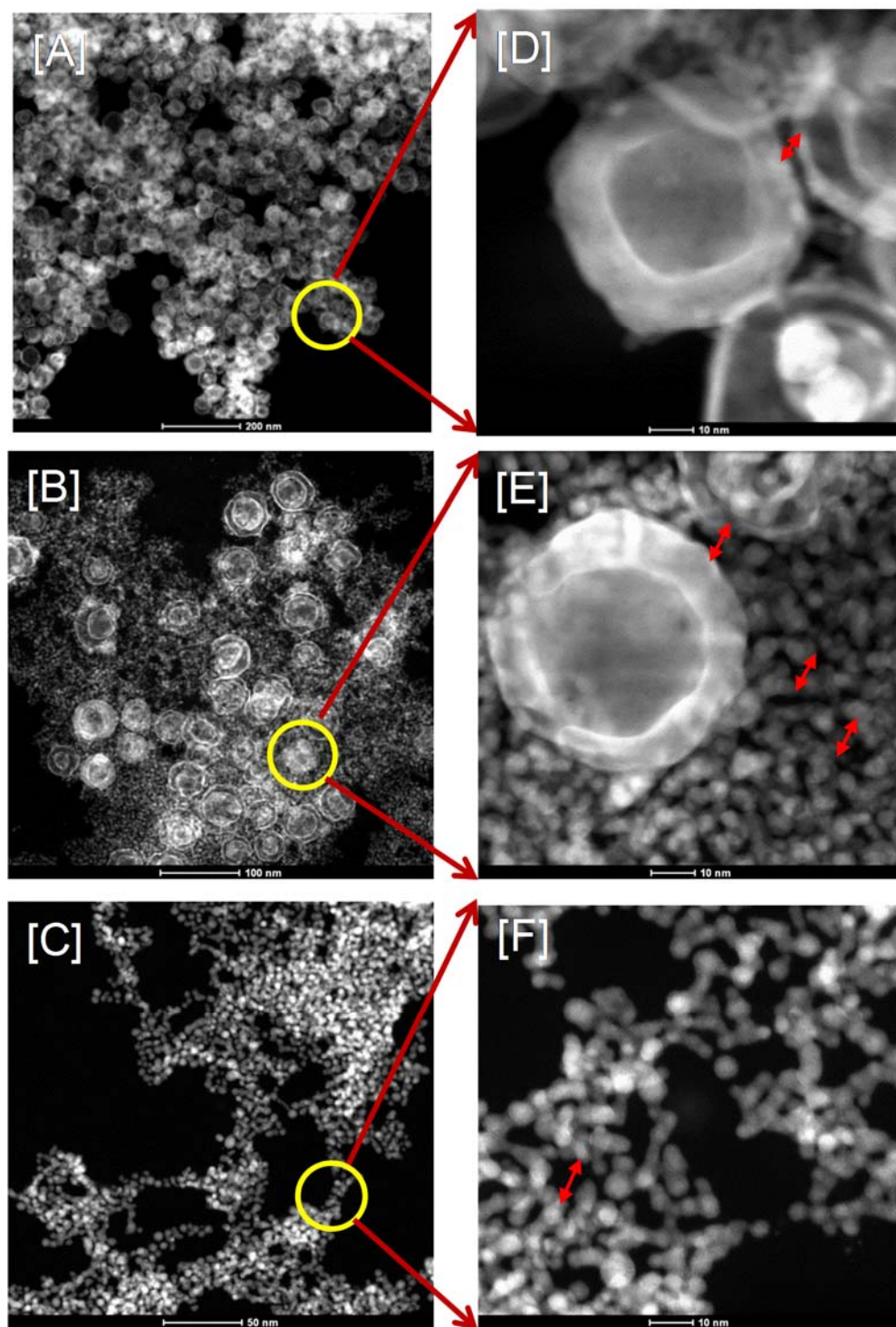


Figure 4.15: Dark field STEM images of Au/Ag aerogel [A] I, [B] II, and [C] III. The magnified STEM images [D-F] are used to demonstrate the interparticle gaps in the aerogel framework.

The powder diffraction patterns of Ag hollow NPs, Au/Ag alloy NPs, and corresponding aerogels were recorded to study the structural evolution of materials upon GRRs and oxidative-assembly. The diffraction patterns of Au/Ag precursor NPs and aerogels are consistent with the cubic Ag phase (PDF # Ag 01-0870-719) and exhibit a slight shift towards larger 2θ angles owing to the growth of homogeneous alloys (Figure 4.16). The diffraction peaks corresponding to AgCl or any other crystalline impurities were not detected suggesting that the as-synthesized materials are phase pure. The average crystallite sizes of alloy NPs and aerogels were calculated using Scherrer equation,¹⁷² which revealed values in the range of 14.5-19.0 nm for precursor NPs and 4.2-11.1 nm for aerogels (Table 4.1). In general, a significant reduction in crystallite size and wall thickness is noted upon gelation and aerogel formation, attributed to dealloying of the Ag by in-situ generated $\text{HNO}_2/\text{HNO}_3$ acids that has been previously reported to etch the Ag atoms.¹⁵⁷

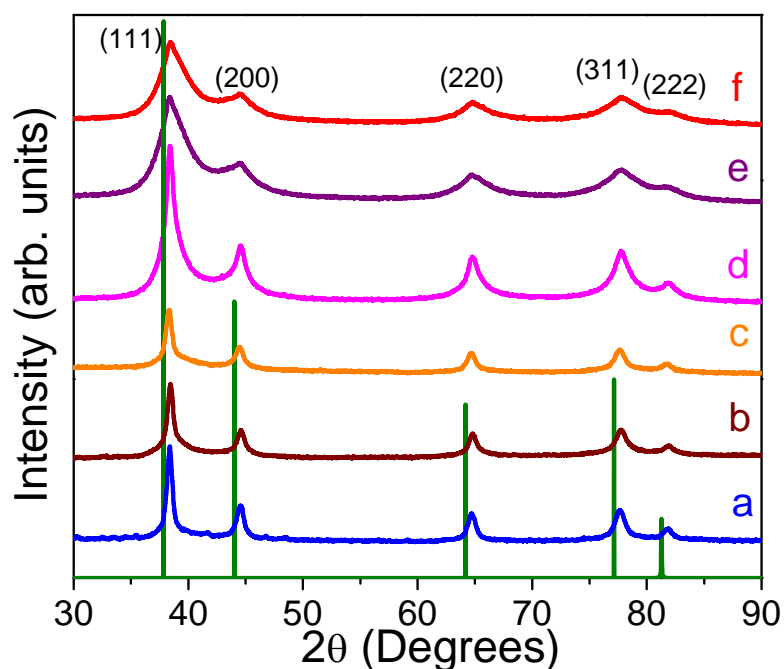


Figure 4.16. PXRD patterns of Au/Ag alloy NPs (a) I, (b) II, and (c) III along with Au/Ag alloy aerogels (d) I, (e) II, and (f) III produced via oxidation-induced self-assembly of NPs. ICDD-PDF overlay of cubic Ag (PDF # 01-0870-719) is shown as vertical lines.

Nitrogen adsorption-desorption isotherms of Au/Ag alloy aerogels were recorded to investigate the surface area and porosity of the materials. The typical isotherms of Au/Ag aerogels are shown in Figure 4.17 corresponding to type IV curves suggesting the mesoporous (2-50 nm) nature of the superstructures.^{143,144} The sharp upturn in the high-relative-pressure region is consistent with a type II curve indicating some degree of macroporosity (>50 nm) in the gel materials. The shapes of hysteresis loops reveal a combination of H1 and H3 character,¹⁴⁴ indicating that both slit-shaped and cylindrical-shaped pores are present in the gel material. The BET modeled surface areas determined from adsorption/desorption isotherms are 67, 71, and 73 m²/g for Au/Ag alloy aerogel I, II, and III, respectively. An interesting observation is that similar surface areas were obtained for aerogels assembled from larger hollow NPs (aerogel I, 40.8 ± 6.1 nm) and smaller solid NPs (aerogel III, 11.5 ± 3.2 nm). Such comparable surfaces were achieved due to accessibility of molecules to both inner and outer surfaces of the hollow NPs in aerogel I, which maximizes the available surface.^{112,157} The surface areas obtained for Au/Ag alloy aerogels I through III are considerably higher than previous reports on Au/Ag aerogels (~42 m²/g)¹¹² produced via salt mediated self-assembly and Au-Ag heterogeneous nanoparticulate aerogels (~48 m²/g),⁹¹ suggesting significant potential in chemical sensor and catalytic technologies.

The pore size distributions and cumulative pore volumes of Au/Ag alloy aerogels were investigated by applying the BJH model to the desorption branches of N₂ adsorption/desorption isotherms. Interestingly, a bi-modal pore distribution plot was achieved for alloy aerogel I: a narrow distribution centered at ~8 nm and a broader distribution centered at ~30 nm. In contrast, the precursor NPs I exhibit a single pore distribution at ~7 nm, corresponding to inner diameter of the hollow NPs (4.18). Therefore, the narrow pore distribution at ~8 nm is likely originated

from hollow interior of the alloy NP I that retains its morphology, suggesting that small molecules can penetrate through nanoshells into hollow interior of the particles. The latter distribution centered at ~ 30 nm corresponds to meso-to-macro pore network buildup by the 3-dimensional gel framework, which is clearly observed in TEM images (Figure 4.11). On the contrary, aerogels II and III exhibit unimodal pore size distributions reminiscent of network pores, suggesting the presence of minimum (aerogel II) or no (aerogels III) hollow NPs in corresponding superstructures. Collectively, the surface area and pore size distribution analyses revealed the perforated nature of the larger hollow NPs, making them of great interest for customized chemical sensor and catalytic applications.

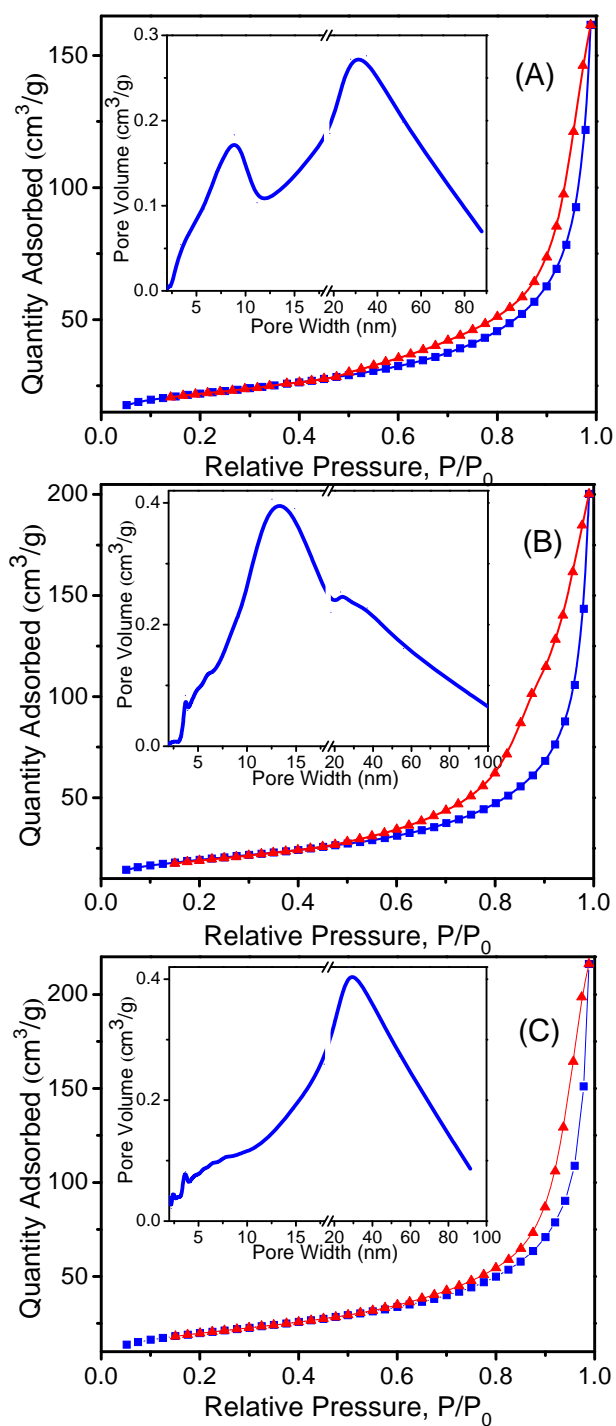


Figure 4.17: Nitrogen adsorption (blue) desorption (red) isotherms of Au/Ag alloy aerogel (A) I, (B) II, and (C) III. The corresponding BJH model pore distribution plots are shown as insets.

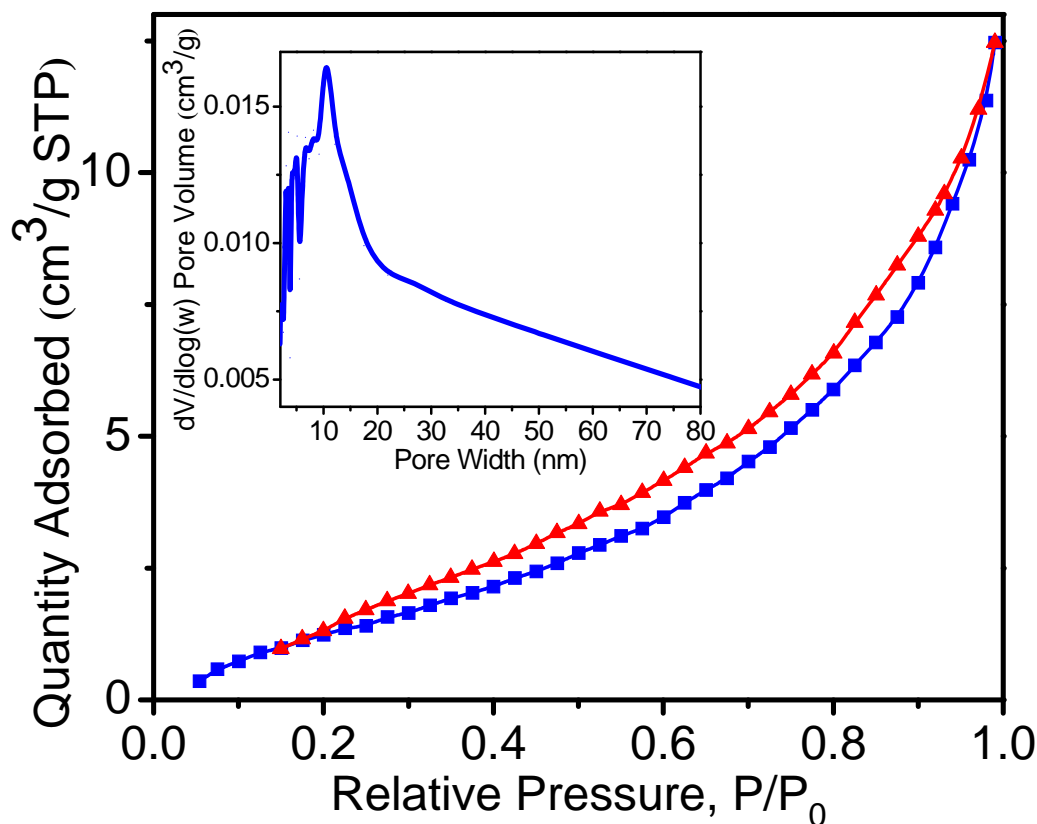


Figure 4.18: Nitrogen adsorption/desorption isotherm of Au/Ag alloy NP I along with the corresponding BJH modeled pore size distribution plot (Inset). BET surface area = 7.13 m²/g, average pore diameter = 7.5 nm, and cumulative pore volume = 0.018 cm³/g.

The SERS properties of Au/Ag aerogels were investigated by employing Rd 101 as a probe molecule. The SERS spectra of Rd 101 (1 μM) in the presence of Au/Ag alloy NPs and corresponding aerogels are shown in Figure 4.19. The strong to medium Raman bands observed at 1229, 1347, 1504, and 1645 cm⁻¹ are assigned to the C-O-C stretch, C-H scissoring, C-N stretch, and xanthene ring stretch of Rd 101, respectively.¹⁷³ It has been reported that Ag NPs are promising SERS substrates whereas Au and Au/Ag alloy NPs tend to exhibit much lower signal enhancement partly due to the differences in plasmonic properties.^{174, 175} In the current study, we

compare the structural properties of the Au/Ag alloy NPs and aerogels to better understand the effects of oxidative self-assembly and mesoporous gel morphology on SERS properties. The NP measurements were done by mixing Rd 101 into concentrated colloidal sols and placing a drop on an aluminum pan to dry or by drop casting the dye solutions onto dried NP precipitates. Both sample preparation methods resulted in similar signal intensities. During a typical measurement average signal intensities of 47.5 ± 6.4 , 59.0 ± 29.3 , and 57.8 ± 18.8 were attained at 1645 cm^{-1} for NP I, II, and III, respectively. In contrast, no signal was acquired from $1\text{ }\mu\text{M}$ Rd 101 drop casted on Al substrates (Figure 4.20). The aerogel samples were dispersed in solutions of Rd 101 ($1\text{ }\mu\text{M}$ - 1 nM) and placed on an aluminum pan to dry, prior to signal acquisition. The average signal intensities attained for Au/Ag alloy aerogels I, II and III are 946.2 ± 395.7 , 2231.3 ± 1079.7 , and 474.7 ± 203.3 , respectively for the peak at 1645 cm^{-1} .^{176,177} The intensity histograms at 1504 cm^{-1} and 1645 cm^{-1} obtained from different locations of multiple individually prepared samples are shown in Figure 4.21. This data suggest that the mesoporous gel morphology plays a clear role in improving the signal over that of the dried NP precipitates. There are two possible factors for the observed improvements in signal intensity. First, the amount of plasmonic particles hit by the laser during a given scan can vary drastically when comparing a relatively flat precipitate of NPs vs. the rough surface of the aerogels. The aerogel materials are known to exhibit more hills and valleys in the nanoscale in comparison to condensed NP precipitates.^{112,157} Second, the aerogels exhibit interparticle crevices that can potentially generate a large number of plasmonic hot spots leading to higher signal enhancement. In general, the aerogel II exhibits signal intensities that are 2-5 times higher than aerogel I and III owing to more interparticle gaps observed in a mixed gel framework (Figure 4.15). The large standard deviations attained for SERS intensities are likely due to the inherent randomness of the non-ordered superstructures.

However, an optimized aerogel III demonstrates signal enhancement down to 1 nM level whereas a significant reduction in signal intensity is observed from 1 nM to 1 pM level. Further studies, beyond the scope of this work, are underway to improve the microstructural properties of aerogels to achieve better signal enhancement and improved sensitivity of molecular detection.

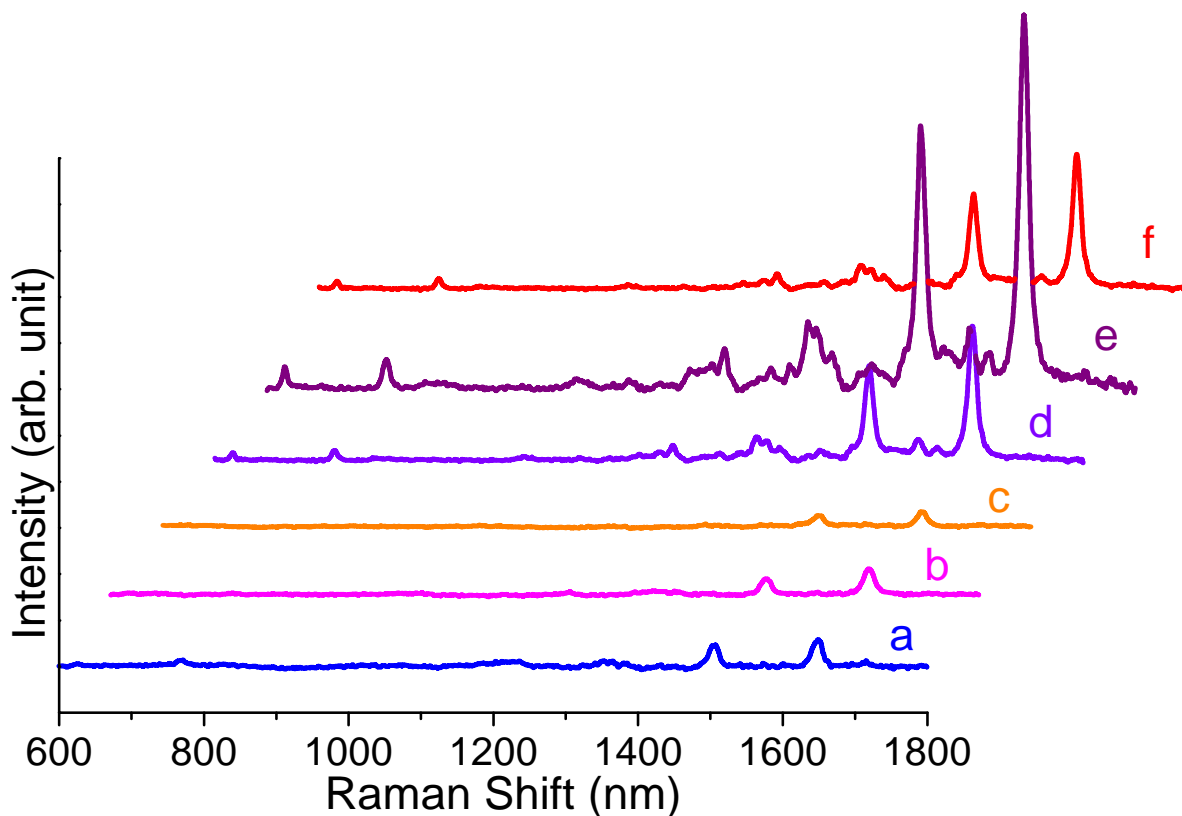


Figure 4.19: Surface enhanced Raman scattering spectra of Au/Ag alloy NP (a) I, (b) II, and (c) III along with corresponding Au/Ag alloy aerogel (d) I, (e) II, and (f) III. For better representation, the SERS spectra of Au/Ag alloy NPs (I-III) were multiplied by a common factor of two.

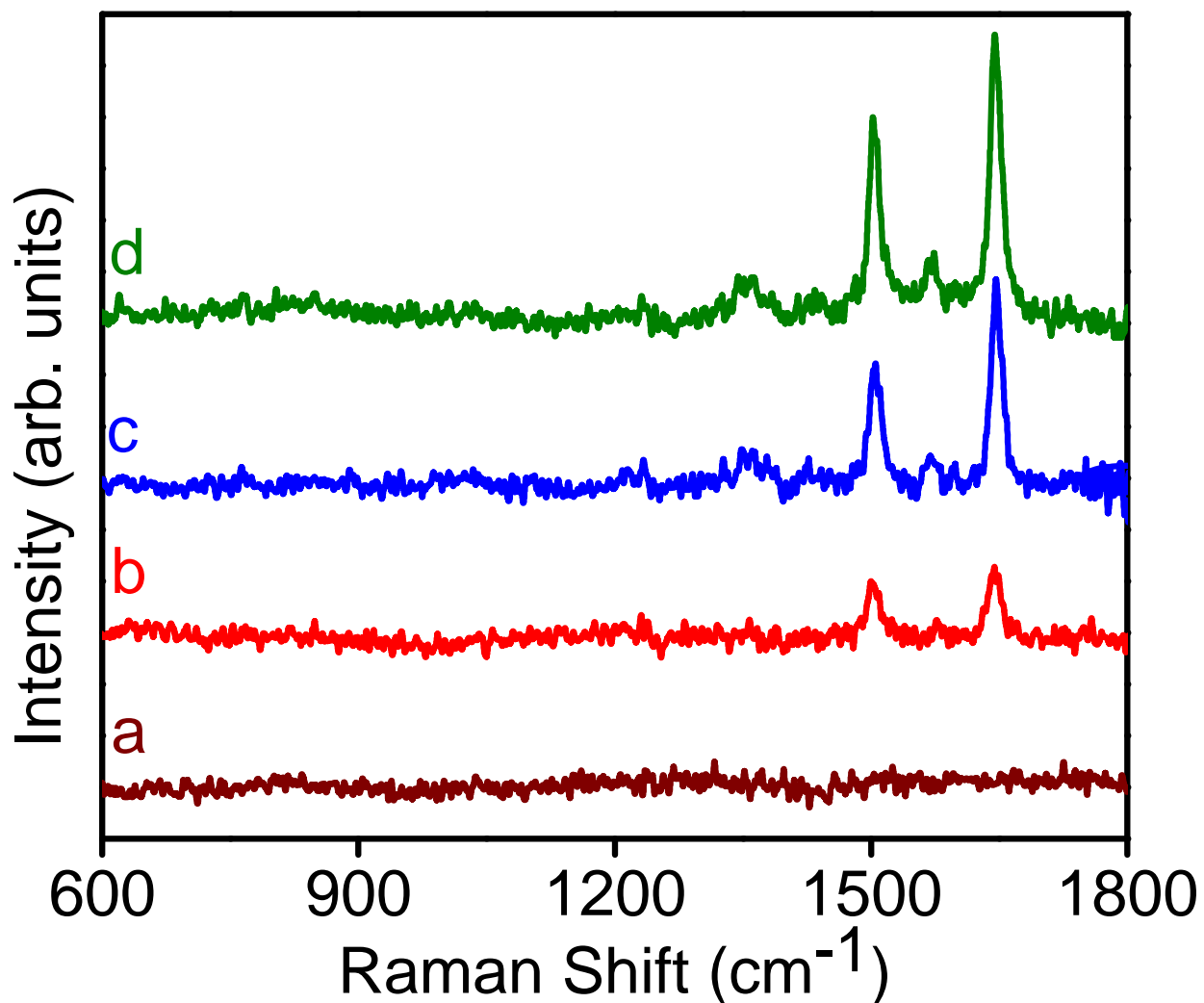


Figure 4.20 Raman spectra of (a) Rd 101 ($1 \times 10^{-6} \text{ M}$) with no SERS substrate. Au/Ag aerogel III with different concentrations of Rd 101: (b) $1 \times 10^{-9} \text{ M}$, (c) $1 \times 10^{-7} \text{ M}$, (d) $1 \times 10^{-6} \text{ M}$.

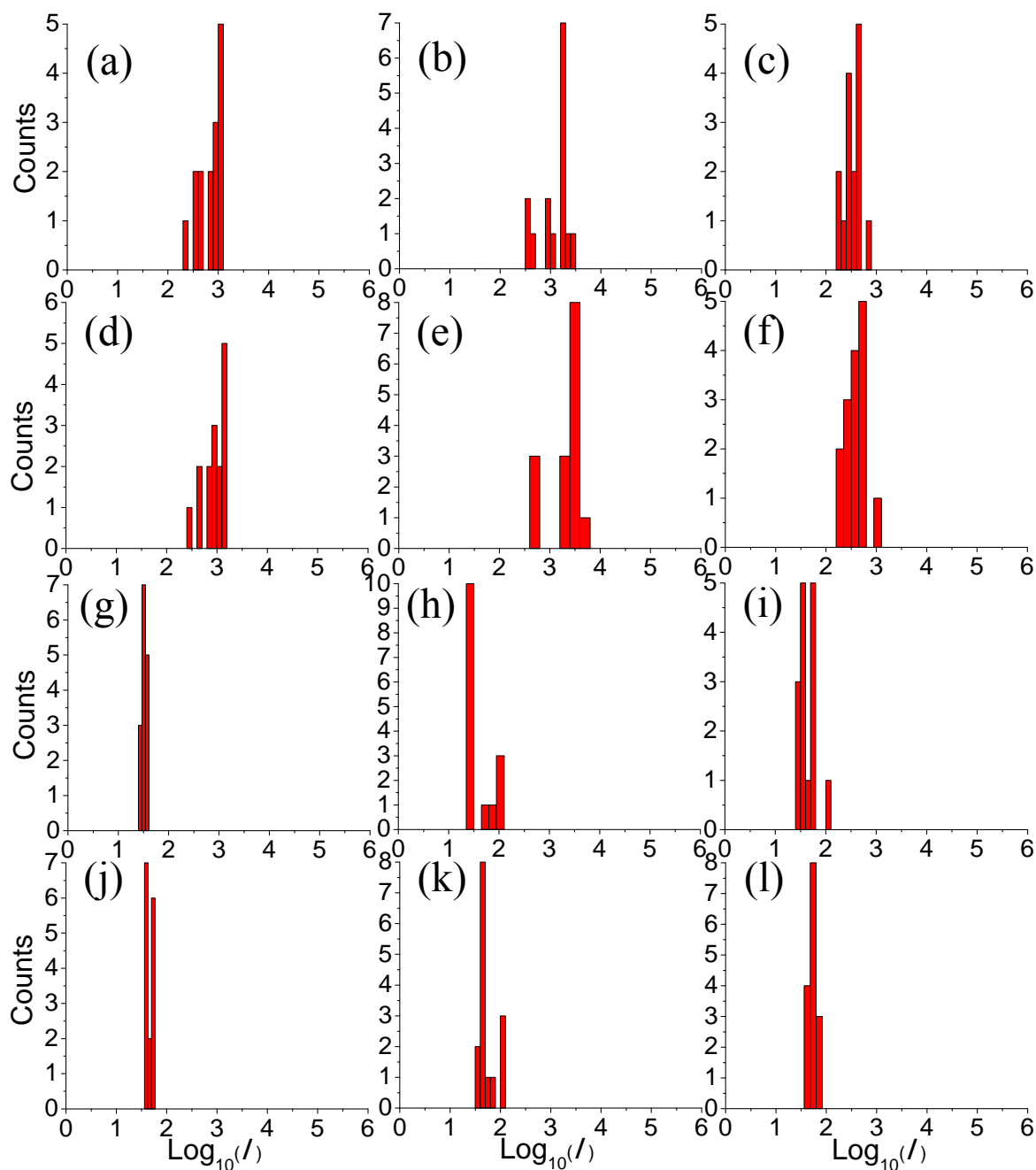


Figure 4.21: Intensity histograms of Rhodamine 101 (1 μM) in Au/Ag alloy aerogel (a) I, (b) II, and (c) III at 1504 cm^{-1} along with Au/Ag alloy aerogel (d) I, (e) II, and (f) III at 1648 cm^{-1} . Intensity histograms of Rd 101 (1 μM) in Au/Ag alloy NP (g) I, (h) II, and (i) III at 1504 cm^{-1} along with Au/Ag alloy NP (j) I, (k) II, and (l) III at 1648 cm^{-1} .

4.4 Conclusion

In summary, we have successfully synthesized Au/Ag alloy NPs and hollow NPs with distinct morphologies and transformed them into self-supported, high porous aerogels. Ag hollow NPs was used as template for alloying Au under galvanic replacement reaction onto the surface to produce Au/Ag alloy NPs. With changing the Au: Ag molar ratio, different morphologies of the alloy nanostructures has been achieved and systematically studied. The Au/Ag alloy NPs and hollow NPs solutions were concentrated using centrifuge filter technique for preparation of highly concentrated sol. With similar sol-gel process of the Ag hollow NPs, the Au/Ag alloy NPs and hollow NPs also have been successfully transformed into hydrogels with the use of tetranitromethane. The resultant Au/Ag alloy aerogels with high surface area, low density and distinct morphologies were used as SERS substrate. The SERS spectra displays significant enhancement compared to the NPs which makes it a promising material for future studies.

Chapter 5: Sol-Gel Assembly of Ag-Pt-Au Alloy Ternary Nanoparticles into Metallic Aerogels with the Application on Methanol Oxidation Catalysis

5.1 Introduction

Noble metal NPs such as Ag, Au, Pt, and Pd has gained considerable attention in the past decades due to the fascinating physical properties they exhibit in the nano-scale. These NPs have the potential to impact on several technologies, such as catalysts,²⁶ sensors,²⁷ gas storage²⁸ and photovoltaics.¹⁷ Among these applications, Pt-based nanomaterials are still the most effective catalysts for methanol oxidation reaction which can be used in the direct methanol fuel cell.^{128, 130, 178} However, the formation of CO during the catalysis process is known as a great challenge. Therefore, alloying Au into the Pt to form bimetallic or multimetallic catalysts has caused great interest.^{126,179} Since Au can perform as catalyst for oxidizing CO into CO₂, the synergy effect of Au and Pt can overcome the in situ generated CO poisoning. To date, Eychmüller's group has reported Pt-M (M=Pd, Co, Ni, Au) bimetallic catalysts and their improvement in the oxidation reduction reaction with the change of surface composition and electronic structures.^{110, 171, 180, 181} Unfortunately, the durability of the cathode catalysts caused by dissolution and/or agglomeration of Pt and catalyst poisoning still exist and limit the catalytic properties. Therefore, the development of highly porous noble metal aerogels with direct metal NP linkage, and rough metal surface has caused a lot of interest, since it will serve as a conducting catalyst with rapid diffusion of the analytes that can potentially increase the efficiency. Considering the difference of the standard reduction potential, Ag hollow NPs can be used as template to produce Au/Pt/Ag alloy NPs first and transform them into self-assembled high porous aerogel.¹⁵⁷

In this chapter, we successfully produced Au/Pt/Ag, alloy hollow NPs through galvanic replacement reaction by scarifying Ag hollow NPs as templates. The alloy hollow NPs self-assembled into highly porous aerogel superstructures via oxidative removal of the surface ligands. Furthermore, we optimized the size dispersity as well as chemical stability of the hollow NPs to achieve control over their physical properties. The resultant aerogels were applied as catalyst for the methanol oxidation reactions, and catalytic performance was discussed.

5.2 Experimental Section

Materials

Chloroplatinic (IV) acid hexahydrate ($\text{H}_2\text{PtCl}_4 \cdot 6\text{H}_2\text{O}$) 99%, chloroauric (III) acid (HAuCl_4) 99%, tetranitromethane ($\text{C}(\text{NO}_2)_4$), L-glutathione (GSH) reduced 98% and Nafion 117 solution (~5% in a mixture of lower aliphatic alcohols and water) were purchased from Sigma-Aldrich. Silver nitrate (AgNO_3) 99.9% and sodium borohydride (NaBH_4) 98% were purchased from Strem Chemicals. Sodium hydroxide (ACS grade), Potassium hydroxide (ACS grade), isopropanol (ACS grade), methanol (99.8%, Extra Dry, AcroSeal™) and acetone (ACS grade) were purchased from Fisher Scientific. 18 M Ω Milli-Q filtered water was used in the synthesis of all samples. All chemicals were used as received with no purification.

Synthesis of Ag Hollow NPs

Ag hollow NP templates were synthesized by following previously reported procedure. Typically, a 250 mL round bottom flask is placed in an ice-cold water bath and 50 mL of ultrapure water, 1.00 mL of 10 mM AgNO_3 , and 100 μL of 10 mM GSH were added. After 1 min vigorous stirring, 10.00 mL of 0.1 M NaOH was injected to produce precursor Ag_2O seeds. Then, 3.60 mL of 10 mM NaBH_4 was swiftly injected that caused an immediate color change

from pale-yellow to orange-pink, indicating the formation of hollow Ag NPs. The resulting mixture was left in the ice water bath for 30 min. prior to galvanic replacement.

Synthesis of Ag-Pt-Au Ternary Alloy Hollow NPs Sol

Synthesis of Ag/Pt/Au alloy NPs was achieved by galvanic displacement of the pre-formed hollow Ag NPs. Typically, 10 mL of 0.5 mM H_2PtCl_6 was injected to the as-prepared Ag hollow NP solution at a rate of 2 mL min^{-1} , which caused a color change to pink-purple. After 30 min, 10 mL of 0.5 mM HAuCl_4 was also injected at a rate of 2 mL min^{-1} to produce a clear purple solution, suggesting the growth of ternary Ag/Pt/Au alloy hollow particles. This process was repeated 8 times to produce $\sim 700 \text{ mL}$ Ag/Pt/Au sol. The concentrated ternary sols were prepared by centrifuge filtration. Specifically, the centrifuge filters (MWCO 300,000) filled with 20 mL of Ag-Pt-Au sols were centrifuged at 3500 rpm for 9 min to remove 18 mL solution. This process was repeated until 8 mL of sol with a concentration of 0.02 M left (based on the AgNO_3 used), and saved for future use.

Synthesis of Ag-Pt-Au Alloy Hydrogels and Aerogels

The 8 mL sol was divided into 4 glass vials with 2 mL aliquots. Three different amount of $\text{C}(\text{NO}_2)_4$ were added into each vial to produce different morphologies of the Ag-Pt-Au hydrogels, which were 75 μL of 1% $\text{C}(\text{NO}_2)_4$, 350 μL of 1% $\text{C}(\text{NO}_2)_4$, and 350 μL of 7% $\text{C}(\text{NO}_2)_4$. The $\text{C}(\text{NO}_2)_4$ treated sols were kept in the dark after vigorous shaking to induce the gelation. Gradual condensation of the NP sol into solvent swollen, polymeric hydrogel is noted within 4-6 h. The resultant hydrogels were first washed with ultrapure water for 4-5 times to remove the byproducts of the synthesis, followed by acetone for 5-6 times until the yellow color supernatant disappears. The acetone exchanged hydrogels were loaded into CO_2 supercritical dryer and exchanged with liquid CO_2 at 15°C for 6-8 times. Finally, the gels immersed in liquid

CO₂ were dried under supercritical conditions (1350 psi and 40 °C) to produce the Ag/Pt/Au ternary aerogels.

5.3 Results and Discussion

Previously, we have reported the synthesis of Au/Ag NPs and hollow NPs through GRR using Ag hollow NPs as templates.¹⁸² However, this method can be further expanded to alloy Ag hollow NPs with other noble metals in order to be used into more applications. Unfortunately, no matter what kind of commercial available Pt catalyst, either by itself or doped with Ni, they are still get pensioned by the in situ generated CO from the reaction and lost its catalytic activity. Since Au has been well known as the CO oxidation catalyst, alloying Au into Pt to make a porous material for methanol oxidation has become a great challenge. As the difference in standard reduction potential, both Au³⁺ and Pt⁴⁺ ions can oxidize Ag into Ag⁺, but Au³⁺ cannot oxidize Pt to Pt²⁺. In this case, Ag hollow NPs can be used as the template, by a slowly injection of the K₂PtCl₄ and HAuCl₄, the ternary hollow NPs can be obtained (Figure 5.1).^{113, 114}

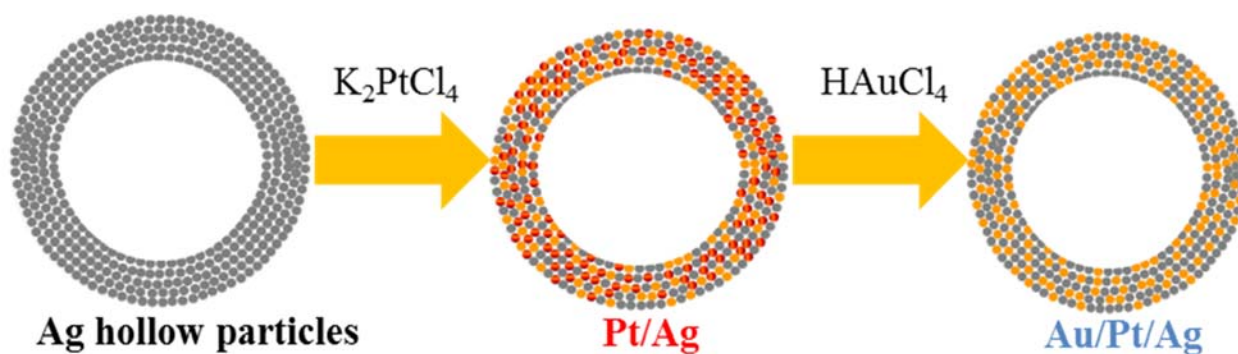


Figure 5.1: Schematic view of GRR of Pt and Au on the Ag hollow NPs for the formation of Au/Pt/Ag ternary hollow NPs.

The optical property of noble metal NPs are controlled by the composition and morphology. We have reported the tuning SPR maximum of Ag hollow NPs and Au/Ag hollow NPs through varying outer diameter and composition change.^{117,183} Similarly, with the composition change of adding Pt salt, the SPR maximum of Ag hollow NP started from 500 nm shifted to 520 nm. It can be further shifted to 560 nm after introduction of Au salt into the solution, as well as a larger value of the FWHM, indicating the successful alloying of the ternary hollow NPs.^{42,184}

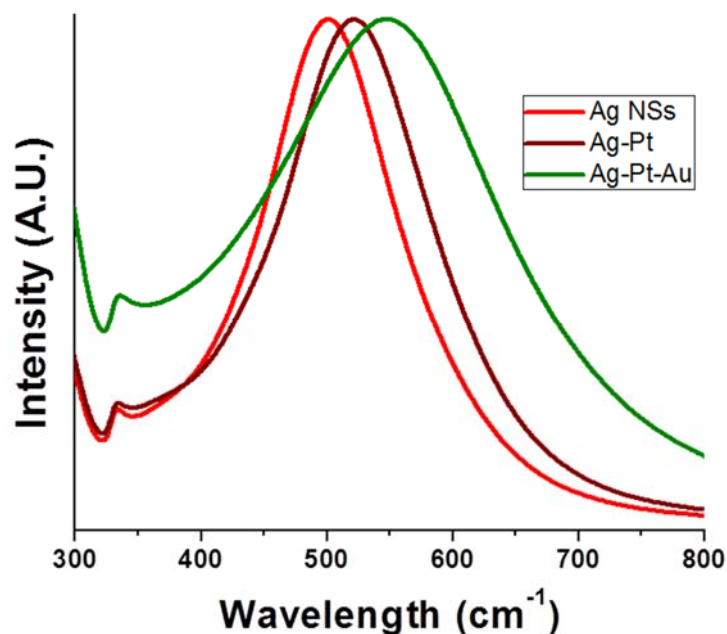


Figure 5.2 UV-Vis absorption of Ag hollow NPs (green), Pt/Ag alloy hollow NPs (brown) and Au/Pt/Ag hollow NPs (Red).

Low resolution TEM was applied to investigate the morphology and size of the ternary hollow NPs. As shown in Figure 5.3, the hollow NPs exhibit similar spherical morphology as the Ag hollow NPs in Figure 5.4. By counting over 200 hollow NPs size through different samples, the average outer diameter is 44.3 ± 5.5 nm and shell thickness is 8.6 ± 1.1 nm. That represents the part of the Ag atom in the NPs have been replaced by Pt and Au, and dissolved into the

solution, which is constant as the Au/Ag GRR reaction. Interestingly, the Ag:Pt:Au ratio is 2:1:1 to yield the spherical shape. If the ratio of increased to 2:1.5:1.5 or even higher amount of Au and Pt, the hollow NPs will break up into small NPs first and then lost their colloidal stability. So the ratio applied in this method is the maximum Au and Ag that possibly can be used.

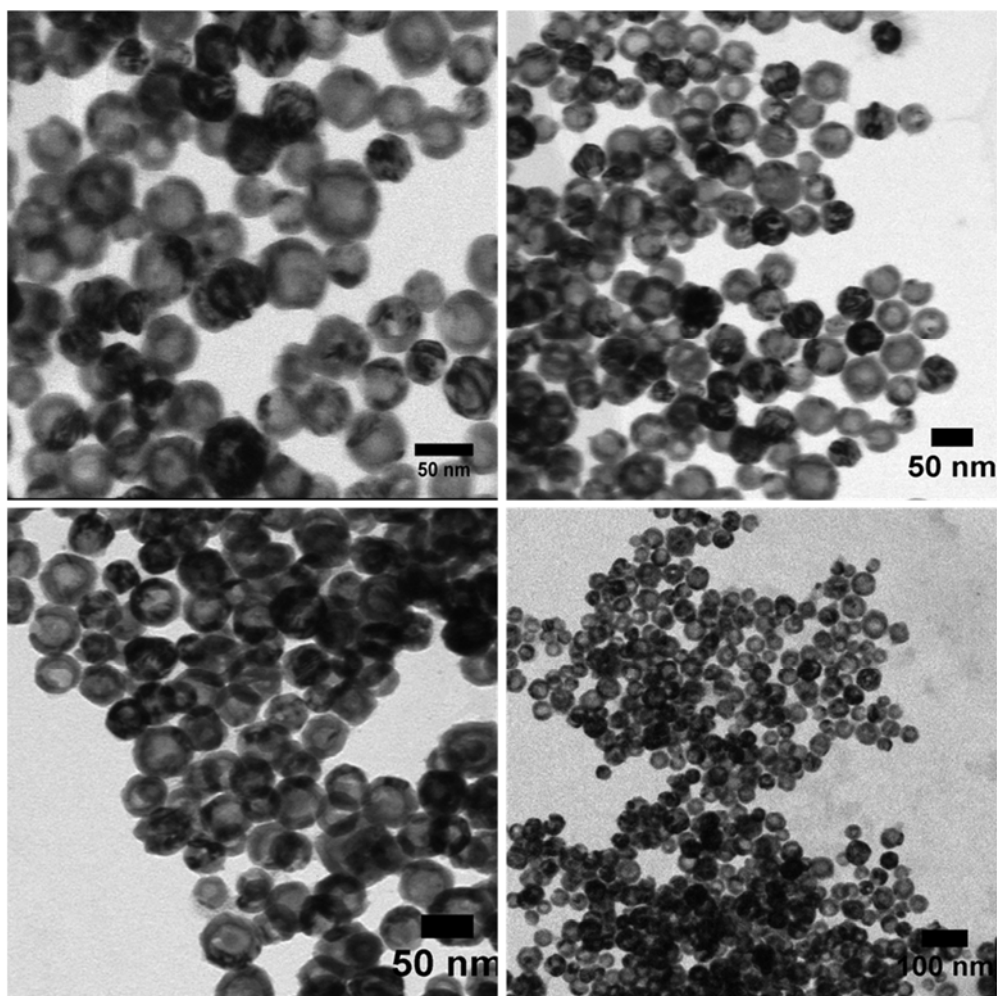


Figure 5.3: TEM images of ternary Au/Pt/Ag hollow NPs.

In order to further investigate on the alloying effect of the ternary hollow NPs, STEM-EDS mapping was used to study the elemental distribution in the NPs. Figure 5.4 shows the dark field STEM image of the ternary hollow NPs, followed with the elemental mapping of Pt, Ag and Au, respectively. It is obvious that the three elements are evenly distributed all over the

hollow NPs, indicating a homogeneous alloying effect. More important, small NPs are also shown around the hollow NPs which mainly compose Pt, which means Pt resource might be still higher than needed. Therefore, according to the STEM study, a significant decrease of Ag proves that Pt^{4+} and Au^{3+} replaced the Ag atoms in the hollow NPs.

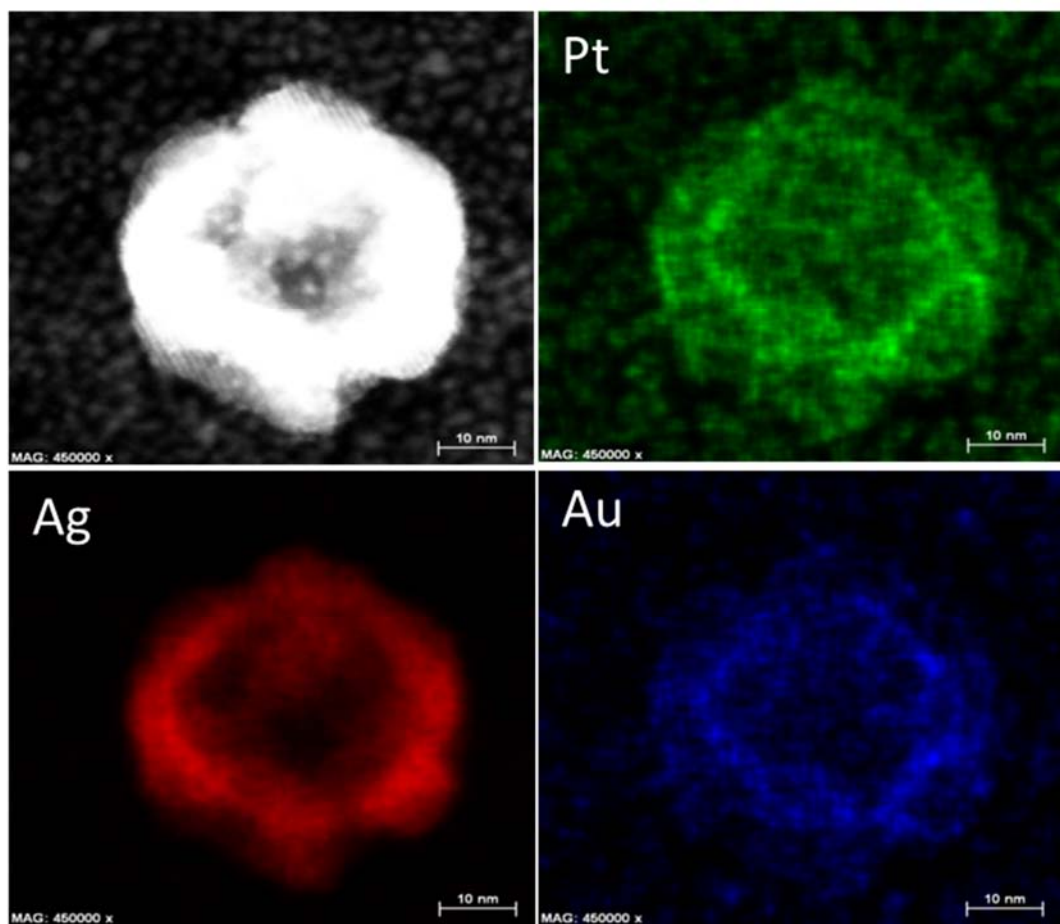


Figure 5.4: STEM image of Au/Ag alloy hollow NP along with elemental maps of Pt, Ag and Au.

After the synthesis of the ternary hollow NPs, the as prepared solution was washed with water and then concentrated using centrifuge filters to remove excess water and other ionic byproduct. The final sol concentration is 10 mM which can be treated with oxidizing agent $\text{C}(\text{NO}_2)_4$ for hydrogel formation. Similarly to previous study, the surface thiolate ligand can be

oxidized to form sulfenyl nitrates and further to disulfides and dissolved into the solution, leaving active spots on the surface of the hollow NPs.^{112,157} Such spots on different NPs can build direct cross-linkage that resulted in the NP condensation for formation of hydrogels (Figure 5.5). Different from other hydrogel, the ternary hydrogel condensed from sideways and condense to the middle yield a freestanding gel structure. Such observation can be due to the different surface tension of the hydrogel surface verse the water and more study will be performed in the future.¹⁸⁵ After the formation of the hydrogel, acetone change was applied several times to remove the byproducts during the sol-gel process. The wet-gel was loaded into supercritical drying to produce the aerogel. The ternary aerogel is in black color, with extremely low density ($0.120 \text{ g}\cdot\text{cm}^{-3}$) that is only about 1.2% compared to the corresponding bulk alloys.

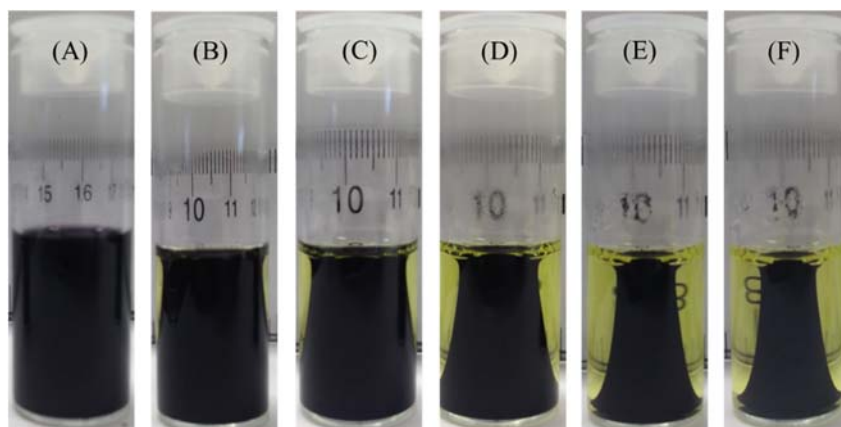


Figure 5.5: Photographs showing the condensation of Au/Pt/Ag NPs into opaque hydrogels: (A) concentrated sol, (B) after 2 hours, (C) after 4 hours, (D) after 6 hours (E) after 8 hours, and (F) after 12 hours. The top scale bar is in inches.

In order to study the morphology and elemental composition of the aerogel, both low resolution TEM and STEM-EDS mapping are used. Different from the Ag aerogel, the ternary aerogel has a large number of smaller NPs which are direct cross-linked to produce a

nanoparticulate gel framework. It is likely that the NPs are generated through the breakup of the large hollow NPs during the sol-gel process. Since the in situ produced HNO_3 etches Ag atoms into Ag^+ , part of the hollow NPs can't retain their original morphology and breakup into smaller NPs. However, significant amount of hollow NPs still exist and randomly distributed on the network, providing inter-particles gaps for many applications.^{100,186} Figure 5.7 shows the dark field STEM image and elemental mapping of the ternary aerogel. Both Pt and Au are homogeneous distributed in the gel network, but Ag is more concentrated at the hollow NPs sites. That is probably because during the sol-gel process, more surface atoms are etched by the oxidizing agent, leaving the inner part of the hollow NPs which get less replacement by Pt and Au in the previous step. However, the elemental mapping proves that the aerogel superstructure contains both Pt and Au that can be used as methanol oxidation catalysis.

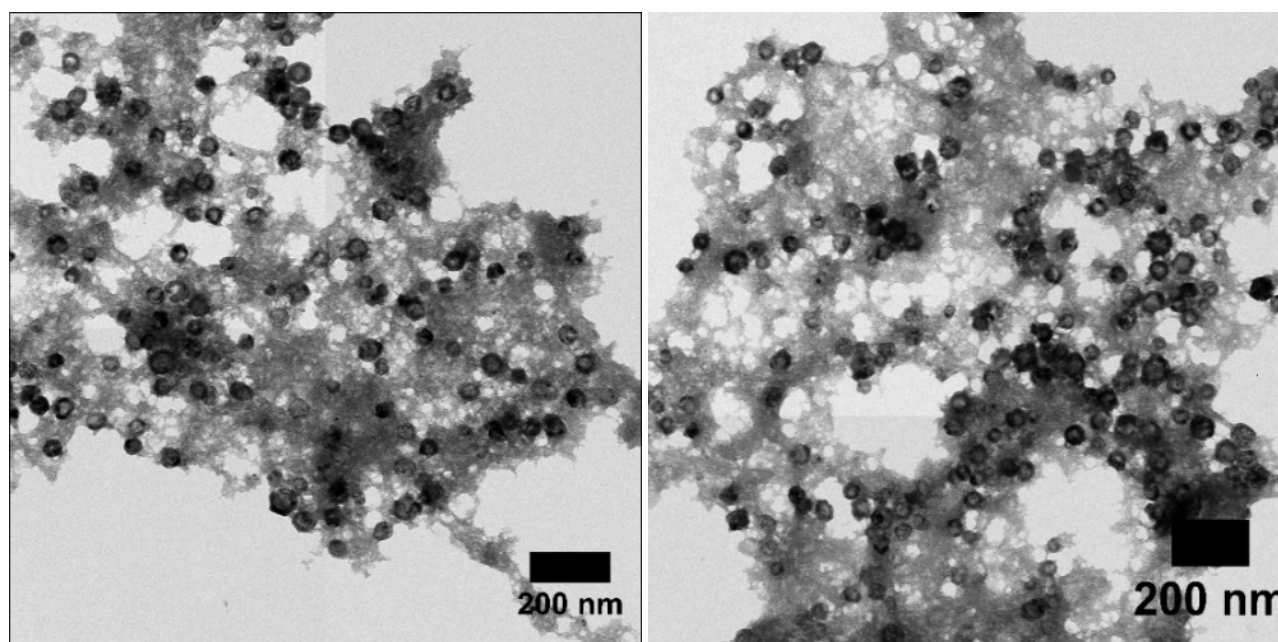


Figure 5.6: TEM images of ternary hollow NPs formed aerogel.

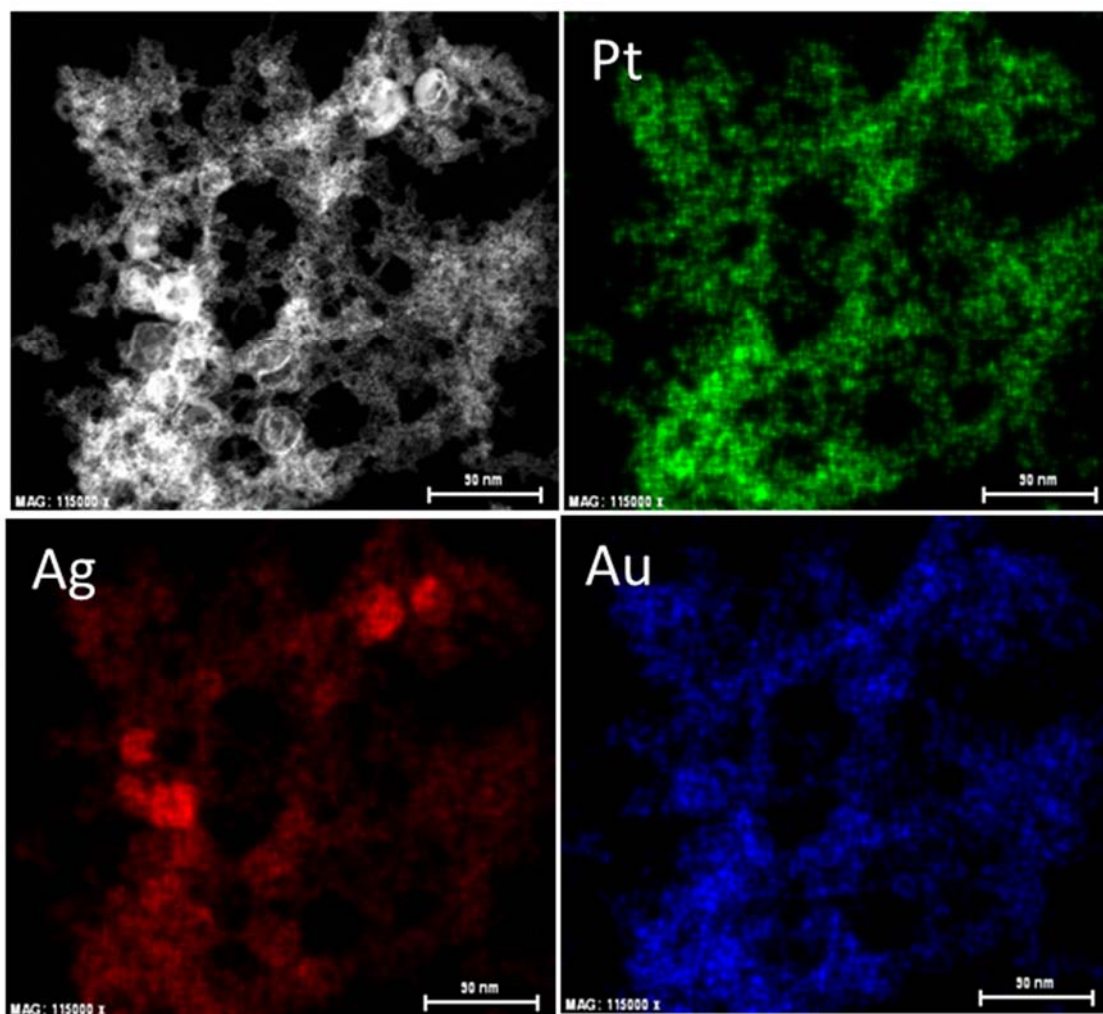


Figure 5.7: STEM image of Au/Ag alloy aerogel along with elemental maps of Pt, Ag and Au.

The PXRD of ternary hollow NPs and aerogel were recorded for structural evaluation. The diffraction pattern of Au/Pt/Ag hollow NPs is consistent with cubic Ag (PDF # Ag 01-0870-719), Pt (PDF # Ag 01-0870-719), and Au (PDF # Ag 01-0870-719) phase. However, there is a slight shift that made the peaks are in between of the three patterns.^{171,175} That is due to the change of lattice d-spacing discussed in chapter 2. The diffraction peaks corresponding to AgCl was not detected because the addition of ascorbic acid reduces some of Ag^+ to Ag that avoided the formation of AgCl. As describe in the TEM analysis, since the formation of a lot of broken NPs, the aerogel lost its crystallinity. The aerogels' property change may affect the application

such as catalysis because usually only certain facets in the crystal structure have been shown to exhibit maximum catalytic activity. Therefore, more work will be focused on keeping the crystalline structures of the aerogel during the sol-gel transformation in the future.

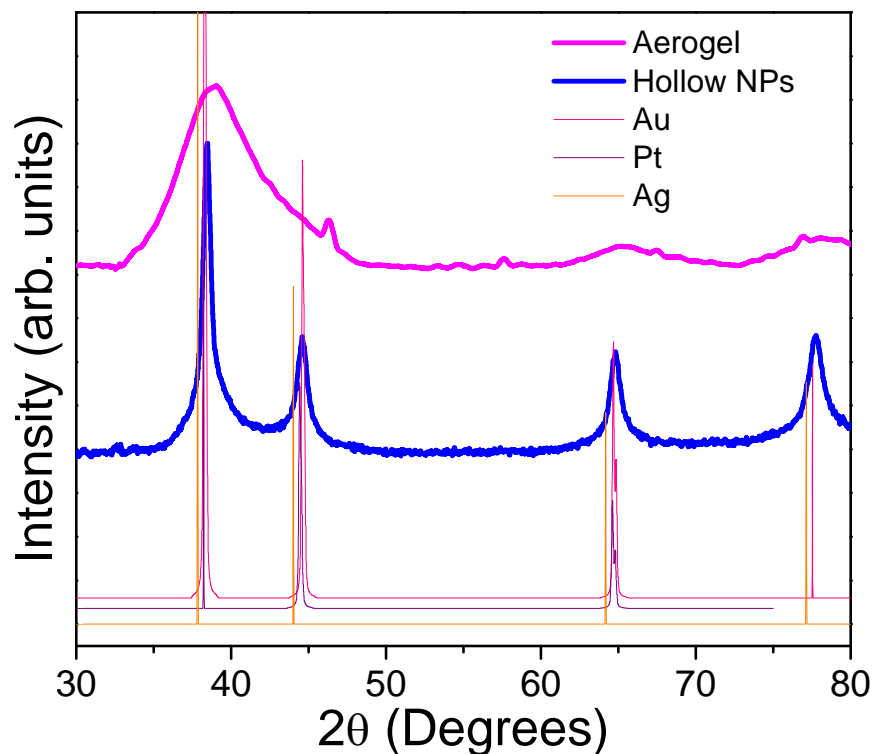


Figure 5.8: PXRD patterns of ternary hollow NPs and corresponding Au/Pt/Ag aerogel.

Nitrogen adsorption/desorption isotherms of ternary alloy aerogel were performed for surface area analysis and pore size distribution study. As shown in Figure 5.9, the shape of the isotherm corresponds to type IV curves, which means mesopores are present in the framework. The significant increase at higher P/P_0 matches a type II curve suggesting some macroporosity in the network. In addition, hysteresis loops in the desorption isotherm indicates both slit and cylindrical shaped pores. By fitting into the BET model, the surface areas were calculated to be $173 \text{ m}^2/\text{g}$, which is extremely high compared to reported values. The highly porous property

makes the ternary aerogels a promising material for many applications like catalysis, storage and chemical sensing.^{98,124}

The pore size distribution and cumulative pore volumes of the aerogel were acquired by fitting the BJH model to the desorption isotherm. A bi-modal pore volume distribution was observed. The big peak centering at 25-30 nm representing the network pores, whereas the small peak centering at 3-4 nm is suggested to be the inter-particle gas between the NP network and hollow NPs.

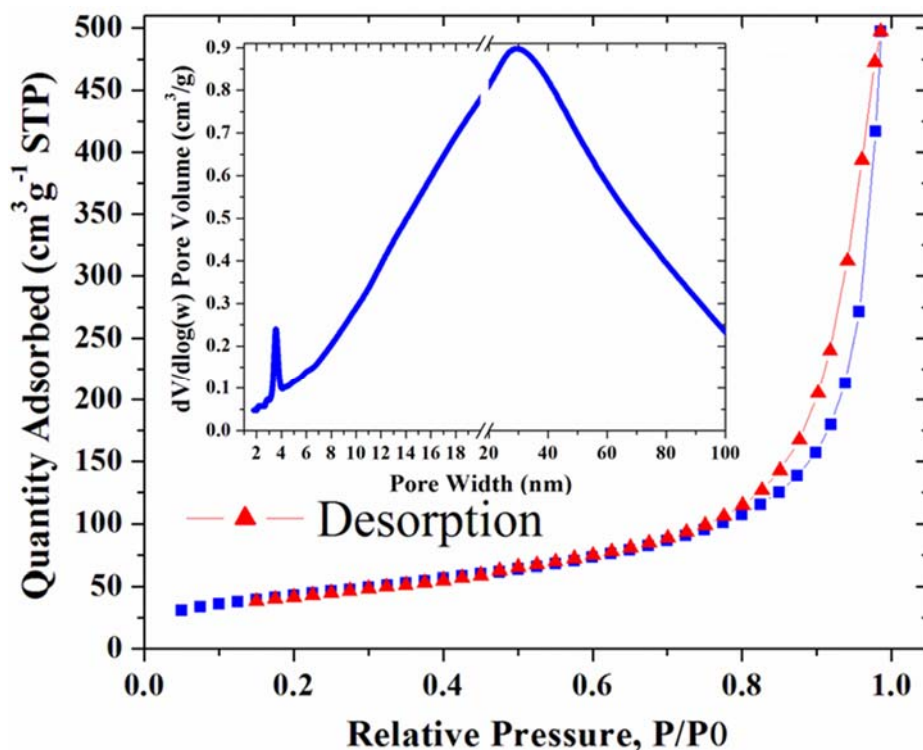


Figure 5.9: Nitrogen adsorption (blue) desorption (red) isotherms of ternary aerogel. The BJH model pore distribution plots are shown as insets.

The catalytic properties of the ternary aerogel are examined in the methanol oxidation reaction and ternary alloy aerogel electrodes displayed an exceptionally high catalytic activity toward the electro-oxidation of methanol.^{129, 178, 187} The CVs for the electro-oxidation of

methanol at a scan rate of 50 mVs^{-1} are depicted in Figure 5.10. Two current peaks characteristic of methanol electro-oxidation can be identified in all the obtained CVs similar to those obtained with a bulk platinum electrode. The symmetric anodic peak around -0.3 volts observed in the forward scan can be assigned to the oxidation of freshly adsorbed methanol species. As the methanol concentration increased the anodic peak current density increased, became less symmetric and the peak potential shifted to a less negative value (e.g. zero volts at 12 M methanol). Surprisingly, there hasn't shown any decrease in the anodic peak current density upon increasing the methanol concentration up to 12 M, indicating an excellent and superior catalytic performance of this sample over the commercially available Pt/C catalysts.¹⁸⁸ The superior electrocatalytic performance toward the methanol oxidation can be attributed to both the alloying effect and the unique microstructure of the aerogel. During the reverse scan, an anodic oxidation current peak around -0.4 volts was recorded. This peak can be attributed to sweeping the incompletely oxidized carbonaceous organic intermediates formed on the electrode surface during the forward potential sweep. The ability of the aerogel electrodes to handle very high concentrations of methanol is reflecting the high capability of these aerogels to resist the poisoning effects.¹⁸⁴

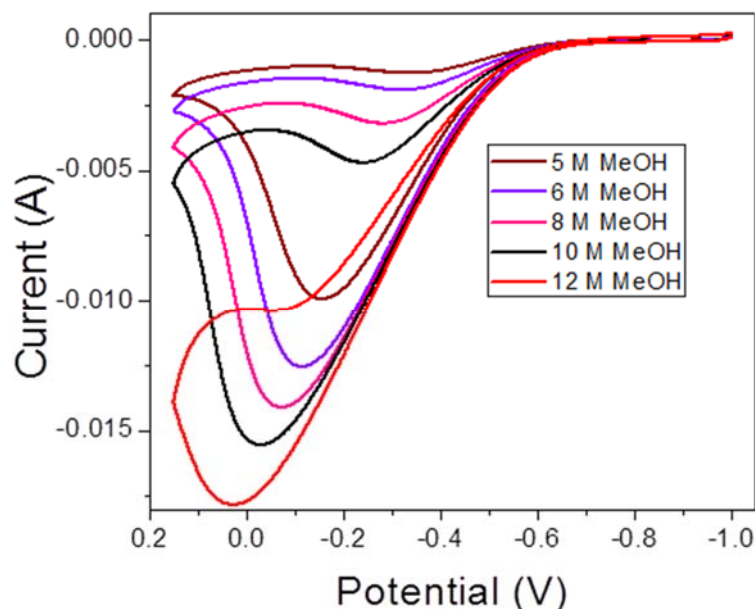


Figure 5.10: CVs for the electro-oxidation of methanol with different concentrations.

5.4 Conclusion

In this project, we have successfully synthesized Au/Pt/Ag ternary alloy hollow NPs through GRR with Ag hollow NPs as template. The NPs display homogenous distribution of all three elements and keep the original hollow morphology of Ag templates with the appropriate amount of Au and Pt alloyed. Moreover, such ternary hollow NPs can be assembled into high surface area and self-supported aerogel superstructures under sol-gel transformation. The aerogel with a large number of micro to mesopores shows direct NP to NP linkage with a random distribution of hollow NPs on the network. Unfortunately, the powder XRD proves that the aerogel lost the crystallinity compared to the hollow NPs and the reason is still unclear. The performance of the aerogel as a catalyst for methanol oxidation was studied via CV showing significant promising result for the high capability and outstanding catalytic performance. More studies on tuning the physical properties and improving catalytic behavior are currently underway.

Chapter 6: Conclusion

In this dissertation, we have successfully developed a novel strategy for direct cross-linking of noble metal NPs into high surface area metallic gel frameworks, transparent and opaque, via oxidative removal of surfactant ligands. First, we established a new methodology for production of noble metal NPs and hollow NPs with control of morphology, crystal phase, and tunable plasmonic properties. Secondly, as prepared colloidal NPs were condensed into wet “jello-like” hydrogels with direct interfacial linkages upon chemical oxidation of thiolate ligands. Hydrogels have been supercritically dried to produce monolithic metal aerogels. The resulting Ag, Au/Ag, Au/Pt/Ag aerogel are proven to be promising candidates for SERS-based chemical sensing and electrocatalytic studies.

In Chapter 3, we have successfully demonstrated the synthesis of size and shell thickness tunable Ag hollow NPs and their self-supported assembly into transparent and opaque Ag gel frameworks via oxidative removal of the GSH surface functionalities. The Ag hollow NPs prepared by fast chemical reduction of Ag_2O exhibit narrow and tunable plasmonic bands in the visible spectrum (470-570 nm) that are significantly red-shifted from those of the solid NP counterparts (410-420 nm). Glutathione surface functionality has been used to produce highly-concentrated (0.03-0.05 M) Ag NP sols via centrifuge filtration whereas the introduction of $\text{C}(\text{NO}_2)_4$ was utilized for the oxidative removal of glutathione, leading to direct cross-linking of Ag hollow NPs into metallic Ag gel frameworks. The oxidant/thiolate molar ratio (X) determines the rate of NP condensation, which in turn determines the morphology, optical transparency, opacity, surface area and porosity of the resultant Ag aerogels. As-prepared opaque Ag aerogels exhibit extremely low densities, high-surface-area and porosities that can be tuned by varying the inner diameter of the precursor NPs as well as classic pearl necklace morphology of the base-

catalyzed silica aerogels. The high concentration of oxidant ($X > 7.7$) facilitates the oxidative etching of Ag hollow NPs into significantly smaller NPs (3.2-7.6 nm) that can result in optically transparent Ag hydrogels. While the tunable plasmonic properties of the precursor hollow NPs are lost upon sol-gel assembly the catalytic and SERS activities of the nanoscale building blocks are expected to retain in the resultant aerogel product.

In Chapter 4, we have demonstrated the synthesis of Au/Ag hollow NPs with varying morphologies and tunable plasmonic properties via galvanic replacement of the preformed Ag hollow NPs. The influence of the Au: Ag molar ratio (m value) on the evolution of SPR and morphology of alloy nanostructures has been systematically studied by employing sacrificial porous Ag templates, for the first time. As-prepared Au/Ag NPs were successfully transformed into high surface area, self-supported, bimetallic superstructures via controlled oxidation of the surfactant ligands. The resultant aerogels exhibit direct NP connectivity, extremely low density, high surface area and mesoporosity, and distinct morphologies that can be tuned by varying the nanoparticulate building block. The performance of monolithic aerogels in SERS application has been studied using Rd 101 as the probe molecule. The SERS spectra exhibit average signal intensities of 47.5 ± 6.4 - 59.0 ± 29.3 for precursor NPs and 474.7 ± 203.3 - 2231.3 ± 1079.7 for corresponding aerogel samples, under identical experimental conditions. The production of high surface area, mesoporous Au/Ag alloy aerogels will add to the overall tool box of metal aerogels with promising application in chemical sensor technologies.

In Chapter 5, synthesis of Au/Pt/Ag hollow NPs is reported, which has been shown as a promising material in methanol oxidation electrocatalysis. In this work, synthesis of Au/Pt/Ag ternary hollow NPs was achieved through GRR of the preformed Ag hollow NPs. The ternary hollow NPs exhibit homogeneous distribution of Au, Pt, and Ag while retaining the original

morphology of precursor Ag templates. As prepared ternary hollows were successfully transformed into free standing hydrogels via oxidative removal of the surfactant ligands. The resultant aerogels exhibit high surface area ($173 \text{ m}^2/\text{g}$) and pore size distribution ranging from 20-60 nm. TEM images of aerogels show direct small NP to NP linkage with numerous hollow NPs decorating on the NP formed network due to the breakup of the hollow NPs. However, the aerogel lost the crystallinity and turned into amorphous structure, most probably because of the etching of Ag by in situ generated HNO_3 . Nonetheless, the performance of the ternary aerogels for electro-oxidation of alcohol has been studied with methanol concentration up to 12 M. It has shown promising catalytic performance due to the alloying effect which overcomes the CO formation. Since the reaction catalysis commonly occurs on certain facets of the crystalline structure, retain the crystallinity from ternary hollow NPs to aerogels will be able to significantly increase the catalytic efficiency. In the future, in order to improve the mechanical stability as well as the crystallinity of the aerogels, we will attempt different approaches such as varying reaction parameters (different amount of oxidizing agent used, gelation time, drying time, and Ag:Pt:Au ratios) to produce ternary crystalline aerogel. Moreover, the electrocatalytic performance of ternary aerogels derived from above protocols will be systematically studied. Since morphology of the nanoscale material is another key factor that influences the catalytic performance, hence ternary Au/Pt/Ag aerogels that exhibit varying morphologies will also be synthesized and applied in the methanol oxidation reactions.

In conclusion, the development of alloy noble metal aerogels provides an new field for studying porous Au, Ag and Pt nanostructures with controlled chemical and physical properties. Moreover, the sol-gel condensation strategy for direct cross-linking of noble metal NPs into high surface area, mesoporous aerogels provides a versatile route to produce NP superstructures of

other nanoscale metals, semiconductors, and their hybrids. The unique properties of the aerogels, including self-supported, low density, chemical sensitivity and highly catalytic properties make them well-suited for potential applications such as chemical sensing and electro-catalysis.

Reference

1. Scher, E. C.; Manna, L.; Alivasatos, A. P., Shape Control and Applications of Nanoparticles. *Philos. Trans. Royal Soc. London A* **2003**, 361, 241-255.
2. Murray, C. B.; Kagan, C. R.; Bawendi, M. G., Synthesis and Characterization of Monodisperse Nanocrystals and Closed-Packed Nanocrystal Assemblies. *Annu. Rev. Mater. Sci.* **2000**, 30, 545-610.
3. Shevchenko, E. V.; Talapin, D. V.; Murray, C. B.; O'Brien, S., Structural Characterization of Self-Assembled Multifunctional Binary Nanoparticle Superlattices. *J. Am. Chem. Soc.* **2006**, 128, 3620-3637.
4. Crooks, R. M.; Zhao, M.; Sun, L.; Chechik, V.; Yeung, L. K., Dendrimer-Encapsulated Metal Nanoparticles: Synthesis, Characterization, and Applications to Catalysis. *Acc. Chem. Res.* **2001**, 34, 181-190.
5. Hüsing, N.; Schubert, U., Aerogels-Airy Materials: Chemistry, Structure, and Properties. *Angew. Chem. Int. Ed.* **1998**, 37, 22-45.
6. Rolison, D. R., Catalytic Nanoarchitectures-the Importance of Nothing and the Unimportance of Periodicity. *Science* **2003**, 299, 1698-1701.
7. Trindale, T. O.; O'Brien, P.; Pickett, N. L., Nanocrystalline Semiconductors: Synthesis, Properties, and Perspectives. *Chem. Mater.* **2001**, 13, 3843-3858.
8. Viswanath, B.; Patra, S.; Munichandraiah, N.; Ravishankar, N., Nanoporous Pt with High Surface Area by Reaction-Limited Aggregation of Nanoparticles. *Langmuir* **2009**, 25, 3115-3121.
9. Norman, T. J.; Grant, C. D.; Magana, D.; Zhang, J. Z.; Liu, J.; Cao, D. L.; Bridges, F.; Van Buuren, A., Near Infrared Optical Absorption of Gold Nanoparticle Aggregates. *J. phys. Chem. B* **2002**, 106, 7005-7012.

10. Hybertsen, M. S., Absorption and Emission of Light in Nanoscale Silicon Structures *Phys. Rev. Lett.* **1994**, 72, 1514–1517.
11. Emmerling, A.; Petricevic, R.; Beck, A.; Wang, P.; Scheller, H.; Fricke, J., Relationship Between Optical Transparency and Nanostructural Features of Silica Aerogels *J. Non-Cryst. Solids* **1995**, 185, 240–248.
12. Kovalev, D.; Heckler, H.; Ben-Chorin, M.; Polisski, G.; Schwartzkopff, M.; Koch, F., Breakdown of the k-Conservation Rule in Si Nanocrystals. *Phys. Rev. Lett.* **1998**, 81, 2803–2806.
13. Fang, Y.-Y.; Xie, J.; Tolle, J.; Roucka, R.; D'Costa, V. R.; Chizmeshya, A. V. G.; Menendez, J.; Kouvetakis, J., Molecular-Based Synthetic Approach to New Group IV Materials for High-Efficiency, Low-Cost Solar Cells and Si-Based Optoelectronics. *J. Am. Chem. Soc.* **2008**, 130, 16095-16102.
14. Kim, J. K.; Park, J., Foldable Transparent Substrates with Embedded Electrodes for Flexible Electronics. *ACS Appl. Mater. Interfaces* **2015**, 7, 18754-18580.
15. Long, J. W.; Swider-Lyons, K. E.; Stroud, R. M.; Rolison, D. R., Design of Pore and Matter Architectures in Manganese Oxide Charge-Storage Materials. *Electrochem. Solid-State Lett.* **2000**, 3, 453-456.
16. Barnham, K. W. J.; Mazzer, M.; Clive, B., Resolving the Energy Crisis: Nuclear or Photovoltaics? *Nat. Mater.* **2006**, 5, 161-164.
17. Hightower, M.; Pierce, S. A., The Energy Challenge. *Nature* **2008**, 42, 285-286.
18. Schloegl, R., Energy: Fuel for Thought. *Nat. Mater.* **2008**, 7, 72-774.
19. Labille, J.; Brant, J., Stability of Nanoparticles in Water. *Nanomedicine* **2010**, 5, 985–998.

20. Gaponik, N.; Wolf, A.; Marx, R.; Lesnyak, V.; Schilling, K.; Eychmuller, A., Three-Dimensional Self-Assembly of Thiol-Capped CdTe Nanocrystals: Gels and Aerogels as Building Blocks for Nanotechnology. *Adv. Mater.* **2008**, 20, 4257–4262.
21. Jo, H. Y.; Jung, I.; Choi, C. S.; Kim, I.; Lee, H. M., Synthesis and Characterization of Low Temperature Sn Nanoparticles for the Fabrication of Highly Conductive Ink *Nanotechnology* **2011**, 22, 225701.
22. Rao, C. N. R.; Kulkarni, G. U.; Thomasa, P. J.; Edwards, P. P., Metal Nanoparticles and Their Assemblies. *Chem. Soc. Rev.* **2000**, 29, 27-35.
23. Anderson, M. L.; Stroud, R. M.; Rolison, D. R., Enhancing the Activity of Fuel-cell Reactions by Designing Three-dimensional Nanostructured Architectures: Catalyst-modified Carbon-Silica Composite Aerogels. *Nano Lett.* **2002**, 2, 235-240.
24. Chen, Z.; Zhan, P.; Wang, Z.; Zhang, J.; Zhang, W.; Ming, N.; Chan, C. T.; Sheng, P., Two- and Three-Dimensional Ordered Structures of Hollow Silver Spheres Prepared by Colloidal Crystal Templating. *Adv. Mater.* **2004**, 5, 417-422.
25. Sreeprasad, T. S.; Samal, A. K.; Pradeep, T., One-, Two-, and Three-Dimensional Superstructures of Gold Nanorods Induced by Dimercaptosuccinic Acid. *Langmuir* **2008**, 24, 4589-4599.
26. Collins, G.; Blömker, M.; Osiak, M.; Holmes, J. D.; Bredol, M.; O'Dwyer, C., Three-Dimensionally Ordered Hierarchically Porous Tin Dioxide Inverse Opals and Immobilization of Palladium Nanoparticles for Catalytic Applications. *Chem. Mater.* **2013**, 25, 4312–4320.
27. Sun, Y.; Xia, Y., Gold and Silver Nanoparticles: A Class of Chromophores with Colors Tunable in the Range from 400 to 750 nm. *Analyst* **2003**, (128), 686-691.

28. Li, X. G.; He, Y. Q.; Swihart, M. T., Surface Functionalization of Silicon Nanoparticles Produced by Laser-Driven Pyrolysis of Silane followed by HF-HNO₃ Etching. *Langmuir* **2004**, *20*, 4720–4727.
29. Klajn, R.; Bishop, K. J. M.; Fialkowski, M.; Paszewski, M.; Campbell, C. J.; Gray, T. P.; Grzybowski, B. A., Plastic and Moldable Metals by Self-Assembly of Sticky Nanoparticle Aggregates. *Science* **2007**, *316*, 261-264.
30. Solomon, S. D.; Bahadory, M.; Jeyarajasingam, A. V.; Rutkowsky, S. A.; Boritz, C., Synthesis and Study of Silver Nanoparticles. *J. Chem. Educ.* **2007**, *84*, 322-325.
31. Pal, A.; Shah, S.; Devi, S., Synthesis of Au, Ag and Au–Ag Alloy Nanoparticles in Aqueous Polymer Solution Colloids and Surfaces. *Colloids Surf., A* **2007**, (302), 51-57.
32. Campbell, C. T., Physics: The Active Site in Nanoparticle Gold Catalysis. . *Science* **2004**, *306*, 234-235.
33. An, K.; Somorjai, G. A., Size and Shape Control of Metal Nanoparticles for Reaction Selectivity in Catalysis. *ChemCatChem* **2012**, *4*, 1512-1524.
34. Steigerwald, M. I.; Brus, L. E., Semiconductor Crystallites: A Class of Large Molecules. *Acc. Chem. Res.* **1990**, *23*, 183-188.
35. Alivisatos, A. P., Semiconductor Clusters, Nanocrystals, and Quantum Dots. *Science* **1996**, *271*, 933-937.
36. Redela, E.; Krämera, J.; Thomannb, R.; Janiak, C., Synthesis of Co, Rh and Ir Nanoparticles from Metal Carbonyls in Ionic Liquids and Their Use as Biphasic Liquid–Liquid Hydrogenation Nanocatalysts for Cyclohexene. *J. Org. Chem.* **2009**, *694*, 1069-1075.
37. Leventis, N.; Chandrasekaran, N.; Sadekar, A. G.; Mulika, S.; Sotiriou-Leventis, C., The Effect of Compactness on the Carbothermal Conversion of Interpenetrating Metal

Oxide/Resorcinol-Formaldehyde Nanoparticle Networks to Porous Metals and Carbides *J. Mater. Chem.* **2010**, 20, 7456-7471.

38. Califano, M.; Franceschetti, A.; Zunger, A., Lifetime and Polarization of the Radiative Decay of Excitons, Biexcitons, and Trions in CdSe Nanocrystal Quantum Dots. *Phys. Rev. B* **2007**, 75, 115401/1-115401/7.

39. Klajn, R.; Gray, T. P.; Wesson, P. J.; Myers, B. D.; Dravid, V. P.; Smoukov, S. K.; Grzybowski, B. A., Bulk Synthesis and Surface Patterning of Nanoporous Metals and Alloys from Supraspherical Nanoparticle Aggregates. *Adv. Funct. Mater.* **2008**, 18, 2763-2769.

40. Katsoulidis, A. P.; He, J.; Kanatzidis, M. G., Functional Monolithic Polymeric Organic Framework Aerogel as Reducing and Hosting Media for Ag nanoparticles and Application in Capturing of Iodine Vapors. *Chem. Mater.* **2012**, 24, 1937-1943.

41. Colson, A. C.; Whitmire, K. H., Synthesis of $\text{Fe}_{2-x}\text{Mn}_x\text{P}$ Nanoparticles from Single-Source Molecular Precursors. *Chem. Mater.* **2011**, 23, 3731-3739.

42. Lee, D.; Jang, H. Y.; Hong, S.; Park, S., Synthesis of Hollow and Nanoporous Gold/Platinum Alloy Nanoparticles and Their Electrocatalytic Activity for Formic Acid Oxidation. *J. Colloid Interf. Sci.* **2012**, 388, 74-79.

43. Zhang, X.; Marocico, C. A.; Lunz, M.; Gerard, V. A.; Gun'ko, Y. K.; Lesnyak, V.; Gaponik, N.; Susa, A. S.; Rogach, A. L.; Bradley, A. L., Wavelength, Concentration, and Distance Dependence of Nonradiative Energy Transfer to a Plane of Gold Nanoparticles. *ACS Nano* **2012**, 6, 9283-9290.

44. Hitihami-Mudiyanselage, A.; Senevirathne, K.; Brock, S. L., Bottom-Up Assembly of Ni_2P Nanoparticles into Three-Dimensional Architectures: An Alternative Mechanism for Phosphide Gelation. *Chem. Mater.* **2014**, 26, 6251-6256.

45. Riabinina, D.; Durand, C.; Chaker, M.; Rosei, F., Photoluminescent Silicon Nanocrystals Synthesized by Reactive Laser Ablation *Appl. Phys. Lett.* **2006**, 88, 073105/1-073105/3.
46. Muthuswamy, E.; Iskandar, A. S.; Amador, M. M.; Kauzlarich, S. M., Facile Synthesis of Germanium Nanoparticles with Size Control: Microwave versus Conventional Heating *Chem. Mater.* **2013**, 25, 1416-1422.
47. Gupta, A.; Swihart, M. T.; Wiggers, H., Luminescent Colloidal Dispersion of Silicon Quantum Dots from Microwave Plasma Synthesis: Exploring the Photoluminescence Behavior Across the Visible Spectrum. *Adv. Funct. Mater.* **2009**, 19, 696–703.
48. Abdelmoti, L. G.; Zamborini, F. P., Potential-Controlled Electrochemical Seed-Mediated Growth of Au Nanorods Directly on Electrode Surfaces. *Langmuir* **2010**, 26, 13511–13521.
49. Tolle, J.; Chizmeshya, A. V. G.; Fang, Y.-Y.; Kouvetakisa, J., Low Temperature Chemical Vapor Deposition of Si-Based Compounds via $\text{SiH}_3\text{SiH}_2\text{SiH}_3$: Metastable SiSn/GeSn/Si (100) Heteroepitaxial Structures. *Appl. Phys. Lett.* **2006**, 89, 231924/1-231924/3.
50. Lobiak, E. V.; Shlyakhova, E. V.; Bulusheva, L. G.; Plyusnin, P. E.; Shubin, Y. V.; Okotrub, A. V., Ni–Mo and Co–Mo alloy nanoparticles for catalytic chemical vapor deposition synthesis of carbon nanotubes. *Journal of Alloys and Compounds* **2015**, 621, 351-356.
51. Brinker, C. J.; Scherer, G. W., *Sol-Gel Science*. 1st ed. ed.; Harcourt Brace: San Diego, 1990.
52. Sriram, M. A.; Kumta, P. N., The thio-sol-gel synthesis of titanium disulfide and niobium disulfide. *J. Mater. Chem.* **1998**, 8, 2453-2463.
53. Arachchige, I. U.; Mohanan, J. L.; Brock, S. L., Sol-Gel Processing of Semiconducting Metal Chalcogenide Xerogels: Influence of Dimensionality on Quantum Confinement Effects in a Nanoparticle Network. *Chem. Mater.* **2005**, 17, 6644-6650.

54. Schaefer, D. W.; Keefer, K. D., Fractal Geometry of Silica Condensation Polymers. *Phys. Rev. Lett.* **1984**, 53, 1383-1386.
55. Chou, N. H.; Oyler, K. D.; Motl, N. E.; Schaak, R. E., Colloidal Synthesis of Germanium Nanocrystals Using Room Temperature Benchtop Chemistry. *Chem. Mater.* **2009**, 21, 4105-4107.
56. Henderson, E. J.; Seino, M.; Puzzo, D. P.; Ozin, G. A., Colloidally Stable Germanium Nanocrystals for Photonic Applications. *ACS Nano* **2010**, 4, 7683–7691.
57. Gao, J.; Huang, X.; Liu, H.; Zan, F.; Ren, J., Colloidal Stability of Gold Nanoparticles Modified with Thiol Compounds: Bioconjugation and Application in Cancer Cell Imaging. *Langmuir* **2012**, 28, 4464-4471.
58. Groenert, M. E.; Leitz, C. W.; Pitera, A. J.; Yang, V.; Lee, H.; Ram, R. J.; Fitzgerald, E. A., Monolithic Integration of Room-Temperature cw GaAs/AlGaAs Lasers on Si Substrates via Relaxed Graded GeSi Buffer Layers. *J. Appl. Phys.* **2003**, 93, 362-367.
59. Chriqui, Y.; Saint-Girons, G.; Isella, G.; Von Kaenel, H.; Bouchoule, S.; Sagnes, I., Long Wavelength Room Temperature Laser Operation of a Strained InGaAs/GaAs Quantum Well Structure Monolithically Grown by Metalorganic Chemical Vapour Deposition on a Low Energy-Plasma Enhanced Chemical Vapour Deposition Graded Misoriented Ge/Si Virtual Substrate. *Opt. Mater.* **2005**, 27, 846–850.
60. Shirahata, N.; Linford, M.; Furumi, S.; Pei, L.; Sakka, Y.; Gates, R. J.; Asplund, M. C., Laser-Derived One-Pot Synthesis of Silicon Nanocrystals Terminated with Organic Monolayers **2009**, 31, 4684-4686.
61. Taylor, B. R.; Kauzlarich, S. M., Solution Synthesis and Characterization of Quantum Confined Ge Nanoparticles. *Chem. Mater.* **1999**, 11, 2493-2500.

62. Baldwin, R. K.; Pettigrew, K. A.; Ratai, E.; Augustine, M. P.; Kauzlarich, S. M., Solution Reduction Synthesis of Surface Stabilized Silicon Nanoparticles. *Chem. Commun.* **2002**, 1822-1823.
63. Xu, Y.; Al-Salim, N.; Hodgkiss, J. M.; Tilley, R. D., Solution Synthesis and Optical Properties of SnTe Nanocrystals. *Cryst. Growth Des.* **2011**, 11, 2721–2723.
64. Tao, A. R.; Habas, S.; Yang, P., Shape Control of Colloidal Metal Nanocrystals. *Small* **2008**, 3, 310-325.
65. Sperling, R. A.; Parak, W. J., Surface Modification, Functionalization and Bioconjugation of Colloidal Inorganic Nanoparticles. *Phil. Trans. R. Soc. A* **2010**, 368, 1333-1383
66. Kovalenko, M. V.; Scheele, M.; Talapin, D. V., Colloidal Nanocrystals with Molecular Metal Chalcogenide Surface Ligands. *Science* **2009**, 324, 1417-1420.
67. Kovalenko, M. V.; Bodnarchuk, M. I.; Zaumseil, J.; Lee, J.-S.; Talapin, D. V., Expanding the Chemical Versatility of Colloidal Nanocrystals Capped with Molecular Metal Chalcogenide Ligands. *J. Am. Chem. Soc.* **2010**, 132, 10085-10092.
68. Pokhrel, L. R.; Dubey, B.; Scheuerman, P. R., Impacts of Select Organic Ligands on the Colloidal Stability, Dissolution Dynamics, and Toxicity of Silver Nanoparticles. *Environ. Sci. Technol.* **2013**, 47, 12877-12885.
69. Sun, Y.; Xia, Y., Shape-Controlled Synthesis of Gold and Silver Nanoparticles. *Science* **2002**, 298, 2176-2179.
70. Ratchford, D.; Shafiei, F.; Kim, S.; Gray, S. K.; Li, X., Manipulating Coupling between a Single Semiconductor Quantum Dot and Single Gold Nanoparticle. *Nano Lett.* **2011**, 11, 1049-054.

71. Wright, A.; Gabaldon, J.; Burckel, D. B.; Jiang, Y.-B.; Tian, Z. R.; Liu, J.; Brinker, J.; Fan, H., Hierachically Organized Nanoparticle Mesostructure Arrays Formed through Hydrothermal Self-Assembly. *Chem. Mater.* **2006**, 18, 3034-3038.
72. Shevchenko, E. V.; Talapin, D. V.; Kotov, N. A.; O'Brien, S.; Murray, C. B., Structural Diversity in Binary Nanoparticle Superlattices. *Nature* **2006**, 439, 55-59.
73. Urban, J. J.; Talapin, D. V.; Shevchenko, E. V.; Murray, C. B., Self-Assembly of PbTe Quantum Dots into Nanocrystal Superlattices and Galssy Films *J. Am. Chem. Soc.* **2006**, 128, 3248-3255.
74. Wessels, J. M.; Nothofer, H.-G.; Ford, W. E.; von Wrochem, F.; Scholz, F.; Vossmeier, T.; Schroedter, A.; Weller, H.; Yasuda, A., Optical and Electrical Properties of Three-Dimensional Interlinked Gold Nanoparticle Assemblies. *J. Am. Chem. Soc.* **2004**, 126, 3349–3356.
75. Shavel, A.; Gaponik, N.; Eychmüller, A., The Assembly of Semiconductor Nanocrystals. *Eur. J. Inorg. Chem.* **2005**, 18, 3613–3623.
76. Shim, B. S.; Zhu, J. A.; Jan, E.; Critchley, K.; Kotov, N. A., Transparent Conductors form Layer-by-Layer Assembled SWNT Films: Importance of Mechanical Properties and a New Figure of Merit. *ACS Nano* **2010**, 4, 3725-3734.
77. Lee, Y.; Cho, S. B.; Chung, Y.-C., Tunable Indirect to Direct Band Gap Transition of Monolayer Sc₂CO₂ by the Strain Effect. *ACS Appl. Mater. Interfaces* **2014**, 6, 14727-14728.
78. Tserbak, C.; Theodorou, G., Direct-gap Si/Ge Superlattices Strained Along the [110] and [111] Directions. *Appl. Surf. Sci.* **1996**, 102, 288-292.

79. Urban, J. J.; Talapin, D. V.; Shevchenko, E. V.; Kagan, C. R.; Murray, C. B., Synergism in Binary Nanocrystal Superlattices Leads to Enhanced p-type Conductivity in Self-assembled PbTe/Ag₂Te Thin Films. *Nat. Mater.* **2007**, 6, 115-121.
80. Zhang, F.; P., S. M., Multilayered Gold-Nanoparticle/Polyimide Composite Thin Film through Layer-by-Layer Assembly. *Langmuir* **2007**, 23, 10102-10108.
81. Radha, B.; Senesi, A. J.; O'Brien, M. N.; Wang, M. X.; Auyeung, E.; Lee, B.; Mirkin, C. A., Reconstitutable Nanoparticle Superlattices. *Nano Lett.* **2014**, 14, 2162-2167.
82. Pajonk, G. M., Catalytic Aerogels. *Catal. Today* **1997**, 35, 319-337.
83. Vacher, R.; Woignier, T.; Pelous, J.; Courtens, E., Structure and Self-Similarity of Silica Aerogels. **1988**, 37, 6500-6503.
84. Pierre, A. C.; Pajonk, G. M., Chemistry of Aerogels and Their Applications. *Chem. Rev.* **2002**, 102, 4243-4265.
85. Gacoin, T.; Malier, L.; Boilot, J.-P., Sol–Gel Transition in CdS Colloids. *J. Mater. Chem.* **1997**, 7, 859-860.
86. Gacoin, T.; Malier, L.; Boilot, J.-P., New Transparent Chalcogenide Materials Using a Sol-Gel Process. *Chem. Mater.* **1997**, 9, 1502-1504.
87. Gacoin, T.; Lahlil, K.; Larregaray, P.; Boilot, J.-P., Transformation of CdS Colloids: Sols, Gels, and Precipitates. *J. Phys. Chem. B* **2001**, 105, 10228-10235.
88. Brock, S. L.; Arachchige, I. U.; Kalebaila, K. K., Metal Chalcogenide Gels, Xerogels and Aerogels. *Comments Inorg. Chem.* **2006**, 27, 103-126.
89. Arachchige, I. U.; Brock, S. L., Sol–Gel Methods for the Assembly of Metal Chalcogenide Quantum Dots. *Acc. Chem. Res.* **2007**, 40, 801-809.

90. Hitihami-Mudiyanselage, A.; Senevirathne, K.; Brock, S. L., Assembly of Phosphide Nanocrystals into Porous Networks: Formation of InP Gels and Aerogels. *ACS Nano* **2013**, 7, 1163–1170.
91. Bigall, N. C.; Herrmann, A.-K.; Vogel, M.; Rose, M.; Simon, P.; Carrillo-Cabrera, W.; Dorfs, D.; Kaskel, S.; Gaponik, N.; Eychmüller, A., Hydorgels and Aerogels from Noble Metal Nanoparticles. *Angew. Chem. Int. Ed.* **2009**, 48, 9731-9734.
92. Liu, W.; Herrmann, A.-K.; Geiger, D.; Borchardt, L.; Simon, F.; Kaskel, S.; Gaponik, N.; Eychmüller, A., High Performance Electrocatalyst on Palladium Aerogels. *Angew. Chem. Int. Ed.* **2012**, 51, 5743-5747.
93. Ayers, M. J.; Hunt, A. J., Molecular Oxygen Sensors Based on Photoluminescent Silica Aerogels. *J. Noncrystall. Solids* **1998**, 225, 343-347.
94. Leventis, N.; Sotiriou-Leventis, C.; Zhang, G.; Rawashdeh, A.-M. M., Nanoengineering Strong Silica Aerogels
Nano Letters **2002**, 2, 957-960.
95. Zu, G.; Shen, J.; Zou, L.; Wang, W.; Lian, Y.; Zhang, Z.; Du, A., Nanoengineering Super Heat-Resistant, Strong Alumina Aerogels. *Chem. Mater.* **2013**, 25, 4757-4764.
96. Stengl, V.; Bakardjieva, S.; Subrt, J.; Szatmary, L., Titania Aerogel Prepared by Low Temperature Supercritical Drying. *Microporous and Mesoporous Mater.* **2007**, 91, 1-6.
97. Tappan, B. C.; Huynh, M.; Hiskey, M. A.; Chavez, D. E.; Luther; Mang, J. T.; Son, S. F., Ultralow-Density Nanostructured Metal Foams: Combustion Synthesis, Morphology, and Composition. *J. Am. Chem. Soc.* **2006**, 128, 6589-6594.
98. Leventis, N.; Chandrasekaran, N.; Sotiriou-Leventis, C.; Mumtaz, A., Smelting in the Age of Nano: Iron Aerogels *J. Mater. Chem.* **2009**, 19, 63-65.

99. Mohanan, J. L.; Arachchige, I. U.; Brock, S. L., Porous semiconductor chalcogenide aerogels. *Science* **2005**, 307, 397-400.
100. Arachchige, I. U.; Brock, S. L., Sol-Gel Assembly of CdSe Nanoparticles to Form Porous Aerogel Networks. *J. Am. Chem. Soc.* **2006**, 128, 7964-7971.
101. Xia, Y.; Xiong, Y. J.; Lim, B.; Skrabalak, S. E., Shape-Controlled Synthesis of Metal Nanocrystals: Simple Chemistry Meets Complex Physics? *Angew. Chem. Int. Ed.* **2009**, 48, 60-103.
102. Schwartzberg, A.; Zhang, J. Z., Novel Optical Properties and Emerging Applications of Metal Nanostructures. *J. Phys. Chem. C* **2008**, 112, 10323-10337.
103. Schwartzberg, A. M.; Olson, T. Y.; Talley, C. E.; Zhang, J. Z., Synthesis, Characterization, and Tunable Optical Properties of Hollow Gold Nanospheres. *J. Phys. Chem. B* **2006**, 110, 19935-19944.
104. Moshe, A. B.; Markovich, G., Synthesis of Single Crystal Hollow Silver Nanoparticles in a Fast Reaction-Diffusion Process. *Chem. Mater.* **2011**, 23, 1239-1245.
105. Chen, H. M.; Liu, R.-S.; Y., L. M.; Chang, S.-C.; Tsai, L.-D.; Peng, Y.-M.; Lee, J.-F., Hollow Platinum Spheres with Nano-Channels: Synthesis and Enhanced Catalysis for Oxygen Reduction. *J. Phys. Chem. C* **2008**, 112, 7522-7526.
106. Lee, C. L.; Tseng, C.-M.; Wu, C.-C.; Chou, T.-C.; Syu, C. M., High Activity of Hexagonal Ag/Pt Nanoshell Catalyst for Oxygen Electroreduction. *Nanoscale Res. Lett.* **2009**, 4, 193-196.
107. Guo, S.; Fang, Y.; Dong, S.; Wang, E., High-Efficiency and Low-Cost Hybrid Nanomaterial as Enhancing Electrocatalyst: Spongelike Au/Pt Core/Shell Nanomaterial with Hollow Cavity. *J. Phys. Chem. C* **2007**, 111, 17104-17109.

108. Jayasayee, K.; Dam, V. A. T.; Verhoeven, T.; Celebi, S.; Bruijn, F. A. D., Oxygen Reduction Kinetics on Electrodeposited PtCo as a Model Catalyst for Proton Exchange Membrane Fuel Cell Cathodes: Stability as a Function of PtCo Composition. *J. Phys. Chem. C* **2009**, 113, 20371–20380.
109. Zhang, J. Z.; Noguez, C., Plasmonic Optical Properties and Applications of Metal Nanostructures. *Plasmonics* **2008**, 3, 127-150.
110. Hendel, T.; Lesnyak, V.; Kuhn, L.; Herrmann, A.; Bigall, N. C.; Borchardt, L.; Kaskel, S.; Gaponik, N.; Eychmüller, A., Mixed Aerogels from Au and CdTe Nanoparticles. *Adv. Funct. Mater.* **2013**, 23, 1903-1911.
111. Lesnyak, V.; Wolf, A.; Dubavik, A.; Borchardt, L.; Voitekhovich, S. V.; Gaponik, N.; Kaskel, S.; Eychmüller, A., 3D Assembly of Semiconductor and Metal Nanocrystals: Hybrid CdTe/Au Structures with Controlled Content. *J. Am. Chem. Soc.* **2011**, 133, 13413–13420.
112. Ranmohotti, K. G. S.; Gao, X.; Arachchige, I. U., Salt-Mediated Self-Assembly of Metal Nanoshells into Monolithic Aerogel Frameworks. *Chem. Mater.* **2013**, 25, 3528–3534.
113. Chen, J.; Wiley, B.; McLellan, J.; Xiong, Y.; Li, Z.-Y.; Xia, Y., Optical Properties of Pd-Ag and Pt-Ag Nanoboxes Synthesized via Galvanic Replacement Reactions. *Nano Lett.* **2005**, 5, 2058-2062.
114. Jing, H.; Wang, H., Structural Evolution of Ag–Pd Bimetallic Nanoparticles through Controlled Galvanic Replacement: Effects of Mild Reducing Agents. *Chem. Mater.* **2015**, 27, 2172-2180.
115. Lu, X.; Tuan, H.-Y.; Chen, J.; Li, Z.-Y.; Korgel, B. A.; Xia, Y., Mechanistic Studies on the Galvanic Replacement Reaction between Multiply Twinned Particles of Ag and HAuCl₄ in Organic Medium. *J. Am. Chem. Soc.* **2007**, 129, 1733-1742.

116. Marhaba, S.; Bachelier, G.; Bonnet, C.; Broyer, M.; Cottancin, E.; Grillet, N.; Lerme, J.; Vialle, J.-L.; Pellarin, M., Surface Plasmon Resonance of Single Gold Nanodimers near the Conductive Contact Limit. *J. Phys. Chem. C* **2009**, 113, 4349–4356.
117. Pecharroman, C., Influence of the Close Sphere Interaction on the Surface Plasmon Resonance Absorption Peak. *J. Phys. Chem. Chem. Phys.* **2009**, 11, 5922–5929.
118. Slaughter, L.; Chang, W.-S.; Link, S., Characterizing Plasmons in Nanoparticles and Their Assemblies with Single Particle Spectroscopy. *J. Phys. Chem. Lett.* **2011**, 2, 2015-2023.
119. Ferraro, J. R.; Nakamoto, K.; Brown, C. W., *Introductory Raman Spectroscopy*. 6th ed.; Academic Press: New York, 2003.
120. Stiles, P. L.; Dieringer, J. A.; Shah, N. C.; Van Duyne, R. P., Surface-Enhanced Raman Spectroscopy. *Annu. Rev. Anal. Chem.* **2008**, 1, 601-626.
121. Kim, K.; Kim, K. L.; Choi, J. Y.; Lee, H. B.; Shin, K. S., Surface Enrichment of Ag Atoms in Au/Ag Alloy Nanoparticles Revealed by Surface-Enhanced Raman Scattering of 2,6-Dimethylphenyl Isocyanide. *J. Phys. Chem. C* **2010**, 114, 3448-3453.
122. Pavel, I. E.; Alnajjar, K. S.; Monahan, J. L.; Stahler, A.; Hunter, N. E.; Weaver, K. M.; Baker, J. D.; Meyerhoefer, A. J.; Dolson, D. A., Estimating the Analytical and Surface Enhancement Factors in Surface-Enhanced Raman Scattering (SERS): A Novel Physical Chemistry and Nanotechnology Laboratory Experiment. *J. Chem. Educ.* **2012**, 89, 286-290.
123. Xie, H.; Larmour, I. A.; Smith, W. E.; Faulds, K.; Graham, D., Surface-Enhanced Raman Scattering Investigation of Hollow Gold Nanospheres. *J. Phys. Chem. C* **2012**, 116, 8338-8342.
124. Tian, L.; Tadepalli, S.; Fei, M.; Morrissey, J. J.; Kharasch, E. D.; Singamaneni, S., Off-Resonant Gold Superstructures as Ultrabright Minimally Invasive Surface-Enhanced Raman Scattering (SERS) Probes. *Chem. Mater.* **2015**, 27, 5678-5684.

125. Budnyk, A. P.; Damin, A.; Agostini, G.; A., Z., Gold Nanoparticle Aggregates Immobilized on High Surface Silica Substrate for Efficient and Clean SERS Applications. *J. Phys. Chem. C* **2010**, 114, 3857-3862.
126. Xu, Y.; Dong, Y.; Shi, J.; Xu, M.; Zhang, Z.; Yang, X., Au@Pt Core-Shell Nanoparticles Supported on Multiwalled Carbon Nanotubes for Methanol Oxidation. *Catal. Commun.* **2011**, 13, 54-58.
127. Selvaganesh, S. V.; Slvarani, G.; Sridhar, P.; Pitchumania, S.; Shukla, S. K., Durable Electrocatalytic-Activity of Pt–Au/C Cathode in PEMFCs. *Phys. Chem. Chem. Phys.* **2011**, 13, 12623-12634.
128. Salgadoa, J. R. C.; Antolinia, E.; Gonzaleza, E. R., Carbon Supported Pt–Co Alloys as Methanol-Resistant Oxygen-Reduction Electrocatalysts for Direct Methanol Fuel Cells. *Appl. Catal. B-Environ.* **2005**, 57, 283-290.
129. Kashyout, A. B.; Bakar, A.; Nassr, A. A.; Giorgi, L.; Maiyalagan, T.; Youssef, B. A. B., Electrooxidation of Methanol on Carbon Supported Pt-Ru Nanocatalysts Prepared by Ethanol Reduction Method. *Int. J. Electrochem. Sci.* **2011**, 6, 379-393.
130. Kawaguchi, T.; Sugimoto, W.; Murakami, Y.; Takasu, T., Particle Growth Behavior of Carbon-Supported Pt, Ru, Pt/Ru Catalysts Prepared by An Impregnation Reductive-Pyrolysis Method for Direct Methanol Fuel Cell Anodes. *J. Catal.* **2005**, 229, 176-184.
131. Teng, X.; Liang, X.; Rahman, S.; Yang, H., Porous Nanoparticle Membranes: Synthesis and Application as Fuel-Cell Catalysts *Adv. Mater.* **2005**, 17, 2237-2241.
132. Chen, C.; He, J.; Xu, D.; Tan, X.; Zhou, X.; Wang, X., Study of Nano-Au Assembled Amperometric CO Gas Sensor. *Sens. Actuators B* **2007**, 107, 866-871.

133. Zhang, Y.; Huang, Q.; Zou, Z.; Yang, J.; Vogel, W.; Yang, H., Enhanced Durability of Au Cluster Decorated Pt Nanoparticles for the Oxygen Reduction Reaction. *J. Phys. Chem. C* **2010**, 114, 6860–6868.
134. Formo, E.; Lee, E.; Campbell, D.; Xia, Y., Functionalization of Electrospun TiO₂ Nanofibers with Pt Nanoparticles and Nanowires for Catalytic Applications. *Nano Lett.* **2008**, 8, 668-672.
135. Rolison, D. R.; Long, J. W.; Lytle, J. C.; Fischer, A. E.; Rhodes, C. P.; McEvoy, T. M.; Bourga, M. E.; Lubersa, A. M., Multifunctional 3D Nanoarchitectures for Energy Storage and Conversion. *Chem. Soc. Rev.* **2009**, 38, 226-252.
136. Cheetham, A. K.; Day, P., *Solid State Chemistry: Techniques*. **1987**, Clarendon Press: Oxford, 1987, 39-82.
137. Cullity, B. D., *Elements of X-ray Diffraction, 3rd ed.* **1978**, Prentice Hall: Upper Saddle River, NJ.
138. Racker, D. K., *Transmission Electron Microscopy* **1983**, Charles C. Thomas: Springfield, Illinois.
139. Flewitt, P. E. J.; Wild, R. K., *Physical Methods for Materials Characterization*. Institute of Physics Publishing :Philadelphia, 1994.
140. Reimer, L., *Transmission Electron Microscopy: Physics of Image Formation and Microanalysis. 4ed* **1997**, Springer-Verlag: New York.
141. Urch, D. S., Photoelectron and X-ray Emission Spectroscopy: Basic Principles and Chemical Effects. *X-ray Spectroscopy in Atomic and Solid State Physics* **1987**, Plenum Press: New York.

142. Niu, H.; Houk, R. S., Fundamental Aspects of Ion Extraction in Inductively Coupled Plasma Mass Spectrometry *Spectrochim. Acta Part B* **1996**, 51, 779-815.
143. Webb, P. A.; Orr, C., *Analytical Methods in Fine Particle Technology*. Micromeritics: Norcross (Georgia), 1997.
144. Gregg, S. J.; Sing, K. S. W., *Adsorption, Surface Area and Porosity*. 2nd ed.; Academic Press: New York, 1982.
145. Smith, E. D., G., *Modern Raman Spectroscopy: A Practical Approach*. **2005**, John Wiley & Sons: West Sussex, England.
146. El-Sayed, M. A., *Acc. Chem. Res.* **2001**, 34, 257-264.
147. Pattanayak, S.; Priyam, A.; Paik, P., Facile Tuning of Plasmon Bands in Hollow Ag Nanoshells Using Mild reductant and Stabilizer. *Dalton Trans.* **2013**, 42, 10597-10607.
148. Finley, J. W.; Wheeler, E. L.; Witt, S. C., Oxidation of Glutathione by Hydrogen Peroxide and Other Oxidizing Agents. *J. Agric. Food Chem.* **1981**, 29, 404-407.
149. Detty, M. R.; Friedman, A. E.; Oseroff, A. R., A Mechanism for the Oxidation of Glutathione to Glutathione Disulfide with Organotellurium(IV) and Organoselenium(IV) Compounds. A Stepwise Process with Implications for Photodynamic Therapy and Other Oxidative Chemotherapy. *J. Org. Chem.* **1994**, 59, 8245-8250.
150. Pala, I. R.; Arachchige, I. U.; Georgiev, D. G.; Brock, S. L., Reversible Gelation of II-VI Nanocrystals: The Nature of Interparticle Bonding and the Origin of Nanocrystal Photochemical Instability. *Angew. Chem. Int. Ed.* **2010**, 49, 3661-3665.
151. Stabsbie, J. H., *J. Soc. Chem. Ind.* **1913**, 32, 311-319.
152. Briggs, D.; Seah, M. P., *Practical Surface Analysis: Auger and X-ray Photoelectron Spectroscopy*. 2nd ed.; Wiley and Sons: 1993; Vol. 1.

153. Wang, J. H.; Dai, W. L.; Deng, J. F.; Wei, X. M.; Cao, Y. M.; Zhai, R. S., Interaction of oxygen with silver surface at high temperature. *Appl. Surf. Sci.* **1998**, 126, 148-152.
154. Zhou, W. J.; H., L. Y.; M., H. D.; Li, H. D.; Li, L. G.; Li, G. Q.; Liu, H.; Chen, S. W., Phase transformation and enhanced photocatalytic activity of S-doped Ag₂O/TiO₂ heterostructured nanobelts. *Nanoscale* **2014**, 6, 4698-4704.
155. Korala, L.; Brock, S. L., Aggregation Kinetics of Metal Chalcogenide Nanocrystals: Generation of Transparent CdSe (ZnS) Core (Shell) Gels. *J. Phys. Chem. C* **2012**, 116, 17110-17117.
156. Korala, L.; Li, L.; Brock, S. L., Transparent Conducting Films of CdSe(ZnS) Core(Shell) Quantum Dot Xerogels. *Chem. Commun.* **2012**, 48, 8523-8525.
157. Gao, X.; Esteves, R. J.; Luong, T. T. H.; Jaini, R.; Arachchige, I. U., Oxidation-Induced Self-Assembly of Ag Nanoshells into Transparent and Opaque Ag Hydrogels and Aerogels. *J. Am. Chem. Soc.* **2014**, 136, 7993–8002.
158. Cabot, A.; Ibanez, M.; Guardia, P.; Alivisatos, A. P., Reaction Regimes on the Synthesis of Hollow Particles by the Kirkendall Effect *J. Am. Chem. Soc.* **2009**, 131, 11326-11328.
159. Sun, Y.; Mayers, B.; Xia, Y., Metal Nanostructures with Hollow Interiors. *Adv. Mater.* **2003**, 15, 641-646.
160. Ghosh, T.; Satpati, B.; Senapati, D., Characterization of Bimetallic Core-Shell Nanorings Synthesized via Ascorbic Acid-Controlled Galvanic Displacement followed by Epitaxial Growth. *J. Mater. Chem. C* **2014**, (2), 2439-2447.
161. Yang, Y.; Zhang, Q.; Fu, Z.-W.; Qin, D., Transformation of Ag Nanocubes into Ag-Au Hollow Nanostructures with Enriched Ag Contents to Improve SERS Activity and Chemical Stability. *ACS Appl. Mater. Interfaces* **2014**, (6), 3750-3757.

162. Aherne, D.; Gara, M.; Kelly, J. M.; Gun'ko, Y. K., From Ag Nanoprisms to Triangular AuAg Nanoboxes. *Adv. Funct. Mater.* **2010**, 20, 1329-1338.
163. Link, S.; Wang, Z. L.; El-Sayed, M. A., Alloy Formation of Gold-Silver Nanoparticles and the Dependence of the Plasmon Absorption on Their Composition. *J. Phys. Chem. B* **1999**, 103, 3529-3533.
164. Lee, K. S.; El-Sayed, M. A., Gold and Silver Nanoparticles in Sensing and Imaging: Sensitivity of Plasmon Response to Size, Shape, and Metal Composition. *J. Phys. Chem. B* **2006**, (110), 19220-19225.
165. AbdelHamid, A. A.; Al-Ghobashy, M. A.; Fawzy, M.; Mohamed, M. B.; Abdel-Mottaleb, M. M. S. A., Phytosynthesis of Au, Ag, and Au-Ag Bimetallic Nanoparticles Using Aqueous Extract of Sago Pondweed (*Potamogeton Pectinatus* L.). *ACS Sustainable Chem. Eng.* **2013**, 1, 1520-1529.
166. Gao, C.; Hu, Y.; Wang, M.; Chi, M.; Yin, Y., Fully Alloyed Ag/Au Nanospheres: Combining the Plasmonic Property of Ag with the Stability of Au. *J. Am. Chem. Soc.* **2014**, 136, 7474-7479.
167. Sanchez-Gaytan, B. L.; Park, S.-J., Spiky Gold Nanoshells. *Langmuir* **2010**, 26, 19170-19174.
168. Sanchez-Gaytan, B. L.; Swanglap, P.; Lamkin, T. J.; Hickey, R. J.; Fakhraai, Z.; Link, S.; Park, S.-J., Spiky Gold Nanoshells: Synthesis and Enhanced Scattering Properties. *J. Phys. Chem. C* **2012**, 116, 10318-10324.
169. Philip, D., Biosynthesis of Au, Ag and Au-Ag Nanoparticles Using Edible Mushroom Extract. *Spectrochim. Acta, Part A* **2009**, 73, 374-381.

170. Nahar, L.; Esteves, R. J. A.; Hafiz, S.; Özgür, Ü.; Arachchige, I. U., Metal-Semiconductor Hybrid Aerogels: Evolution of Optoelectronic Properties in a Low Dimensional CdSe/Ag Nanoparticle Assembly *ACS Nano* **2015**, 9, 9810-9821.
171. Herrmann, A.-K.; Formanek, P.; Borchardt, L.; Klose, M.; Giebeler, L.; Eckert, J.; Kaskel, S.; Gaponik, N.; Eychmueller, A., Multimetallic Aerogels by Template-Free Self-Assembly of Au, Ag, Pt, and Pd Nanoparticles. *Chem. Mater.* **2014**, 26, 1074-1083.
172. Borchert, H.; Shevchenko, E. V.; Robert, A.; Mekis, I.; Kornowski, A.; Grubel, G.; Weller, H., Determination of Nanocrystal Sizes: A Comparison of TEM, SAXS, and XRD Studies of Highly Monodisperse CoPt₃ Particles. *Langmuir* **2005**, 21, 1931-1936.
173. Vosgrone, T.; Meixner, A. J., Surface- and Resonance-Enhanced Micro-Raman Spectroscopy of Xanthene Dyes: From the Ensemble to Single Molecules. *ChemPhysChem* **2005**, 6, 154-163.
174. Vosgrone, T.; Meixner, A. J., Surface- and Resonance-Enhanced Micro-Raman Spectroscopy of Xanthene Dyes at Single-Molecule Level. *J. Lumin.* **2004**, 107, 13-20.
175. Chen, L.; Chabu, J. M.; Liu, Y., Bimetallic AgM (M = Pt, Pd, Au) Nanostructures: Synthesis and Applications for Surface-Enhanced Raman Scattering. *RSC Adv.* **2013**, 3, 4391–4399.
176. Qian, Z.; Li, C.; Fakhraai, Z.; Park, S.-J., Unusual Weak Interparticle Distance Dependence in Raman Enhancement from Nanoparticle Dimers. *J. Phys. Chem. C* **2016**, 120, 1824-1830.
177. Hastings, S. P.; Swanglap, P.; Qian, Z.; Fang, Y.; Park, S.-J.; Link, S.; Engheta, N.; Fakhraai, Z., Quadrupole-Enhanced Raman Scattering. *ACS Nano* **2014**, 8, 9025-9034.

178. Dinh, H. N.; Ren, X. M.; Garzon, F. H.; Zelenay, P.; Gottesfeld, S., Electrocatalysis in Direct Methanol Fuel Cells: In-Situ Probing of PtRu Anode Catalyst Surfaces. *J. Electroanal. Chem.* **2000**, 491, 222-233.
179. Tai, Y.; Tajiri, K., Preparation, Thermal Stability, and CO Oxidation Activity of Highly Loaded Au/Titania-Coated Silica Aerogel Catalysts. *Appl. Catal. A* **2008**, 342, 113-118.
180. Wen, D.; Herrmann, A.-K.; Borchardt, L.; Simon, F.; Liu, W.; Kaskel, S.; Eychmueller, A., Controlling the Growth of Palladium Aerogels with High-Performance toward Bioelectrocatalytic Oxidation of Glucose. *J. Am. Chem. Soc.* **2014**, 136, 2727–2730.
181. Liu, W.; Rodriguez, P.; Borchardt, L.; Foelske, A.; Yuan, J.; Herrmann, A.-K.; Geiger, D.; Zheng, Z.; Kaskel, S.; Gaponik, N.; Koetz, R.; Schmidt, T. J.; Eychmueller, A., Bimetallic Aerogels: High-Performance Electrocatalysts for the Oxygen Reduction Reaction. *Angew. Chem. Int. Ed.* **2013**, 52, 9849-9852.
182. Gao, X.; Esteves, R. J.; Nahar, L.; Nowaczyk, J.; Arachchige, I. U., Direct Cross-Linking of Au/Ag Alloy Nanoparticles into Monolithic Aerogels for Application in Surface Enhanced Raman Scattering. *ACS appl. Mater. Interfaces* **2016**, Just Accepted.
183. Garcia-Leis, A.; Torreggiani, A.; Garcia-Ramos, J. V.; Sanchez-Cortes, S., Hollow Au/Ag Nanostars Displaying Broad Plasmonic Resonance and High Surface-Enhanced Raman Sensitivity. *Nanoscale* **2015**, 7, 13629-13637.
184. Kim, J.-D.; Lee, Y.-J.; Park, J.-Y., Miniaturized Electrochemical Methanol Sensor Using Macroporous Au with Pt Nano-Particles *Sens. Lett.* **2011**, 9, 106-109.
185. Du, C.; Yao, Z.; Chen, Y.; Bai, H.; Li, L., Synthesis of Metal Nanoparticle@Graphene Hydrogel Composites by Substrate-Enhanced Electroless Deposition and Their Application in Electrochemical Sensors. *RSC Adv.* **2014**, 4, 9133–9138.

186. Bag, S.; Kanatzidis, M. G., Chalcogels: Porous Metal-Chalcogenide Networks from Main-Group Metal Ions. Effect of Surface Polarizability on Selectivity in Gas Separation. *J. Am. Chem. Soc.* **2010**, 132, 14951-14959.
187. Pietron, J. J.; Pomfret, M. B.; Chervin, C. N.; Long, J. W.; Rolison, D. R., Direct Methanol Oxidation at Low Overpotentials Using Pt Nanoparticles Electrodeposited at Ultrathin Conductive RuO₂ Nanoskins. *J. Mater. Chem.* **2012**, 22, 5197-5204.
188. Wu, W.; Lin, Y.-T., Feasible Input Manipulation for a Nonisothermal Direct Methanol Fuel Cell System. *Ind. Eng. Chem. Res.* **2010**, 49, 5725-5733.

Vita

Xiaonan Gao

Born Oct. 7th, 1986 in Shandong, China

Email: gaox6@vcu.edu

Education

- Ph. D. Chemistry, Virginia Commonwealth University **Aug. 2011 to May 2016**
- B.S. (Honors) Chemistry, East Tennessee State University **Aug. 2007 to May 2009**
- B. S. Chemistry, Shandong Normal University **Sep. 2005 to Jul. 2009**

Research Experience

- 09/2011 – 05/2016 Graduate Assistant, Virginia Commonwealth University
Advisor: Dr. Indika U. Arachchige
- 10/2009 – 05/2011 Graduate Assistant, Worcester Polytechnic University
Advisor: Dr. W. Grant McGimpsey
- 09/2008 – 05/2009 Research Volunteer, East Tennessee State University
Advisor: Dr. Yulin Jiang
- 09/2005 – 07/2007 Research Volunteer, Dezhou University, Shandong, China
Advisor: Dr. Aiyun Fu

Teaching Experience

- 08/2011 – 05/2014 Graduate Teaching Assistant, Virginia Commonwealth University
- 08/2009 – 05/2011 Graduate Teaching Assistant, Worcester Polytechnic Institute

Honors and Awards

- Third Place Scholarship, Shandong Normal University, 2005.
- Outstanding Student Leader, Shandong Normal University, 2006.
- Dead's List, East Tennessee State University, 2007.
- Significant Contribution to the Internalization, Virginia Commonwealth University 2012.
- Altria Fellowship, Virginia Commonwealth University, 2014.

Publications

1. Gao, X.; Esteves, R. J.; Nahar, L.; Nowaczyk, J.; Arachchige, I. U. "Direct Cross-Linking of Au/Ag Alloy Nanoparticles into Monolithic Aerogels for Application in Surface Enhanced Raman Scattering" *ACS appl. Mater. Interfaces*, Just Accepted.
2. Gao, X.; Fu, A. Y.; Wang, Y. -Y., "Shape-Asymmetry Supramolecular Isomerism in Asymmetrical Ligand PCPs and the Expression Method of Three-Level Isomerism" *Inorg. Chem.* **2016**, 55, 4330-4334
3. Gao, X.; Esteves, R. J.; Luong, T. T. H.; Jaini, R.; Arachchige I. U. "Oxidation-Induced Self-Assembly of Ag Nanoshells into Transparent and Opaque Ag Hydrogels and Aerogels" *J. Am. Chem. Soc.*, **2014**, 136, 7993–8002
4. Ranmohotti, K. G. S.; Gao, X.; Arachchige I. U. "Salt-Mediated Self-Assembly of Metal

- Nanoshells into Monolithic Aerogel Frameworks” *Chem. Mater.* **2013**, 25, 3528–3534
5. White, L. S.; Echard, D. R.; Bertino, M. F.; Gao, X.; Donthula, S.; Leventis, N.; Shukla, N.; Kośny, J.; Saeed, S.; Saoud K. “Fabrication of Native Silica, Cross-Linked, and Hybrid Aerogel Monoliths with Customized Geometries” *Transl. Mater. Res.* **2016**, 3, 015002 (1-11)
 6. White, L. S.; Migenda, J.; Gao, X.; Clifford, D. M.; Bertino, M. F.; Saoud, K. M. “Synthesis of Silicon Dioxide, Silicon, and Silicon Carbide Mesoporous Spheres from Polystyrene Sphere Templates” *J. Sol-Gel Sci. and Techno.* **2015**, 02
 7. Jiang, Y. L.; Gao X.; Zhou G., Patel A.; Javier A. “DMF/H₂O Volume Ratio Controls the Syntheses and Transformations of a Series of Cobalt Complexes Constructed Using a Rigid Angular Multitopic Ligand”, *Inorg. Chem.* **2010**, 49, 5495–5502
 8. Fu, A. Y.; Jiang Y. L.; Wang Y. Y.; Gao X.; Yang G. P.; Hou L.; Shi Q. Z. “Selective Recognition of Uracil and Its Derivatives Using a DNA Repair Enzyme Structural Mimic” *J. Org. Chem.* **2010**, 75, 324–333
 9. Gao, X. Bis(μ -N-acetyl-N-phenylglycinato- κ 2O:O')bis[dinitrato- κ 4O,O'-bis(1,10-phenanthroline- κ 2N,N')]lanthanum(III)] *Acta Cryst. Section E*, **2009**, 65(1), 59

Conference Publications

1. Gao, X.; Arachchige I. U. “Sol-Gel Method for the Assembly of Noble Metal Nanoparticles into Metallic Aerogels” *250th ACS National Meeting*, Boston, MA, United States, August 16-20, **2015**, *oral presentation*.
2. Gao, X.; Nahar L.; Arachchige I. U. “Porous Conducting Superstructures of Metal Colloids: Noble Metal Aerogels” *250th ACS National Meeting & Exposition*, Boston, MA, United States, August 16-20, **2015**, Abstracts of Papers
3. Gao, X.; Arachchige I. U. “Sol-Gel Assembly of Silver Nanoshells into Aerogel Frameworks” *65th Southeast Regional Meeting of the American Chemical Society*, Atlanta, GA, United States, November 13-16, **2013**, *oral presentation*.
4. Luong, T. T. H.; Gao, X.; Ranmohotti, K. G. S.; Arachchige I. U. “Non-Ordered Metal Hollow Particle Superstructures: Metal Aerogels” *65th Southeast Regional Meeting of the American Chemical Society*, Atlanta, GA, United States, November 13-16, **2013**, *Abstract*
5. Ranmohotti, K. G. S.; Gao, X.; Arachchige I. U. “Self-Supported Assembly of Hollow Metallic Spheres into Metallic Aerogel Frameworks” *245th ACS National Meeting & Exposition*, New Orleans, LA, United States, April 7-11, **2013**, *Abstracts of Papers*